Explorations of Water Oxidation Catalysis in Explicit Solvent

Jessica M. de Ruiter

Explorations of Water Oxidation Catalysis in Explicit Solvent

PROEFSCHRIFT

ter verkrijging van
de Graad van Doctor aan de Universiteit Leiden,
op gezag van Rector Magnificus prof. mr. C. J. J. M. Stolker,
volgens besluit van het College voor Promoties
te verdedigen op dinsdag 30 oktober 2018
klokke 13.45 uur

door

Jessica M. de Ruiter

geboren te Nelson, Nieuw-Zeeland
in 1989

Promotiecommissie

Promoter:	Prof. dr. Huub J. M. de Groot
Co-promoter:	Dr. Francesco Buda
Overige leden:	Prof. dr. Marc. T. M. Koper
	Prof. dr. Hermen S. Overkleeft
	Prof. dr. Shirin Faraji (University of Groningen, The Netherlands)
	Prof. dr. Leif Hammarström (Uppsala University, Sweden)

Jessica M. de Ruiter
Explorations of Water Oxidation Catalysis in Explicit Solvent
Ph.D. thesis, Leiden University

ISBN: 978-94-6332-412-0

Cover and bookmark designed by Nico de Ruiter

This thesis was printed on 100% recycled paper.

This research was financed by Leiden University, and co-financed by the Dutch Ministry of Economic Affairs as part of the BioSolar Cells research project C1.9. The use of supercomputer facilities was sponsored by NWO Exact and Natural Sciences, with financial support from the Netherlands Organization for Scientific Research (NWO).

Table of Contents

List of Abbreviations

ADF	Amsterdam Density Functional
AIMD	*Ab Initio* Molecular Dynamics
ALDA	Adiabatic Local Density Approximation
B3LYP	Becke 3 parameter; Lee Yang Parr
BJDAMP	Becke Johnson DAMPing
BOA	Born-Oppenheimer Approximation
CE	Counter Electrode
CFF	Consistent Force Field
CHARMM	Chemistry at HARvard Macromolecular Mechanics
COSMO	Conductor Like Screening Model
CPMD	Car-Parrinello Molecular Dynamics
CSA	Closed System Approach
CV	Cyclic Voltammetry
d(X→Y)	Distance constraint/constrained distance between X and Y
DCACP	Dispersion-Corrected Atom-Centred Potential
DFT	Density Functional Theory
EQCN	Electrochemical Quartz Crystal Nanobalance
GC	Glassy Carbon
GGA	Generalised Gradient Approximation
GTH	Goedecker Teter Hutter
HF	Hartree-Fock
KS	Kohn-Sham
LanL2DZ	Los Alamos National Laboratory 2 Double Zeta
LMCT	Ligand-to-Metal Charge Transfer
MD	Molecular Dynamics
MLCT	Metal-to-Ligand Charge Transfer
NHE	Normal Hydrogen Electrode
OPBE	OPTX Perdew Burke Ernzerhof
OPTX	Handy's OPTimised eXchange functional
OLEMS	Online Electrochemical Mass Spectrometry
PBEc	Perdew Burke Ernzerhof Correlation functional
PCET	Proton-Coupled Electron Transfer
PCM	Polarisable Continuum Model
PS II	PhotoSystem II
QM/MM	Quantum Mechanics/Molecular Mechanics

RHE	Reversible Hydrogen Electrode
SCE	Saturated Calomel Electrode
SERS	Surface Enhanced Raman Spectroscopy
TDDFT	Time Dependent Density Functional Theory
TZP	Triple Zeta Polarised
VMD	Visual Molecular Dynamics visualisation program
WE	Working Electrode
WOC	Water Oxidation Catalyst

General Introduction & Computational Tools

Chapter One

1. General Introduction and Computational Tools

Abstract

In this chapter the context for this thesis is introduced. Furthermore a brief outline is given of the computational methods used, as well as supporting theory.

1.1. The search for sustainable energy solutions

World-wide, there is an increasing amount of attention being invested into sustainable energy solutions,[1–3] one of which is hydrogen. A critical hurdle is securing a sustainable supply of hydrogen.[4] Not only can hydrogen replace fossil fuels as a combustible source of energy, it is an essential part of the Haber-Bosch process, and plays an important role in carbon chemistry. The Haber-Bosch process uses hydrogen to produce ammonia which, as an agricultural fertilizer, is responsible for food production for a significant percentage of the global population.[5] Indeed, around half of the hydrogen produced globally is used for ammonia production.[6,7] As the global population increases, the need for food, and therefore hydrogen, must surely increase. Furthermore, unprecedented amounts of hydrogen will be needed within the chemical industry: hydrogen can be reacted with CO_2, both from the atmosphere as well as from industrial emissions, to produce useable hydrocarbons. However, this must occur on the gigatonne scale.[8] Considering that around 95 % of hydrogen is currently generated via steam reforming of natural gas,[6,7] new hydrogen generation methods must be explored.

One of the most promising methods of generating hydrogen is via artificial photosynthesis. A schematic representation of an artificial photosynthetic system is shown in Figure 1.1.[9] An antenna component absorbs sunlight which is used to excite an electron in the photosensitiser, after which excitation energy is converted into electrochemical energy. This electrochemical energy is used as redox potential by a WOC to catalyse water splitting. This splitting results in oxygen, hydrogen ions, and electrons which are stored as reducing equivalents. These reducing equivalents are then transferred via an electron transfer system

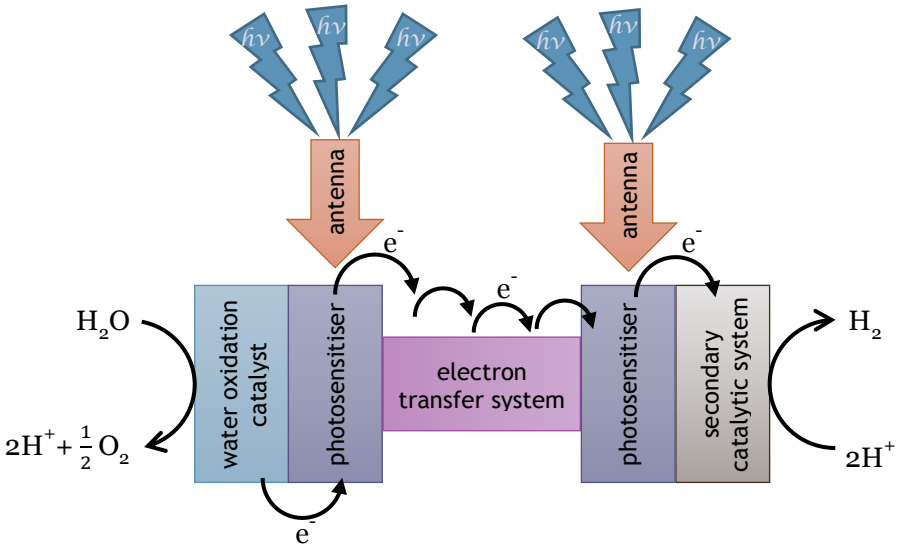

Figure 1.1 The basic components of a solar fuel production system

and a second photosensitiser to a secondary catalytic system which then reduces the hydrogen ions to molecular hydrogen. This secondary catalytic system may also be used in the generation of hydrocarbons. Although this may sound straight forward, challenges include rapid and efficient water splitting, efficient visible-light absorption and stable charge separation.[10] Stable charge separation is one of the greatest challenges, which the natural photosynthetic system achieves by means of a highly complex electron transfer system that prevents back reactions

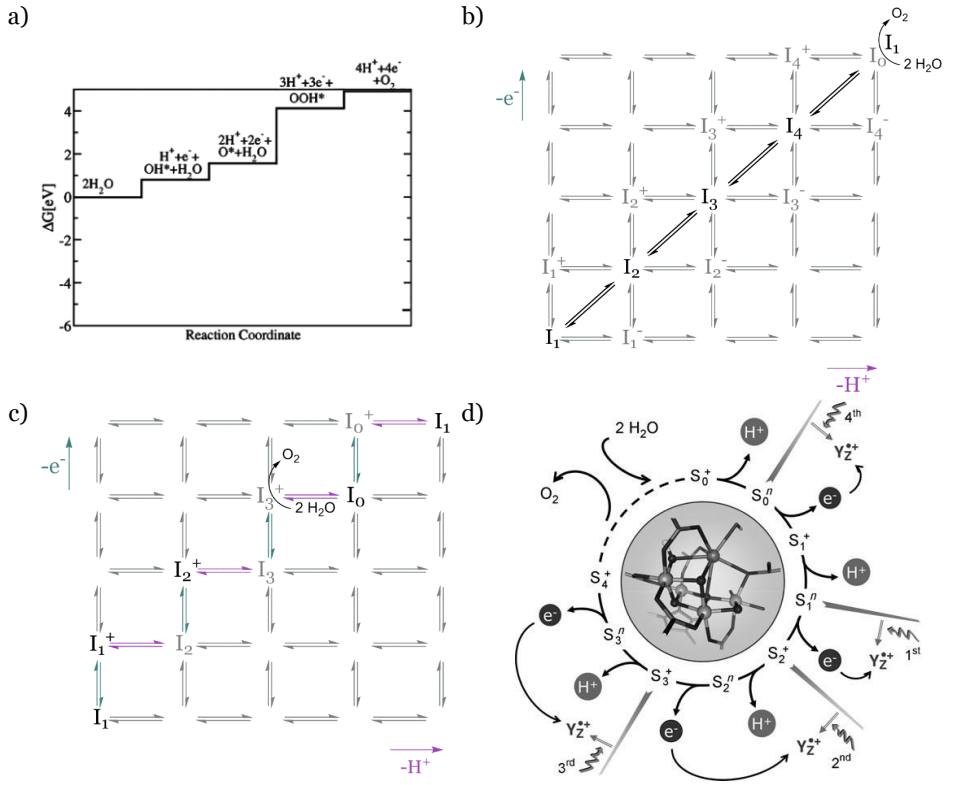

Figure 1.2 (a) The changes in free energy for the four PCET steps of a heterogeneous WOC, where * indicates the adsorbents. Adapted from Rossmeisl et al.[22] (b) The four PCET steps between the catalytic intermediates I_1 - I_0. Vertical lines denote electron transfer, horizontal lines proton transfer. The ligand exchange $I_0 + H_2O \rightarrow I_1 + O_2$ is shown in the top right corner. (c) The decoupled PCET reactions of the Mn complex, where vertical lines denote electron transfer and horizontal lines proton transfer. The stable states are shown in black: I_1, I_1^+, I_2^+ and I_0, which correspond to S_1^n, S_2^+, S_3^+ and S_0^n in Dau's notation shown in (d). (d) The water oxidation mechanism for the Mn complex in the natural photosynthetic system, as reproduced from Dau et al.[19] We note that two of the stable states shown in (c) are off-diagonal when compared to (b), these represent the interchange of transition states and intermediates. The start of the cycle (I_0, I_1) has intermediates on the diagonal, while the I_1^+ and I_2^+ are off-diagonal. This leads to a mismatch between the end and the start of the reaction coordinate that requires a rearrangement involving the exchange of O_2 by $2H_2O$ in an energetically downhill process. This supplies a molecular level heat pulse at the right time and location for the release of the gaseous O_2.

and electron-hole recombination, by matching time, length and energy scales.[11]

Water splitting forms an important challenge in the move towards a fully sustainable energy infrastructure,[12–14] which has led to an explosion in the WOC research field.[10,15–18] The primary function of a WOC is to drive water oxidation. To do so, it must be able to process four electrons, according to

$$2H_2O \rightarrow O_2 + 4H^+ + 4e^-. \qquad (1.1)$$

The thermodynamic potential E^0 of water oxidation is 1.23 V. In the natural photosynthetic system this reaction proceeds via PCET steps.[19] The water oxidation mechanism for many heterogeneous catalysts also features four PCET steps. The pH-independent changes in free energy throughout the catalytic cycle are often depicted as shown in Figure 1.2 (a). Although at longer time scales one might consider these steps concerted, i.e. that proton and electron transfer occurs simultaneously, on short enough timescales these processes will be decoupled. If we consider Figure 1.2 (b), the diagonal arrows would denote the concerted reaction. If we were to decouple the electron and proton transfer processes, proton and electron transfer could occur in varying sequences throughout the catalytic cycle. For example, one could first transfer one electron ($I_1 \rightarrow I_1^+$) in Figure 1.2 (b) followed by two protons ($I_1^+ \rightarrow I_2^-$). This technique is also employed in the natural photosynthetic system, as shown in Figure 1.2 (c), yielding a total of 9 decoupled states (Figure 1.2 (d)),[20] in contrast to the four intermediates S0-S3 of the Kok model.[21] Though the second step is PCET, the first catalytic step involves only the transfer of an electron ($I_1 \rightarrow I_1^+$ in Figure 1.2 (c)). These sequences could therefore be modified in the search for an optimal water oxidation catalyst.

In the search for the optimal water oxidation catalyst, one should bear in mind the energetic relationships between catalytic intermediates. It has been established, using heterogeneous catalysis, that a scaling relationship exists between the adsorption energies of the OH and OOH groups (see Figure 1.3, left).[23,24] Because the OH and OOH groups bind to surfaces in similar ways, the stabilisation or destabilisation of one intermediate will affect the other in the same way. For various oxide surfaces the difference in energies between the OH and OOH intermediates remains roughly constant at 3.2 eV.[24] This introduces a minimum overpotential for WOCs, where the overpotential is the difference between the potential at which a WOC operates and 1.23 V. Plotting negative overpotential as a function of the descriptor $\Delta G_O^0 - \Delta G_{OH}^0$ yields a volcano plot (see Figure 1.3, right), which can be used to evaluate WOCs. The apex of the volcano indicates the minimum overpotential needed to overcome both O and OH binding energies.[24]

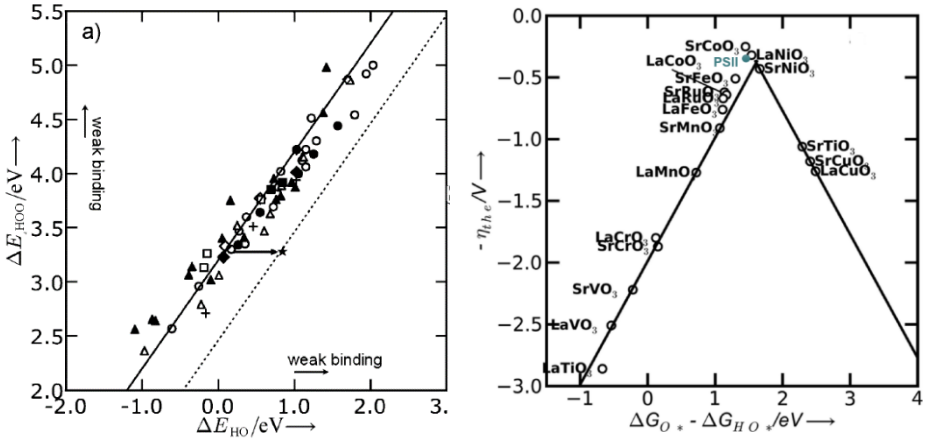

Figure 1.3 (left) Adsorption energy of OOH plotted against the adsorption energy of OH on perovskites, rutiles, anatase, Mn_xO_y, Co_3O_4, and NiO oxides. (right) Activity trends towards oxygen evolution plotted for perovskites. Both reproduced from Man et al., [24] where the PS II data point in (right) has been added (in green) for this thesis.

In designing a biomimetic WOC, there are two energetic properties that should be aimed for. The first is to have differences in energy between catalytic intermediates that would place the WOC on the apex of the volcano plot shown in Figure 1.3 (right). The second is to design the WOC so that intermediates occupy both diagonal and off-diagonal positions when considering the four PCET steps as shown in Figure 1.2 (c). In addressing these challenges, computational techniques will prove essential.

Computational techniques are increasingly employed to test the energetic properties of proposed WOCs.[25–31] Traditionally, catalytic cycles are examined computationally by comparing the free energies of the proposed catalytic intermediates and then, usually, assigning the thermodynamically most favourable cycle as the most likely catalytic cycle.[25–30] This examination often uses an implicit solvent model or correction factors to account for protons and electrons removed in the catalytic step itself.[25,27,29,32–35] Using correction factors prevents direct comparisons of the energy of intermediates as the compared intermediates usually contain different numbers of protons and electrons. In the case of PCET processes,[36] it is also becoming increasingly clear that explicit solvent molecules are needed to obtain realistic descriptions of reaction pathways.[37–39]

The aim of this thesis has been to further examine the catalytic mechanisms of WOCs within an explicit solvent environment, to compare this to the status quo, and to propose a novel approach with which to explore the reaction process and free-energy profile from one catalytic intermediate to the next.

1.2. Computational Tools

1.2.1. Density Functional Theory

The BOA arises from the large mass difference between electrons and nuclei. Electrons usually move much faster than nuclei, so may be considered to readjust instantaneously to changes in nuclear configuration. In this way nuclear and electronic motion may be considered independently from each other. The electronic ground-state can then be studied with DFT. DFT is a well-established computational method which obtains the electronic energy as a functional of the density $\rho(\boldsymbol{r})$ of electrons in the system. We consider a system of N nuclei and n electrons, where the Kth nucleus is positioned at $\boldsymbol{R}_K$ and the ith electron at $\boldsymbol{r}_i$. KS orbitals $\varphi_i(\boldsymbol{r})$, being one-electron wave functions, may be used to obtain the density of the non-interacting system

$$\rho_S(\boldsymbol{r}) = \sum_{i=1}^{n} |\varphi_i(\boldsymbol{r})|^2, \tag{1.2}$$

in atomic units. In atomic units the physical quantities $(4\pi\varepsilon_0)^{-1}$, known as Coulomb's constant with ε_0 the vacuum permittivity; m_e, the mass of an electron; e, the elementary charge; and $\hbar$, the reduced Planck's constant are defined to be 1.

The energy functional

$$\begin{aligned} E &= E[\rho(\boldsymbol{r})] \\ &= T[\rho] + V[\rho] \\ &= T[\rho] + V_{e-e}[\rho] + V_{n-e}[\rho] + V_{n-n}[\rho], \end{aligned} \tag{1.3}$$

includes a kinetic energy term, $T[\rho]$, and a potential term $V[\rho]$ which has three contributions. The potential due to nuclear electron interactions $V_{n-e}[\rho]$ can be generalised to the potential due to an external field, as integrated over all space $\mathbb{R}^3$,

$$V_{n-e}[\rho] = \int_{\mathbb{R}^3} \rho(\boldsymbol{r}) v_{ext}(\boldsymbol{r}) d\boldsymbol{r}, \tag{1.4}$$

which depends solely on changes in geometry. The potential due to nuclear interactions $V_{n-n}[\rho]$, with Z_J the atomic charge of nucleus J

$$V_{n-n}[\rho] = \sum_{J=1,K>J}^{N} \frac{Z_J Z_K}{|\boldsymbol{R}_J - \boldsymbol{R}_K|}, \tag{1.5}$$

is constant for a given nuclear conformation, within the BOA.

$T[\rho]$ and $V_{e-e}[\rho]$ are dependent on the electrons in the system and therefore are universal functionals once the number of electrons is fixed. In

$$T[\rho] + V_{e-e}[\rho] = -\frac{1}{2}\sum_{i=1}^{n}\langle\varphi_i^*|\nabla^2|\varphi_i\rangle + \frac{1}{2}\int_{\mathbb{R}^3}\frac{\rho(\boldsymbol{r})\rho(\boldsymbol{r}')}{|\boldsymbol{r}-\boldsymbol{r}'|}d\boldsymbol{r}d\boldsymbol{r}' + E_{xc}[\rho], \tag{1.6}$$

part of $T[\rho]$ is approximated using the one-electron kinetic energy operator and part of $V_{e-e}[\rho]$ is described by the classical average Coulomb interactions, but the quantum contributions due to electron – electron correlation are still not well described. These unknown terms are collected in the exchange correlation energy functional $E_{xc}[\rho]$ and it is this term that DFT tries to approximate. If $E_{xc}[\rho]$ was given exactly, the KS equations

$$\hat{h}_i^{KS}\varphi_i = \varepsilon_i\varphi_i \tag{1.7}$$

$$\hat{h}_i^{KS} = -\frac{1}{2}\nabla^2 + v_{ext}(\boldsymbol{r}) + \int_{\mathbb{R}^3}\frac{\rho(\boldsymbol{r}')}{|\boldsymbol{r}-\boldsymbol{r}'|}d\boldsymbol{r}' + V_{xc}[\rho] \tag{1.8}$$

would give the exact ground state energy. In Eqn. (1.8) the term V_{xc} is the functional derivative of E_{xc}:

$$V_{xc}[\rho] = \frac{\delta E_{xc}}{\delta\rho}. \tag{1.9}$$

Functionals, basis sets, and other approximations

There are a number of different ways to approximate the $E_{xc}[\rho]$ term, which are then implemented in a variety of different functionals. GGA approximates $E_{xc}[\rho]$ per electron as a function of the electron density ρ as well as the first derivative of the density

$$E_{xc}^{GGA}[\rho,\nabla\rho] = \int_{\mathbb{R}^3}\rho(\boldsymbol{r})f[\rho(\boldsymbol{r}),\nabla\rho(\boldsymbol{r})]\,d\boldsymbol{r}. \tag{1.10}$$

The GGA functional which is primarily used in this thesis is OPBE.[40]

Hybrid GGA functionals

$$E_{xc}^{Hybrid}[\rho] = (1-a)E_{xc}^{GGA}[\rho,\nabla\rho] + aE_{x}^{HF}[\rho], \qquad (1.11)$$

are very widely used. They include part of the exact HF exchange $E_x^{HF}[\rho]$ as well as GGA exchange-correlation $E_{xc}^{GGA}[\rho]$, where a determines the mixing between the HF and GGA exchange. Incorporating HF as well as GGA exchange has been shown to improve the accuracy of a number of molecular properties.[41] Here we use the B3LYP functional which has 20% HF exchange.[42]

The KS orbitals are usually written in terms of a linear combination of basis set functions. Especially in the case of plane wave basis sets, it is customary to use a pseudopotential, which describes the core, or non-valence, electrons of an atom using an effective potential.[43,44] In Gaussian 09 LanL2DZ is used,[45–47] which is a popular pseudopotential for the larger transition metals.[41] In ADF [48–50] Slater-Type Orbitals are used as basis functions. The basis set used, TZP, describes the core electrons using double-zeta, valence electrons using triple-zeta, and includes one polarisation function. This is considered the best balance between accuracy and computational cost for the systems we consider. In CPMD,[51] which uses a plane wave/pseudopotential implementation of DFT, PBE pseudopotentials of the Kleinman-Bylander form are used.[52,53]

Dispersion corrections by Grimme are also added.[54] This attempts to approximate, and correct for, the effect of van der Waals forces (including instantaneous dipole – instantaneous dipole interactions) in the system.

There are two different methods that are used to simulate the solvation of the system in static calculations: in ADF the COSMO,[55] and in Gaussian 09 the PCM.[56] Both methods, though having slightly different origins, currently have similar implementations.[55] The solute molecule is located inside a molecule-shaped cavity within a dielectric medium where the dielectric constant is dependent on the solvent used.

1.2.2. Time Dependent Density Functional Theory

Electronic excited-states are not easily accessible by DFT, which is a ground-state theory in its original formulation. TDDFT is a theory which generalises DFT in the presence of a time-dependent external field.[57–61] Here we focus on linear response TDDFT in particular, which makes use of the KS orbitals obtained in the ground-state. If we consider an excitation induced by a perturbation due to a time-dependent external potential $\delta v_{ext}(\boldsymbol{r},t)$, linear response theory applies when this perturbation is sufficiently small. The density response depends on perturbations at other positions $\boldsymbol{r}'$ and earlier times t'. Time t is replaced by

frequency ω in order to facilitate the extraction of the excitation energies from the linear response of the system.[61]

The first order change in density

$$\delta\rho(\boldsymbol{r},\omega) = \int_{\mathbb{R}^3} \chi_s(\boldsymbol{r},\boldsymbol{r}';\omega)\, \delta v_{eff}(\boldsymbol{r}',\omega)\, d\boldsymbol{r}', \tag{1.12}$$

features the response function of the non-interacting KS system,

$$\chi_s(\boldsymbol{r},\boldsymbol{r}';\omega) = \sum_{i=1}^{n}\sum_{a=1}^{m} 2\frac{\omega_{ai}}{\omega^2-\omega_{ai}^2}\varphi_i(\boldsymbol{r})\varphi_a(\boldsymbol{r})\varphi_i(\boldsymbol{r}')\varphi_a(\boldsymbol{r}'). \tag{1.13}$$

$\chi_s(\boldsymbol{r},\boldsymbol{r}';\omega)$ depends on the unperturbed KS orbitals $\varphi_i(\boldsymbol{r})$ and the difference in energy eigenvalues $\omega_{ai} \equiv \varepsilon_a - \varepsilon_i$ of the virtual $\varphi_a(\boldsymbol{r})$ and occupied $\varphi_i(\boldsymbol{r})$ KS orbitals, both of which may be obtained from the initial DFT calculation. Furthermore, $\chi_s(\boldsymbol{r},\boldsymbol{r}';\omega)$ has poles at the excitation energies of the KS system.

$\delta\rho(\boldsymbol{r},\omega)$ also contains the perturbation of the effective potential

$$\delta v_{eff}(\boldsymbol{r}',\omega) = \int_{\mathbb{R}^3} \frac{\delta\rho(\boldsymbol{r}',\omega)}{|\boldsymbol{r}-\boldsymbol{r}'|} d\boldsymbol{r}' + \delta v_{ext}(\boldsymbol{r},\omega) + \delta v_{xc}(\boldsymbol{r},\omega), \tag{1.14}$$

which depends on the two terms $\delta\rho(\boldsymbol{r},\omega)$ and $\delta v_{ext}(\boldsymbol{r},\omega)$, as well as the linearised exchange correlation potential

$$\delta v_{xc}(\boldsymbol{r},\omega) = \int_{\mathbb{R}^3} f_{xc}(\boldsymbol{r},\boldsymbol{r}';\omega)\, \delta\rho(\boldsymbol{r},\omega)\, d\boldsymbol{r}'. \tag{1.15}$$

$\delta v_{xc}(\boldsymbol{r},\omega)$ contains the time-dependent exchange correlation kernel

$$f_{xc}(\boldsymbol{r},\boldsymbol{r}';\omega) = \left.\frac{\delta v_{xc}(\boldsymbol{r},\omega)}{\delta\rho(\boldsymbol{r}',\omega)}\right|_{\rho=\rho_0}, \tag{1.16}$$

the functional derivative being computed at the ground state density ρ_0. $f_{xc}(\boldsymbol{r},\boldsymbol{r}';\omega)$ is responsible, along with the self-consistency of Eqn. (1.12) and (1.14), for the shifting of the KS poles to the exact excitation energies. The approximation of f_{xc} should technically be linked to the approximation used for

the ground-state xc potential. However, in quantum chemistry codes they are often treated independently. In this thesis the ALDA kernel

$$f_{xc}^{ALDA}(\boldsymbol{r},\boldsymbol{r}';\omega) = \delta(\boldsymbol{r}-\boldsymbol{r}')\frac{d^2}{d\rho^2}(\rho\cdot\varepsilon_{xc}(\rho))\Big|_{\rho=\rho_0} \tag{1.17}$$

is applied,[60] where for $\varepsilon_{xc}(\rho)$, the exchange correlation energy density, a parameterisation of a homogenous electron gas is used.

1.2.3. Car-Parrinello Molecular Dynamics

MD is an established method of investigating the dynamics in a system. In MD it is assumed that the nuclei are heavy enough to be described by classical mechanics and so Newton's equations of motion are used. The forces used in the evolution of the system are often derived by an effective potential, usually called a force field, containing empirical parameters, which is a severe limitation of the MD method. As a result, not all molecules will be well described due to the transferability problem, and the breaking and making of bonds cannot be simulated. The transferability problem describes the inability of force fields that have been optimised for one class of systems to be transferred to a different class of systems.

In an attempt to ameliorate this, AIMD has been developed, where the forces are calculated at each time step by solving the electronic structure for the nuclear configuration at that point in the trajectory. However, this can be computationally very demanding. In response to this, CPMD forms an approach in which the electronic structure is only solved for the initial configuration, and then evolved in time using an extended Lagrangian.[62,63] The evolved electronic structure then provides the forces needed to drive the nuclear dynamics. As a result, the nuclear trajectory and its corresponding electronic ground state are calculated simultaneously, which is significantly less computationally expensive. Usually the electronic structure problem within AIMD is solved using DFT, since this achieves the best compromise between accuracy and computational effort. The Euler-Lagrange equations of motions are given by

$$M_I\frac{d^2}{dt^2}\boldsymbol{R}_I = -\nabla_I E[\boldsymbol{R},\varphi] \tag{1.18}$$

for the dynamics of the nuclei with mass M, and

$$\mu\frac{d^2}{dt^2}\varphi_i = -\frac{\delta E}{\delta\varphi_i} + \sum_j \lambda_{ij}\varphi_j \tag{1.19}$$

for the evolution of the electrons, where μ is the fictitious electron mass, λ_{ij} the

Lagrange multipliers associated to the orthonormalisation condition of the KS orbitals φ_i, and E is the density functional as per Eqn. (1.3).

1.2.4. Calculating changes in Relative Free Energies

Changes in free energy calculated using static calculations

The Gibbs free energy difference, as considered using static calculations, between each catalytic intermediate is calculated following the method first proposed by Norskov and co-workers.[22,64,65] The structures of the intermediates are optimised in vacuum. The zero-point energy and entropic contributions are included through vibrational analysis performed with the same computational set-up. For every structure optimised in vacuum, solvation effects are accounted for by performing a single point calculation in a water environment simulated with the COSMO model to give E_{solv}. Enthalpies E, zero-point energies ZPE and entropies S of O_2, H_2 and H_2O are also calculated in this manner. Furthermore, as the catalytic cycle proceeds via PCET steps, the free energy of the proton and electron are calculated as a pair: $H^+ + e^- \rightarrow \frac{1}{2} H_2$.

In other words, considering that

$$\Delta G = \Delta E - T\Delta S + \Delta ZPE \tag{1.20}$$

and, because ZPE calculations are more consistently achievable in vacuum, G is approximated by

$$\begin{aligned} G &= (E_{vac} + ZPE_{vac} - TS_{vac}) + \delta E_{solv}, \\ \delta E_{solv} &= E_{solv} - E_{vac}. \end{aligned} \tag{1.21}$$

Then for the first PCET reaction step in Figure 1.2 (b)

$$I_i \longrightarrow I_{i+1} + H^+ + e^-, \tag{1.22}$$

the change in free energy is given by

$$\Delta G(I_i \longrightarrow I_{i+1}) = G(I_{i+1}) - G(I_i) + \Delta G(H^+) + \Delta G(e^-), \tag{1.23}$$

where G is approximated by Eqn. (1.21) and $H^+ + e^-$ by $\frac{1}{2}H_2$.

Using constrained CPMD to calculate changes in free energy

The Gibbs free energy difference, as considered using dynamic calculations, between each catalytic intermediate is calculated following a constrained MD method.[66–68] By constraining a reaction coordinate (in this case the distance

between two atoms) at fixed values along a reaction path, the time-averaged constraint force $\langle\lambda\rangle_x$ for each of these values is obtained. The time-averaged constraint force is equal to zero at an equilibrium or transition state (see Figure 1.4), and it has been shown that $\langle\lambda\rangle$ corresponds to the thermodynamic force $\frac{\partial G}{\partial x}$,[68–70] which may be integrated

$$\int_{x1}^{x2} \langle\lambda\rangle_x \, dx \Rightarrow \Delta G(x1 \rightarrow x2) \qquad (1.24)$$

to give the free energy change along the reaction path.[68–70]

It should be noted that the time-scale of the events observed using this methodology will not be comparable with experiment, though the reaction rate can be extracted using transition state theory.[71]

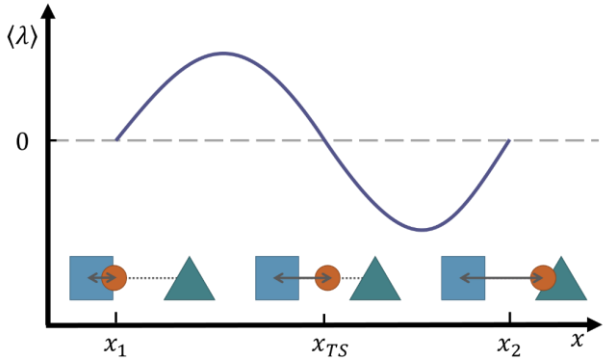

Figure 1.4 The time-averaged constraint force $\langle\lambda\rangle$ as a function of the reaction coordinate x. Here the reaction coordinate is the distance between square and circle as the circle is transferred from the square to the triangle, where x_1 and x_2 are equilibrium states and x_{TS} is the transition state.

1.3. Main Results

The traditional computational methods for establishing a WOC's mechanism are demonstrated in Chapter Two, where a combined experimental and computational analysis is performed on a series of ruthenium-based WOCs. This analysis shows that computational techniques allow for a more in-depth understanding and interpretation of experimental data.

The case for the inclusion of an explicit solvent with regard to mechanistic considerations is given in Chapter Three. There it is observed that including explicit water molecules leads to a different preferred reaction path than would be initially expected by following traditional computational methods. The closed system approach is also introduced, which allows for the decoupling of proton

and electron transfer.

One of the ruthenium-based WOCs investigated in Chapter Two is examined in Chapter Four within an explicit solvent environment including an electron acceptor. Furthermore, the case for a closed system approach is made with regard to energetics. The energetics of the first two catalytic steps are investigated, and taking the energetic contribution of the electron acceptor as constant, these agree with experiment to within 0.1 eV.

Proton diffusion within explicit solvent is further investigated in Chapter Five, where appropriate water wires were observed to facilitate highly rapid proton migration. Furthermore, the inclusion of an OH^- ion as a proton acceptor significantly decreased the thermodynamic barrier of the O – O bond formation step of the earlier investigated ruthenium-based WOC.

1.4. References

[1] B. Christian. "This boat will make its own fuel on a round-the-world voyage" *WIRED UK*. February 20, 2017.
[2] K. Schächtele. "Flying towards a fossil fuel-free future: the HY4 and its plans for zero emission passenger flights" *WIRED UK*. January 12, 2016.
[3] I. Ajjawi *et al. Nat. Biotechnol.* **2017**, *35*, 647–652.
[4] J. O. M. Bockris. *Int. J. Hydrog. Energy* **2013**, *38*, 2579–2588.
[5] J. W. Erisman *et al. Nat. Geosci.* **2008**, *1*, 636–639.
[6] R. Lan *et al. Int. J. Hydrog. Energy* **2012**, *37*, 1482–1494.
[7] N. Armaroli and V. Balzani. *ChemSusChem* **2011**, *4*, 21–36.
[8] A.M. Bazzanella and F. Ausfelder. *Low carbon energy and feedstock for the European chemical industry*; DECHEMA | Gesellschaft für Chemische Technik und Biotechnologie e.V, 2017.
[9] D. Gust *et al. Acc. Chem. Res.* **2009**, *42*, 1890–1898.
[10] K. J. Young *et al. Coord. Chem. Rev.* **2012**, *256*, 2503–2520.
[11] V. W. Lau *et al. Angew. Chem. Int. Ed.* **2017**, *56*, 510–514.
[12] H. L. Tuller. *Mater. Renew. Sustain. Energy* **2017**, *6*, 3.
[13] J. A. Herron *et al. Energy Environ. Sci.* **2015**, *8*, 126–157.
[14] D. Hetterscheid. *Chem. Commun.* **2017**.
[15] J. Hessels *et al. Chem. – Eur. J.* **2017**, *23*, 16413–16418.
[16] P. Garrido-Barros *et al. Chem. Soc. Rev.* **2017**, *46*, 6088–6098.
[17] K. Maeda and K. Domen. *J. Phys. Chem. Lett.* **2010**, *1*, 2655–2661.
[18] A. Thapper *et al. Green* **2013**, *3*, 43–57.
[19] H. Dau *et al. ChemCatChem* **2010**, *2*, 724–761.
[20] H. Dau and M. Haumann. *Biochim. Biophys. Acta BBA - Bioenerg.* **2007**, *1767*, 472–483.
[21] B. Kok *et al. Photochem. Photobiol.* **1970**, *11*, 457–475.
[22] J. Rossmeisl *et al. Chem. Phys.* **2005**, *319*, 178–184.
[23] M. T. M. Koper. *Chem. Sci.* **2013**, *4*, 2710–2723.
[24] I. C. Man *et al. ChemCatChem* **2011**, *3*, 1159–1165.
[25] D. E. Polyansky *et al. J. Am. Chem. Soc.* **2011**, *133*, 14649–14665.
[26] J. D. Blakemore *et al. J. Am. Chem. Soc.* **2010**, *132*, 16017–16029.
[27] T. Wang *et al. J. Chem. Theory Comput.* **2010**, *6*, 2395–2401.
[28] M. D. Kärkäs *et al. Angew. Chem. Int. Ed.* **2012**, *51*, 11589–11593.
[29] A. Venturini *et al. Chem. – Eur. J.* **2014**, *20*, 5358–5368.
[30] M. Orio *et al. Photosynth. Res.* **2009**, *102*, 443–453.

[31] H. A. Younus *et al. ChemSusChem* **2017**, *10*, 862–875.
[32] T. Zhang *et al. J. Am. Chem. Soc.* **2014**, *136*, 273–281.
[33] A. V. Marenich *et al. Angew. Chem. Int. Ed.* **2012**, *51*, 12810–12814.
[34] J. J. Concepcion *et al. J. Am. Chem. Soc.* **2008**, *130*, 16462–16463.
[35] R.-Z. Liao and P. E. M. Siegbahn. *ChemSusChem* **2017**, *10*, 4236–4263.
[36] S. Hammes-Schiffer. *Acc. Chem. Res.* **2009**, *42*, 1881–1889.
[37] C. Ma *et al. ACS Catal.* **2012**, *2*, 1500–1506.
[38] J. L. Vallés-Pardo *et al. ChemPhysChem* **2012**, *13*, 140–146.
[39] T. J. Eisenmayer and F. Buda. *ChemPhysChem* **2014**, *15*, 3258–3263.
[40] M. Swart *et al. Mol. Phys.* **2004**, *102*, 2467–2474.
[41] C. J. Cramer. *Essentials of Computational Chemistry: Theories and Models*; Wiley: Chichester, 2005.
[42] P. J. Stephens *et al. J. Phys. Chem.* **1994**, *98*, 11623–11627.
[43] N. Troullier and J. L. Martins. *Phys. Rev. B* **1991**, *43*, 1993–2006.
[44] O. A. von Lilienfeld *et al. Phys. Rev. Lett.* **2004**, *93*, 153004.
[45] P. J. Hay and W. R. Wadt. *J. Chem. Phys.* **1985**, *82*, 270–283.
[46] P. J. Hay and W. R. Wadt. *J. Chem. Phys.* **1985**, *82*, 299–310.
[47] W. R. Wadt and P. J. Hay. *J. Chem. Phys.* **1985**, *82*, 284–298.
[48] G. te Velde *et al. J. Comput. Chem.* **2001**, *22*, 931–967.
[49] SCM. *ADF 2012*; Theoretical Chemistry, Vrije Universiteit, Amsterdam, The Netherlands.
[50] C. F. Guerra *et al. Theor. Chem. Acc.* **1998**, *99*, 391–403.
[51] *CPMD*; Copyright IBM Corp 1990-2008, Copyright MPI für Festkörperforschung Stuttgart 1997-2001.
[52] I.-C. Lin *et al. Phys. Rev. B* **2007**, *75*, 205131.
[53] L. Kleinman and D. M. Bylander. *Phys. Rev. Lett.* **1982**, *48*, 1425–1428.
[54] S. Grimme *et al. J. Comput. Chem.* **2011**, *32*, 1456–1465.
[55] A. Klamt. *COSMO-RS: From Quantum Chemistry to Fluid PhaseThermodynamics and Drug Design*; Elsevier Science: Amsterdam, 2005.
[56] J. Tomasi *et al. Chem. Rev.* **2005**, *105*, 2999–3094.
[57] E. Runge and E. K. U. Gross. *Phys. Rev. Lett.* **1984**, *52*, 997–1000.
[58] M. E. Casida and M. Huix-Rotllant. *Annu. Rev. Phys. Chem.* **2012**, *63*, 287–323.
[59] N. T. Maitra. *J. Chem. Phys.* **2016**, *144*, 220901.
[60] S. J. A. van Gisbergen *et al. J. Chem. Phys.* **1995**, *103*, 9347–9354.
[61] C. A. Ullrich. *Time-Dependent Density-Functional Theory : Concepts and Applications*; Oxford Graduate Texts; OUP Oxford: Oxford, 2011.
[62] R. Car and M. Parrinello. *Phys. Rev. Lett.* **1985**, *55*, 2471–2474.
[63] D. Marx and J. Hutter. *Ab Initio Molecular Dynamics: Basic Theory and Advanced Methods*, 1 edition.; Cambridge University Press: Cambridge ; New York, 2009.
[64] J. K. Nørskov *et al. J. Phys. Chem. B* **2004**, *108*, 17886–17892.
[65] J. Rossmeisl *et al. J. Electroanal. Chem.* **2007**, *607*, 83–89.
[66] B. Ensing *et al. J. Phys. Chem. A* **2001**, *105*, 3300–3310.
[67] F. Costanzo and R. G. Della Valle. *J. Phys. Chem. B* **2008**, *112*, 12783–12789.
[68] M. Sprik and G. Ciccotti. *J. Chem. Phys.* **1998**, *109*, 7737–7744.
[69] W. K. den Otter and W. J. Briels. *J. Chem. Phys.* **1998**, *109*, 4139–4146.
[70] L. Bernasconi *et al. ACS Catal.* **2017**, *7*, 4018–4025.
[71] D. Frenkel and B. Smit. *Understanding Molecular Simulation: From Algorithms to Applications*, 2nd ed.; Academic Press: California, 2001.

The Fundamentals: A Combined Experimental & Theoretical Study

Chapter Two

2. The Fundamentals: A Combined Experimental and Theoretical Study

Abstract

When designing a WOC it is crucial to establish the catalytic mechanism and the intermediates of the catalytic cycle, but a full description is often difficult to obtain using only experimental data. A combination of DFT, radiation chemistry, spectroscopic techniques and electrochemistry is used to establish the water oxidation mechanism of a series of mononuclear ruthenium water oxidation catalysts. The comparison between the calculated absorption spectra of the proposed intermediates with experimental ones, as well as free-energy calculations with electrochemical data, provides strong evidence for the proposed catalytic pathway: a water oxidation catalytic cycle involving four PCET steps. The thermodynamic bottleneck is identified in the third PCET step involving the O-O bond formation. The good agreement between the optical and thermodynamic data with DFT predictions further confirms that this methodology should be considered fundamental for the characterisation of water oxidation catalysts.

This chapter is based on

J. M. de Ruiter, R. L. Purchase, A. Monti, C. J. M. van der Ham, M. P. Gullo, K. S. Joya, M. D'Angelantonio, A. Barbieri, D. G. H. Hetterscheid, H. J. M. de Groot, and F. Buda "Electrochemical and Spectroscopic Study of Mononuclear Ruthenium Water Oxidation Catalysts: A Combined Experimental and Theoretical Investigation."
ACS Catalysis, **2016**, doi: 10.1021/acscatal.6b02345

2.1. Introduction

A full description of WOC mechanisms underlying catalytic activity is not always accessible experimentally. A computational description of each intermediate state plays a crucial role in the prediction of catalytic behaviour throughout the entire cycle and provides complementary information for the interpretation of experimental observations. Concurrently, the computational approach also needs to be validated with experimental data. Initially, it was supposed that only multinuclear complexes would be able to supply the oxidation potential needed to catalyse water splitting, in analogy with the four Mn complex in the oxygen evolving centre of PS II.[1,2] As a result, several molecular catalysts have been developed with two or more metal sites.[1,3–8] However, an increasing amount of effort has been directed towards developing mononuclear WOCs.[1,9] A large number of ruthenium[1,10–18] and iridium[1,5,19–25] based catalysts have been reported. DFT has been used extensively to predict the reaction mechanisms and the electronic properties of several multi- and mono-nuclear molecular catalysts.[5,6,11,15,16,25]

We recently investigated the WOC $[Ru(cy)(bpy)(H_2O)]^{2+}$ (cy = *p*-cymene, bpy = 2,2'-bipyridine; Scheme 2.1 (*Ru*-bpy)).[14,26] It has been shown that the immobilization of this Ru-based catalyst, modified with surface anchoring units, on a $BiVO_4$ light-absorber enhances the performance of this photoanode.[26] The proposed catalytic cycle for water oxidation involves four PCET steps as depicted in Scheme 2.1.[27] Here we study this *Ru*-bpy catalyst and several derivative catalysts of the form $[Ru(cy)(L)(H_2O)]^{2+}$ (Figure 2.1) by means of a combination of theoretical and experimental techniques, expanding on previously described strategies.[15]

We verify the stability of this class of catalysts under oxidative conditions using

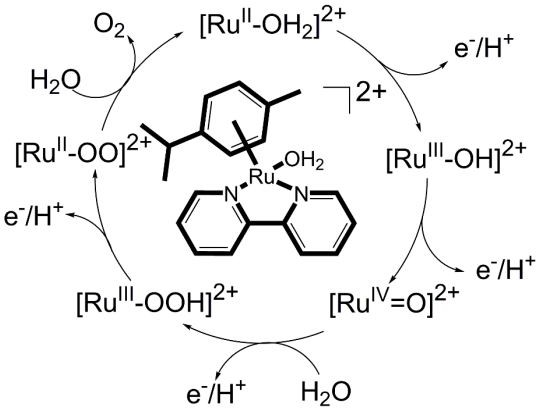

Scheme 2.1 Proposed catalytic cycle for water oxidation by *Ru*-bpy. Inset: Schematic structure of *Ru*-bpy.

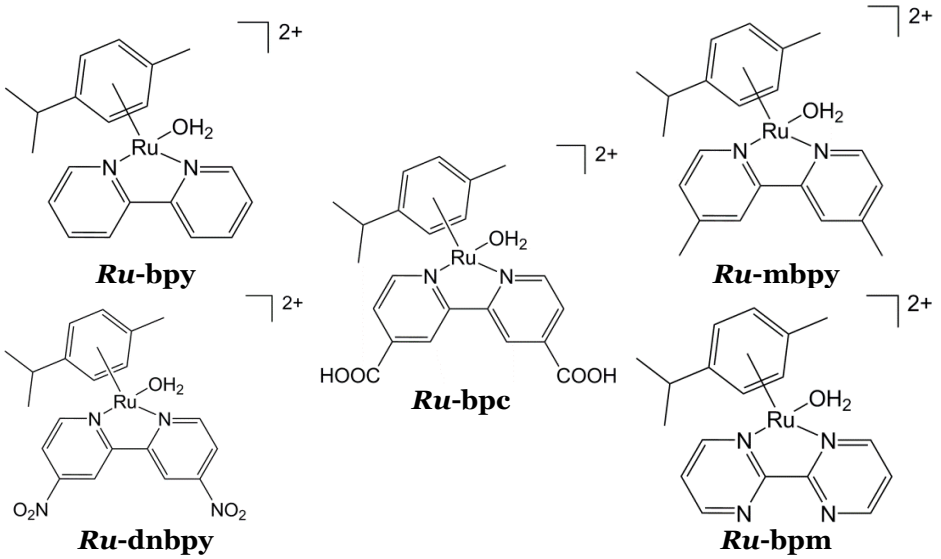

Figure 2.1 Schematic structures of the investigated catalysts: 2,2′-bipyridine (*Ru*-bpy), 4,4′-disubstituted-2,2′-bipyridine (*Ru*-bpc, *Ru*-mbpy, *Ru*-dnbpy) and 2,2′-bipyrimidine (*Ru*-bpm) Ru(*p*-cymene) complexes.

OLEMS and SERS.[28] The proposed catalytic mechanism is validated by comparing the computed free-energy differences between the intermediates in the catalytic cycle and those derived from electrochemical measurements. The absorption spectra predicted by TDDFT calculations for each intermediate in the catalytic cycle are used to interpret the results obtained from stopped-flow and pulse radiolysis measurements, confirming that the proposed cycle can explain experimental observation. Finally, the ability of TDDFT calculations to reproduce absorption spectra for three derivative catalysts confirms the general applicability of this methodology as a powerful tool for the characterisation of WOCs and for the interpretation of experimental observables.

2.2. Experimental Methods

The synthesis of the starting compounds has been described in an earlier thesis published by this group.[29]

Online Electrochemical Mass Spectrometry (OLEMS)

OLEMS experiments were performed using a set up that has been previously described.[28,30] The electrochemical cell used for these experiments is a two compartment cell with three electrodes: a gold bead electrode (diameter 3 mm) and a gold wire were used as the working and counter electrodes, respectively; the reference electrode was an RHE separated from the main cell by a Luggin capillary. Before each measurement, the working electrode was electrochemically cleaned: the electrode was first oxidised in 10% sulfuric acid by applying 10 V for

30 s, using a graphite bar as the counter electrode. Subsequently the gold oxide formed was removed by dipping the working electrode in a 6 M HCl solution for 30 s. The electrode was then flame annealed and cycled 200 times from 0 – 1.75 V (vs. RHE) at 1 V/s in 0.1 M $HClO_4$. The gold counter electrode was flame annealed. A 0.1 M solution of phosphate buffer (pH 7) was prepared from Na_2HPO_4 and NaH_2PO_4. *Ru*-bpc was dissolved in the buffer solution at a concentration of 1 mM and OLEMS measurements were made with the catalyst in solution.

Surface Enhanced Raman Spectroscopy

In situ SERS electrochemistry was performed on a set up that has been previously described.[28,31,32] The electrochemical cell has two compartments and three electrodes: a roughened gold surface as the working electrode, a gold wire as the counter electrode, and the reference electrode was an RHE separated from the main cell by a Luggin capillary. The gold working electrode was first electrochemically cleaned using the process described above for the OLEMS measurements and then subsequently electrochemically roughened by 25 oxidation–reduction cycles in a 0.1 M solution of KCl. The oxidation–reduction cycles were performed between −0.30 and 1.20 V vs SCE, during which the potential was held for 30 s at the negative limit and for 1.3 s at the positive limit, a method reported to give a brownish surface that is SERS active.[33] 1 mg *Ru*-bpc was dissolved in methanol. A neutral Na-exchanged Nafion solution was prepared by mixing one part of Nafion (5% wt, 1000 equiv/g, Sigma-Aldrich) with one part of 0.05 M NaOH.[34] One part of the catalyst solution was mixed with one part of Na-exchanged Nafion solution. 15 µL of this mixture was dropcast on the gold working electrode and dried under vacuum for use in the in situ SERS electrochemical measurements.

UV-Vis Spectroscopy and Stopped Flow analysis

Absorption spectra of the $[Ru(cy)(L)(H_2O)]^{2+}$ complexes ($c = 5\times10^{-5}$ M) for both molar absorptivity measurements and kinetic analysis were recorded with a Perkin-Elmer Lambda 950 UV/Vis/NIR spectrophotometer. The kinetic analysis was performed using an Applied Photophysics stopped-flow system configured for two-syringe mixing (RX.2000 Stopped-Flow Mixing Accessory). The initial concentrations of reactants in the syringes were fixed to 10^{-4} M for Ru(II) complexes in every experiment and from 1×10^{-4} M to 10×10^{-4} M for Ce^{IV} ($[Ce(NH_4)_2(NO_3)_6]$, CAN, Sigma-Aldrich), depending on the different Ru/Ce ratio (1:1; 1:2; 1:4 and 1:10). The spectral evolution was recorded after equal amounts of both solutions were mixed in a 1 cm optical path length stopped-flow cell. The dead time of the mixing setup was 8 ms.

Pulse radiolysis

Pulse radiolysis[35] with optical absorption detection was performed using a

12 MeV linear accelerator, which delivered 100 - 200 ns electron pulses with doses between 4 and 82 Gy.[36] The pulse irradiations were performed at room temperature (22 ± 2 °C) on samples in Spectrosil quartz cells of 2 cm optical path length. Solutions were protected from the analysing light with a shutter and cut-off filters. The bandwidth used throughout the pulse radiolysis experiments was 5 nm. The radiation dose per pulse was monitored with a charge collector placed behind the irradiation cell and calibrated with an N_2O-saturated solution containing 0.1 M HCO_2^- and 0.5 mM methylviologen ($MV^{+\bullet}$), using $G(MV^{+\bullet}) = 0.7\times10^{-6}$ mol J^{-1} at 605 nm, where $G(x)$ represents the number of moles of species x formed, consumed or altered per joule of energy absorbed by the system.[37]

The radiolysis of water yields solvated electrons (e_{aq}^-), hydroxyl radicals ($^\bullet OH$) and hydrogen atoms ($H^\bullet$) as primary radical species, which are responsible for the production of the several active species in solution.[38] The oxidants used in the experiments here were $SO_4^{\bullet-}$ and $CO_3^{\bullet-}$. They were chosen for their high standard redox potentials of 2.43 and 1.5 V (vs. NHE), respectively.[39–41] $SO_4^{\bullet-}$ radicals were generated by pulse radiolysis of a $K_2S_2O_8$ (10 mM) solution de-aerated with Argon, at pH=1.4 adjusted by adding concentrated $HClO_4$, in the presence of 0.1 M *t*-BuOH as $^\bullet OH$ radical scavenger. $CO_3^{\bullet-}$ radicals were generated by pulse radiolysis of $Na_2CO_3/NaHCO_3$ (5 mM : 5 mM, pH = 10) solution saturated with N_2O. The mechanisms for the production of the radicals is described by Polyansky et al.[41]

2.2.1. Computational method and details

Geometry optimisations, thermodynamic and TDDFT calculations are performed using the ADF software package.[42–44] Van der Waals interactions are accounted for by using the Grimme3 BJDAMP dispersion correction.[45] Unless stated otherwise the geometries of the examined molecules are optimised using the OPBE functional,[46] with the TZP basis set and a small core. This GGA functional has shown good performance when describing transition metal complexes.[14,47–49] TDDFT excited state calculations are performed with the B3LYP functional combined with the TZP basis set.[50] In both the geometry optimization and the TDDFT calculations, the solvation effect of water is included by means of COSMO.[51] All calculations are spin unrestricted and the energetically most stable multiplicity is checked when necessary (see Table A2.1).

This computational set-up is employed in test calculations performed on a ruthenium-based benchmark WOC, for which experimental data is available for comparison.[15] The results shown in the Supporting Information (Figure A2.1 and Table A2.2) validate the ability of this method to accurately reproduce the optical properties of compounds chemically similar to the WOC of interest in this study.

The thermodynamics of the catalytic cycle is obtained by calculating the Gibbs free energy difference between each catalytic intermediate following the method

first proposed by Norskov and co-workers.[52–54] The structure of each intermediate is optimised at the B3LYP/TZP level, in vacuum. Zero-point energy and entropic contributions are included through vibrational analysis performed with the same computational set-up. For every structure optimised in vacuum, solvation effects are accounted for by performing a single point calculation with the B3LYP functional in a water environment simulated with the COSMO model. Reaction energies, zero-point energies and entropies of O_2, H_2 and H_2O are also calculated in this manner. Furthermore, as the catalytic cycle proceeds via PCET, the free energy of the proton and electron are calculated as a pair: $H^+ + e^- \rightarrow ½\ H_2$.

Raman frequency calculations, after re-optimisation of the geometries, are performed with Gaussian '09,[55] using the B3LYP functional and LANL2DZ basis set.[56–58] In Gaussian '09 calculations, this basis set has been shown to be an effective descriptor for ruthenium complexes.[59,60]. Solvation effects are included with the PCM model for water,[61] while anharmonic corrections were not included. The resulting output is visualised with the help of the GaussSum program.[62]

2.3. Results and Discussion

2.3.1. Characterisation of the catalytic intermediates of *Ru*-bpc

Catalyst stability

The stability of similar WOC complexes under oxidative conditions has been under scrutiny in the literature due to the possible oxidative degradation and loss of the ligands.[63,64] In particular, evidence of catalyst degradation has been reported for Ir-Cp* complexes (Cp* = cyclopentandienyl).[63,64] These results appear to be strongly affected by the chemical oxidant used in the study, most often CAN or Sodium Periodate $NaIO_4$.[63–74] More recently it has been shown that the Cp* complex remains intact at the initial stages of the water oxidation reaction in the case of $[Ir(Cp^*)(Me_2NHC)(Cl)_2]$.[28]

To establish the stability of the Ru-based catalysts analysed in this work, we use OLEMS monitoring *in situ* the production of O_2 and CO_2 concurrently with time dependent electrolysis.[28] In this way it is possible to check whether the organic moieties in the complex decompose during catalytic oxygen evolution. Figure 2.2 shows the current signal and the mass signals for O_2 (m/z 32) and CO_2 (m/z 44).

Figure 2.2 shows that when the potential is raised to a value above 0.8 V where water oxidation begins (see also Table 2.1), then there is a marked increase in current and oxygen is evolved. In contrast, there is little change in the CO_2 signal. These results show that *Ru*-bpc forms negligible amounts of carbon dioxide under

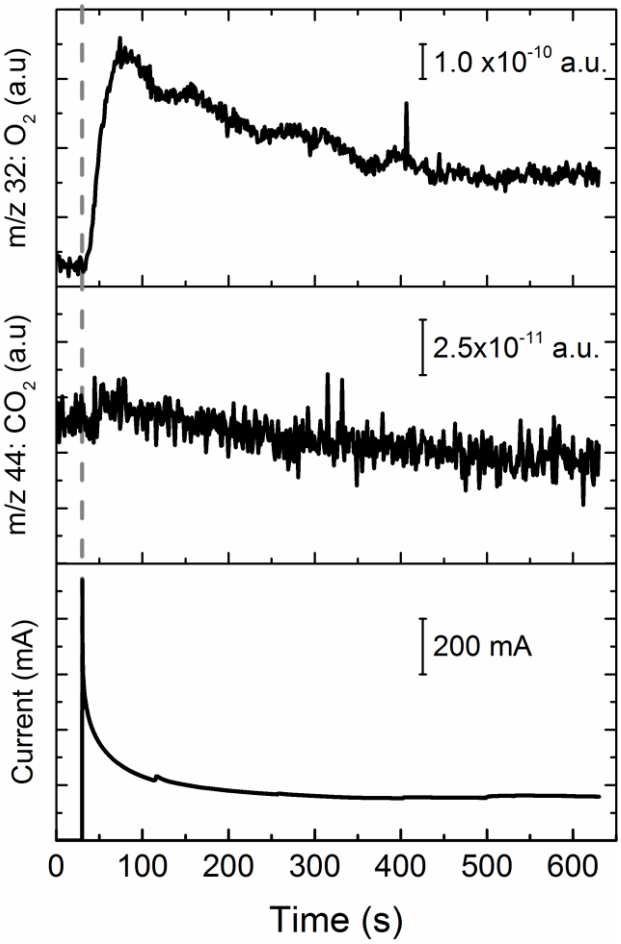

Figure 2.2 OLEMS signals acquired during electrochemical water oxidation as catalysed by *Ru*-bpc. The potential is initially set at 0.8 V (vs NHE) then increased to 1.8 V at 30 s (indicated by the dashed grey line).

oxidizing conditions, strongly suggesting that the organic ligands are stable, or at least do not degradate all the way to CO_2. The instantaneous evolution of dioxygen as soon as a sufficiently high potential is applied, illustrates that *Ru*-bpc itself is the active species in the oxygen evolution reaction at early stages of the water oxidation reaction.[75] We cannot rule out that the cymene ligand de-coordinates after prolonged electrolysis under the harsh oxidative conditions and the decrease in oxygen evolution rates after the initial burst may actually point to such an event. Since we do not detect significant amounts of CO_2 under these circumstances, this indicates that *Ru*-bpc does not degradate all the way to ruthenium oxide under the employed conditions. This is also consistent with our previous investigation involving the use of highly sensitive in-situ EQCN experiments showing no sign of ruthenium oxide generation during the catalytic reaction of water oxidation.[30]

Electrochemical and Thermodynamic investigation

Electrochemical investigations and CV had previously been performed for the *Ru*-bpc and *Ru*-bpy complexes.[29] To assign a specific redox couple to each electronic wave observed in the CV analyses, we compute with DFT the Gibbs free energy differences between consecutive catalytic intermediates according to the proposed cycle presented in Scheme 2.1. As shown in Table 2.1 and Figure 2.3 the theoretical calculations show good agreement with the experimentally observed trend. Consistent with the experimental data, the third step from $[Ru^{IV}=O]^{2+}$ to $[Ru^{III}\text{-}OOH]^{2+}$ (which involves the formation of the O – O bond) shows the largest ΔG, and thereby forms the thermodynamic bottleneck of the system. This thermodynamic bottleneck gives an overpotential of about 0.6 V for both *Ru*-bpc and *Ru*-bpy, as estimated from the electrochemical data (see Table 2.1). As the $[Ru^{II}\text{-}OO]^{2+}$ intermediate cannot be observed experimentally, it is not possible to comment on the redox value calculated for it. It is interesting to note that the DFT results predict the final step involving the ligand exchange of O_2 with H_2O on the Ru site to be thermodynamically spontaneous with a ΔG= -0.42 eV for *Ru*-bpc and ΔG= -0.15 eV for *Ru*-bpy, contrary to the general assumption that this exchange is thermodynamically neutral.[54]

The comparison of the thermodynamic analysis of the two catalysts *Ru*-bpc and *Ru*-bpy (see Table 2.1) shows that the substitution of a COOH group for H seems to have little effect on the potentials at which the PCET steps occur. The two catalysts only differ by around 0.1 eV when comparing the measured ΔG values for each catalytic step. We do notice however that the DFT method used seems to

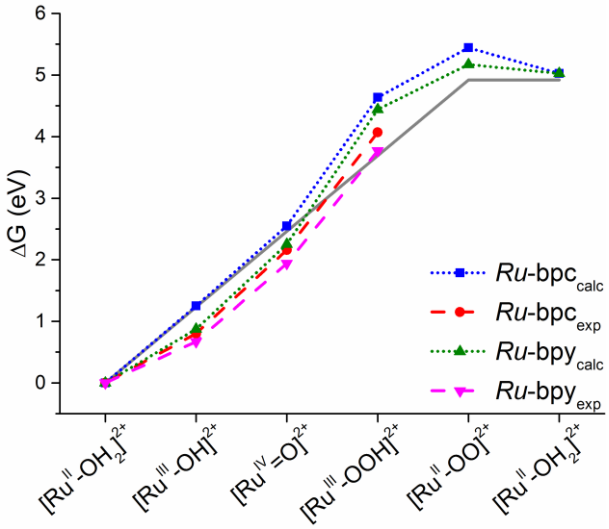

Figure 2.3 Free energy difference between intermediates along the catalytic pathway of the *Ru*-bpy catalyst. DFT results (blue and green) are compared with the values extracted from electrochemical data (red and pink). We also show, as a visual guide, a constant change of 1.23 eV for all four PCET steps (grey line).

Table 2.1 Calculated ΔG for each catalytic step along the proposed catalytic mechanism, as compared to the experimentally measured ΔG for *Ru*-bpc and *Ru*-bpy adjusted to E_0 according to the Nernst equation $E = E_0 - 0.059\,pH$, where the potential E is measured at a certain pH.

	ΔG_{calc} ***Ru*-bpc (eV)**	ΔG_{exp} ***Ru*-bpc (eV)**
$[Ru^{II}\text{-}OH_2]^{2+} \rightarrow [Ru^{III}\text{-}OH]^{2+}$	1.25	0.80
$[Ru^{III}\text{-}OH]^{2+} \rightarrow [Ru^{IV}{=}O]^{2+}$	1.30	1.36
$[Ru^{IV}{=}O]^{2+} \rightarrow [Ru^{III}\text{-}OOH]^{2+}$	2.09	1.91
$[Ru^{III}\text{-}OOH]^{2+} \rightarrow [Ru^{II}\text{-}OO]^{2+}$	0.81	-
$[Ru^{II}\text{-}OO]^{2+} \rightarrow [Ru^{II}\text{-}OH_2]^{2+}$	-0.42	-
$2H_2O \rightarrow 2H_2 + O_2$	5.02	4.92

	ΔG_{calc} ***Ru*-bpy (eV)**	ΔG_{exp} ***Ru*-bpy (eV)**
$[Ru^{II}\text{-}OH_2]^{2+} \rightarrow [Ru^{III}\text{-}OH]^{2+}$	0.87	0.67
$[Ru^{III}\text{-}OH]^{2+} \rightarrow [Ru^{IV}{=}O]^{2+}$	1.38	1.27
$[Ru^{IV}{=}O]^{2+} \rightarrow [Ru^{III}\text{-}OOH]^{2+}$	2.19	1.83
$[Ru^{III}\text{-}OOH]^{2+} \rightarrow [Ru^{II}\text{-}OO]^{2+}$	0.73	-
$[Ru^{II}\text{-}OO]^{2+} \rightarrow [Ru^{II}\text{-}OH_2]^{2+}$	-0.15	-
$2H_2O \rightarrow 2H_2 + O_2$	5.02	4.92

over-stabilise the initial state of *Ru*-bpc leading to a deviation of 0.45 eV for the $[Ru^{II}\text{-}OH_2]^{2+} \rightarrow [Ru^{III}\text{-}OH]^{2+}$ step. This is also reflected in the ΔG values calculated for the final ligand exchange mentioned earlier: that calculated for *Ru*-bpc is 0.3 eV more negative than that calculated for *Ru*-bpy. It is noted that the initial state has also been shown to be the most dependent on the choice of functional.[76] Apart from the steps affected by the over-stabilisation of the initial state of *Ru*-bpc, the calculated ΔG values for both catalysts differ less than 0.1 eV. The $[Ru^{III}\text{-}OH]^{2+} \rightarrow [Ru^{IV}{=}O]^{2+}$ step as calculated for *Ru*-bpc agrees to 0.1 eV with the experimental measurement, while a larger deviation (0.2 eV) is observed for the $[Ru^{IV}{=}O]^{2+} \rightarrow [Ru^{III}\text{-}OOH]^{2+}$ step. This step has the largest deviation between calculated and experimental values for the *Ru*-bpy catalyst, while the experimental values for the first two catalytic steps are reproduced with an error ≤ 0.2 eV.

In Table 2.1 we also note the computed ΔG associated to the hydrolysis process; this corresponds to the sum of all the ΔG contributions in the complete catalytic cycle. This result deviates only by 0.1 eV with respect to the experimental value of 4.92 eV, thereby providing a further indication that the chosen computational method and set-up is sufficiently accurate in its description of the water oxidation reaction.

SERS and Raman frequency calculations

To verify the presence of the expected catalytic intermediates, SERS measurements were conducted stepwise from -0.4 V up to 1.0 V. Owing to the oxidation of the gold electrode, it was not possible to measure SERS spectra at the potentials needed to drive the catalyst through the bottleneck of the third PCET step. After measuring up to 1.0 V, another spectrum was measured at -0.3 V that shows recovery of the initial species. This further indicates that the catalyst remains intact during the initial stages of the water oxidation reaction.

When considering the SERS spectra (Figure 2.4) three distinct potential ranges (-0.4 – 0.1 V, 0.2 – 0.5 V, 0.6 – 1.0 V) can be identified. The potentials at which these ranges change (0.2 and 0.6 V) are the same as the potentials assigned to the transition from one catalytic intermediate to the next (adjusted for pH 7.35).

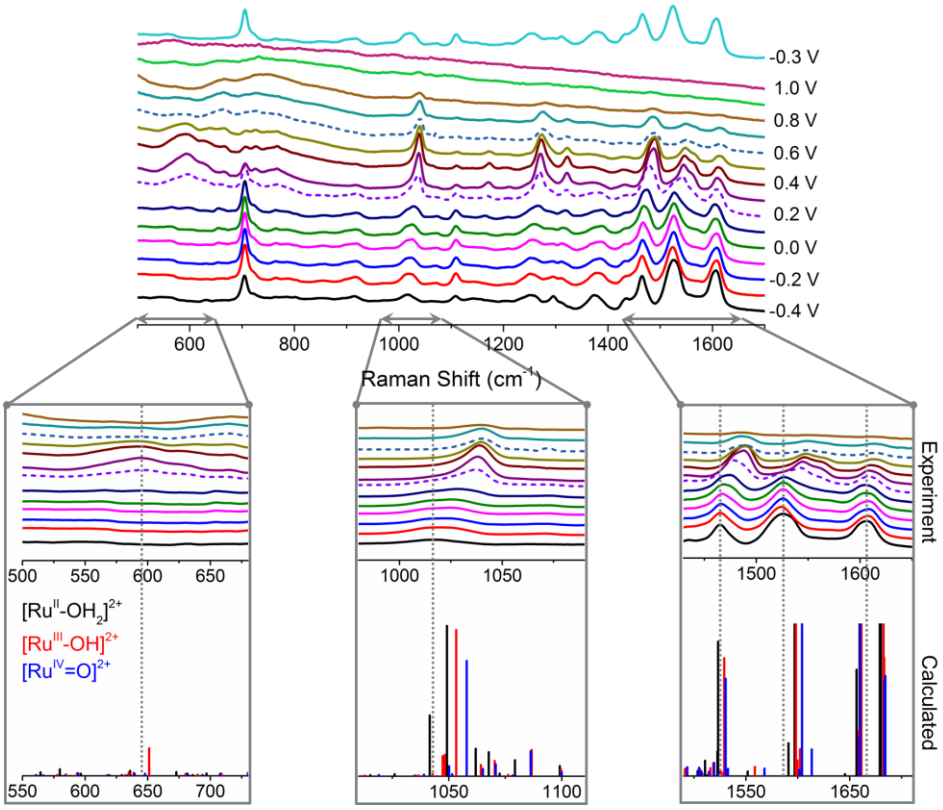

Figure 2.4 (Top) SERS spectra of Ru-bpc. Spectra are obtained by increasing the potential stepwise to 1.0 V, after which a measurement is performed at -0.3 V. The dotted lines indicate the potential at which significant changes are observed. (Bottom panels) Selected regions of SERS spectra of Ru-bpc are compared to computed Raman frequencies and intensities for the three intermediates $[Ru^{II}\text{-}OH_2]^{2+}$ (black), $[Ru^{III}\text{-}OH]^{2+}$ (red) and $[Ru^{IV}=O]^{2+}$ (blue). The grey dotted lines indicate areas in which changes in the Raman spectrum can be linked to different intermediates.

Considering the potential range for which SERS is conducted, it is expected that only the $[Ru^{II}\text{-}OH_2]^{2+}$, $[Ru^{III}\text{-}OH]^{2+}$ and $[Ru^{IV}=O]^{2+}$ species will be identifiable. Raman frequency spectra calculated using Gaussian '09 for these three species are compared to three different selected frequency regions of the SERS spectra in the lower panels of Figure 2.4.

In the region 500 – 680 cm^{-1}, a broad shoulder appears at 0.2 V, then decays above 0.6 V. In this region, the theoretical spectra shows only one mode attributed to the Ru-OH stretch of the $[Ru^{III}\text{-}OH]^{2+}$ species. The Ru-O stretch of the $[Ru^{II}\text{-}OH_2]^{2+}$ species is expected at lower frequencies and as such is not observed experimentally, while the stiffer Ru=O stretch is expected around 830 cm^{-1}. In the 1010 – 1110 cm^{-1} region, a peak is observed around 1015 cm^{-1} at -0.4 V, which shifts to higher frequency at 0.2 V, then slowly decays and shifts to slightly higher frequencies. Based on the DFT calculations, this peak is assigned to the Ru-N stretch, which becomes stiffer as the oxidation state of the Ru increases. This trend is also shown in the theoretical calculations (see lower panels of Figure 4).

The effect of the increasing oxidation state of Ru on the bonds to the bipyridine ligand is also seen in the region between 1430 and 1670 cm^{-1}. The predicted frequencies are ~5 % higher than the measured values, which is within a typical error at the DFT/B3LYP level of theory. Nevertheless, the trends between calculation and experiment are definitely comparable. Calculation identifies the peak around 1475 cm^{-1} as being due to the carbon-carbon stretch bridging the two pyridines. This mode is therefore more influenced by the changing Ru oxidation state than the other bipyridine hydrogen wags which are calculated at around 1600 cm^{-1}. This is demonstrated in the larger shift towards a stiffer mode as the oxidation state increases for the 1475 cm^{-1} peak. Experiment and calculation show good agreement in this trend. Comparing the calculated Raman modes of *Ru*-bpc to *Ru*-bpy (see Figure A2.2) one can notice that the COOH groups lead to a number of additional bipyridine modes, due to the additional symmetric and asymmetric stretches possible in the COOH group.

Calculation also correctly predicts the appearance of a shoulder at increasing potentials for the peak observed at 1525 cm^{-1}. This shoulder is due to stiffer cymene modes resulting from stronger coordination to Ru as the catalyst proceeds through the initial steps of the catalytic cycle and Ru becomes more positive. Thus, by comparing SERS measurements and Raman frequency calculations the presence of the proposed early catalytic intermediates is further established.[65,77]

Optical absorption and TDDFT calculations

Further investigation of the expected catalytic intermediates is conducted by comparing experimental absorption spectra with TDDFT calculations for the

singly- and doubly-oxidised forms proposed for *Ru*-bpc. The absorption of a *Ru*-bpc solution to which an excess of the oxidant CAN is added (Ru/Ce ratio = 1:10) is measured over time. After 24 hours two peaks not seen before the introduction of the oxidant were observed. It is noteworthy that the addition of a more moderate excess of CAN (Ru/Ce ratio = 1:4) produced absorption spectra with the same shape as those reported for a ratio 1:10. In Figure 2.5 the experimental spectra are compared to TDDFT B3LYP spectra calculated for $[Ru^{II}\text{-}OH_2]^{2+}$ and the catalytic intermediates, $[Ru^{III}\text{-}OH]^{2+}$ and $[Ru^{IV}{=}O]^{2+}$. The peak characteristic of Ce^{IV} (around 320 nm) was also investigated over time in experiments conducted with *Ru*-bpy, decreasing in intensity as shown in Figure A2.3. Calculated spectra for all the proposed *Ru*-bpy catalytic intermediates are also shown in Figure A2.4.

The spectrum measured before addition of CAN (Figure 2.5, top, black line) shows good agreement with the one calculated for the starting species, $[Ru^{II}\text{-}OH_2]^{2+}$ (Figure 2.5, bottom, black line). In both experimental and calculated spectra a signal peaking around 380 nm and tailing over 450 nm is observed. This band is commonly detected in *arene*-Ru^{II} complexes with one bidentate bipyridyl ligand,[78] and is attributed to a MLCT transition. The nature of such transition is well described by TDDFT (see Figure A2.5). The intense band at wavelengths shorter than 350 nm, assigned to a ligand-centred transition,[78] is also well reproduced by B3LYP.

The spectrum measured 24 hours after the introduction of 10 equivalents of CAN (Figure 2.5, top, red line) can be interpreted by comparison with the TDDFT

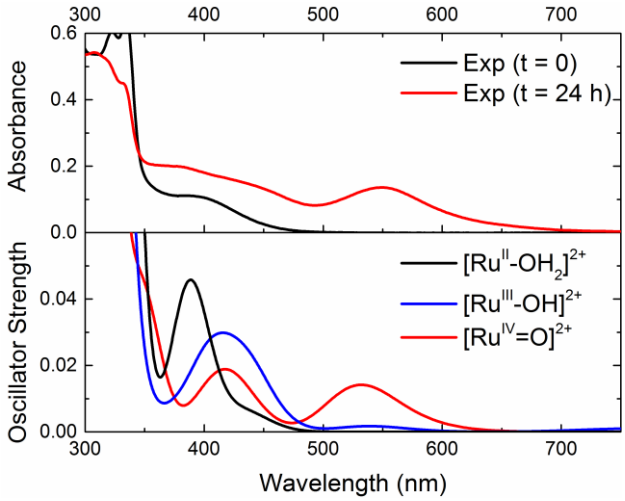

Figure 2.5 (Top) Experimental absorption spectra of *Ru*-bpc initially in acid (black line) and after 24 hours upon addition of 10 equivalents of CAN (red line). This is compared to the TDDFT spectra (bottom) of $[Ru^{II}\text{-}OH_2]^{2+}$ (black), $[Ru^{III}\text{-}OH]^{2+}$ (blue) and $[Ru^{IV}{=}O]^{2+}$ (red). The calculated spectra have a Gaussian width broadening of 0.3 eV.

results obtained for the intermediates $[Ru^{III}\text{-}OH]^{2+}$ (Figure 2.5, bottom, blue line) and $[Ru^{IV}=O]^{2+}$ (Figure 2.5, bottom, red line). The best comparison is observed with the spectrum calculated for the catalytic intermediate $[Ru^{IV}=O]^{2+}$, obtained after two PCET steps, showing a peak around 530 nm which is associated to a metal centred d-d transition (see Figure A2.7). This peak is characteristic of the intermediate $[Ru^{IV}=O]^{2+}$ and deviates by only ~0.15 eV from the experimental peak observed around 550 nm. This deviation between experiment and theory is within a typical average error for TDDFT calculations using the B3LYP functional. A small shoulder tails off at 600 nm, which can be associated with the tail of the measured spectrum. Furthermore, the energetically higher experimental shoulder observed around 400 – 450 nm matches well with a peak calculated for $[Ru^{IV}=O]^{2+}$. It should be noted that although a peak around the same wavelength is also predicted for the intermediate $[Ru^{III}\text{-}OH]^{2+}$, there is no experimental evidence of Ru^{III} formation during chemical oxidation with CAN. This is due to its conversion into a $[Ru^{IV}=O]^{2+}$ species at a rate faster than the time resolution of the stopped flow apparatus (t < 2 ms).[15,74]

This analysis suggests that with the excess CAN oxidant used, the catalytic process has stopped after the first two PCET steps at the $[Ru^{IV}=O]^{2+}$ intermediate. This result reflects that the third PCET step from $[Ru^{IV}=O]^{2+}$ to $[Ru^{III}\text{-}OOH]^{2+}$ requires a driving force larger than the oxidative power of CAN (~1.75 eV).[68] Without a stronger applied overpotential, the catalyst will not be able to cross the potential barrier imposed by the formation of the peroxide bond, leaving $[Ru^{IV}=O]^{2+}$ as stable final product.

2.3.2. Derivative catalysts

The derivative catalysts *Ru*-bpy, *Ru*-mbpy, *Ru*-dnbpy and *Ru*-bpm are also studied using spectroscopic measurements and TDDFT calculations following the same procedure described for the *Ru*-bpc case. The results are shown in Figure 2.6. Like the spectra discussed earlier for *Ru*-bpc, each of the derivative compounds before addition of 10 eq. CAN (Exp t = 0 in Figure 2.6) show an intense peak at wavelengths less than 350 nm, accompanied by a less intense peak which appears as a shoulder tailing to 500 nm (see also Table A2.3 and Figure A2.8). For *Ru*-bpy and *Ru*-mbpy, a clear peak is also observed around 550 nm 24 hours after addition of CAN (Exp t = 24 h, Figure 2.6). The computed absorption spectra for the $[Ru^{IV}=O]^{2+}$ intermediate of these two derivatives also show a very good agreement in the position of the peaks seen experimentally after 24 hours. The values computed for the primary excitations of the $[Ru^{IV}=O]^{2+}$ intermediate indicate that the peak arising after 24 hours around 550 nm is characteristic of that specific catalytic state (Table 2.2). Overall, these results show the importance of TDDFT calculations for the interpretation of the catalytic cycle.

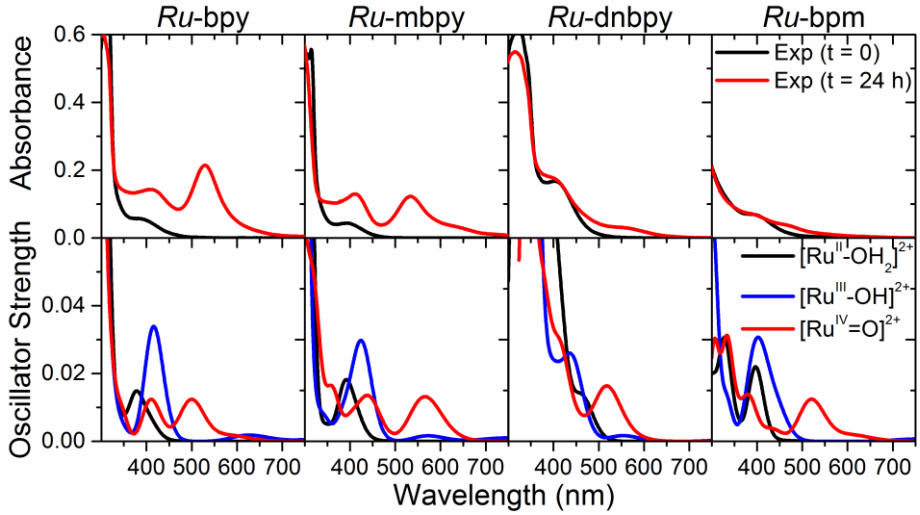

Figure 2.6 (Top) Experimental absorption spectra of different derivative catalysts initially in acid (black line) and after 24 hours upon addition of 10 equivalents of CAN (red line). This is compared to the TDDFT spectra (bottom) of $[Ru^{II}\text{-}OH_2]^{2+}$ (black), $[Ru^{III}\text{-}OH]^{2+}$ (blue) and $[Ru^{IV}=O]^{2+}$ (red). The calculated spectra have a Gaussian width broadening of 0.3 eV.

It should be noted that for *Ru*-bpm and *Ru*-dnbpy the characteristic peak around 550 nm is not observed as distinctly as for *Ru*-bpc and *Ru*-bpy. An approximation was made as to the wavelength for the *Ru*-dnbpy absorbance by considering the shoulder starting around 625 nm. However, the spectrum of *Ru*-bpm appears to have no significant absorbance in this region, while calculation would suggest that the characteristic peak should occur around the same wavelength as that of *Ru*-dnbpy. This would suggest that either the excitation around 550 nm is between different molecular orbitals for each of the different catalysts, that less $[Ru^{IV}=O]^{2+}$ is present, or that compound with these ligands is just unstable. Examination of the molecular orbitals involved in the excitation (see Figure A2.7) shows a similar d – d transition localised on the metal centre for each catalyst (with the unoccupied orbital featuring some delocalisation onto the aromatic ligand). It could therefore be concluded that for the case of *Ru*-bpm and *Ru*-dnbpy, less $[Ru^{IV}=O]^{2+}$ is present after 24 hours.

Table 2.2. Primary excitations for the $[Ru^{IV}=O]^{2+}$ intermediates of the examined catalysts calculated using TDDFT, as compared to experiment

		***Ru*-bpc**	***Ru*-bpy**	***Ru*-mbpy**	***Ru*-dnbpy**
Wavelength (nm)	Exp	550	529	534	~ 560
	Calc	530	501	565	519
Energy (eV)	Exp	2.25	2.34	2.32	~ 2.2
	Calc	2.34	2.47	2.19	2.39

Table 2.3. Change in bond energy for the first two catalytic steps for the examined catalysts. The catalytic steps are assumed to work in PCET regime, and thus the energy of the proton and electron is incorporated by using half the bond energy of H_2

ΔE (eV)	***Ru*-bpc**	***Ru*-bpy**	***Ru*-mbpy**	***Ru*-dnbpy**	***Ru*-bpm**
$\Delta E\ ([Ru^{III}\text{-}OH]^{2+} + \frac{1}{2}H_2 - [Ru^{II}\text{-}OH_2]^{2+})$	1.60	1.68	1.57	1.71	1.68
$\Delta E\ ([Ru^{IV}=O]^{2+} + \frac{1}{2}H_2 - [Ru^{III}\text{-}OH]^{2+})$	1.73	1.63	1.71	1.71	1.73

One might be tempted to attribute this limited presence of $[Ru^{IV}=O]^{2+}$ for *Ru*-bpm and *Ru*-dnbpy to the influence of the different ligand on the oxidation potential of the catalyst, such that the redox potential of CAN would no longer be sufficient to drive the catalyst to this catalytic intermediate. We have therefore computed the energy difference between the first two catalytic steps for all the catalysts examined (see Table 2.3). These results show that from a thermodynamic point of view there is very little difference among the catalysts, and this cannot explain why *Ru*-bpm and *Ru*-dnbpy show little or no presence of the $[Ru^{IV}=O]^{2+}$ intermediate. Most likely these two derivative catalysts are less stable, and have degraded after 24 hours in the presence of CAN. The lower stability of *Ru*-bpm and *Ru*-dnbpy, and their higher oxidation states in particular, may be explained by referring to literature. Ligands such as 2,2'-bipyrimidine are weaker σ-donors and more effective π-acceptors than 2,2'-bipyridine; they are therefore less able to stabilise upper oxidation states, favouring decomposition through ligand loss.[79]

Pulse radiolysis characterization of $[Ru^{III}\text{-}OH]^{2+}$

Although optical absorption measurements clearly showed the $[Ru^{II}\text{-}OH_2]^{2+}$ and $[Ru^{IV}=O]^{2+}$ intermediates, $[Ru^{III}\text{-}OH]^{2+}$, the first PCET intermediate, was not observed. To overcome this problem, pulse radiolysis measurements were made. This technique has two key advantages for tackling these types of problems: it gives access to a wide range of oxidants that can drive the catalyst through its full cycle; and the oxidant can be generated on a time scale of nanoseconds, greatly improving the time resolution.[41] It is therefore a powerful tool for investigating oxidation states that are difficult to access. Here, the derivative catalyst *Ru*-mbpy was used as it reacts with both $SO_4^{\bullet-}$ radicals (produced at neutral and acidic pH) and $CO_3^{\bullet-}$ radicals (produced a basic pH). Experiments were performed in acidic, neutral and basic conditions. However, in neutral and basic conditions, the spectra of the transient oxidised species were not observed, most likely as their lifetime at pH > 3 is below the instrumental resolution (< 10 ns). But the oxidizing $CO_3^{\bullet-}$ (Figure A2.9) or $SO_4^{\bullet-}$ radical did disappear, thereby showing their reactivity with the complex.

The transient spectra of the first PCET intermediate observed at acidic pH are shown in Figure 2.7 (similar spectra obtained with a dose per pulse = 80 Gy are shown in Figure A2.10). A strong band between 300 and 400 nm can clearly be seen. This band is ascribed to ligand-centred π-π* transitions. Two less intense peaks are observed: at 480 and, much weaker, at 600 nm. The latter can be assigned to LMCT transitions, from π (bipyridyl) to partially filled dπ (e_g) orbitals of the Ru^{III} centre, as confirmed by DFT calculations (see Figure A2.11).[74] On the other hand, the absorption bands in the range between 300 and 550 nm can be attributed to MLCT transitions (from dπ (t_{2g}) orbitals of the Ru^{III} to π (bpy) orbitals), in agreement with the literature.[74,80,81]

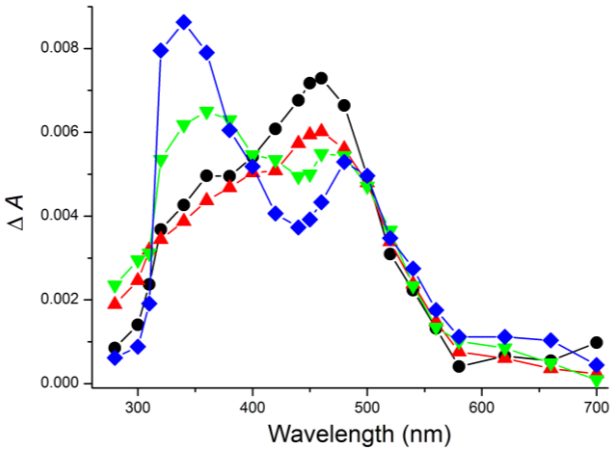

Figure 2.7 Transient absorption spectra obtained by SO4•- radical oxidation of Ru-mbpy (c = 10^{-5} M) after pulse radiolysis of Argon purged solution containing 10 mM $K_2S_2O_8$ and 0.1 M t-BuOH at pH = 1.4. The different curves represent the absorption spectra detected at 1.5 μs (black), 3 μs (red), 5 μs (green), and 15-40 μs (blue) after the pulse. Optical path = 2 cm, dose per pulse = 37.7 Gy.

By increasing $K_2S_2O_8$ concentration up to 0.15 M and decreasing *Ru*-mbpy concentration to 7 μM at pH = 1.4, it was possible to follow the decay of $SO_4^{\bullet-}$ as a function of [*Ru*-mbpy]. Under these conditions all the hydrated electrons are captured by $S_2O_8^{2-}$. The spectra, reported in Figure A2.12, show only the typical band of $SO_4^{\bullet-}$. From this experiment it was possible to obtain the value of $k(SO_4^{\bullet-} + Ru\text{-mbpy}) = (3.6 \pm 0.3) \times 10^9\ M^{-1}\ s^{-1}$.

TDDFT calculations of $[Ru^{III}\text{-}OH]^{2+}$

The spectra for the $[Ru^{III}\text{-}OH]^{2+}$ intermediates were calculated for each catalyst as shown in Figure 2.8 . All catalysts show a primary excitation around 420 nm, while a less intense peak is observed between 550 – 625 nm. This secondary peak is due to a LMCT transition (see Figure A2.11). The differing excitation wavelengths are expected because the ligands differ, and thus also the energy of

Table 2.4 The two primary excitations for the $[Ru^{III}\text{-}OH]^{2+}$ intermediate calculated using TDDFT (Calc), as compared to the two peaks observed in pulse radiolysis measurements of *Ru*-mbpy (Exp). Values are reported both in nm and in eV. In the last column we report the difference in the position of the two peaks.

		λ_1	λ_2	λ_2-λ_1
Wavelength (nm)	Exp	480	~ 620	140
	Calc	424	573	149
		E_1	**E_2**	**E_1-E_2**
Energy (eV)	Exp	2.6	2.0	0.6
	Calc	2.92	2.16	0.76

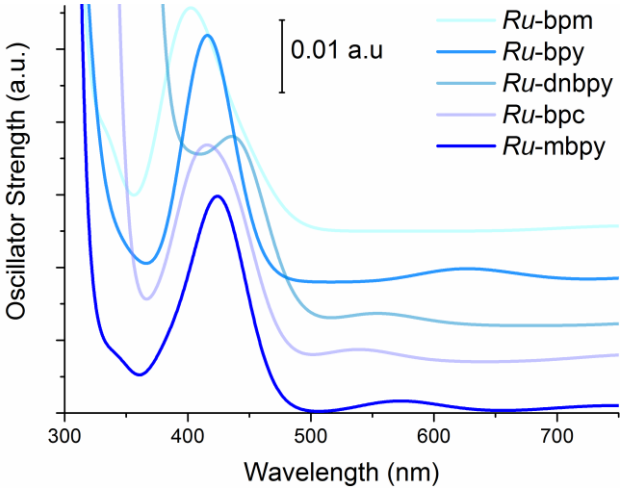

Figure 2.8 TDDFT spectra of the $[Ru^{III}\text{-}OH]^{2+}$ intermediate for each of the catalysts examined in this work. The curves have a Gaussian width broadening of 0.3 eV and have, for clarity, been offset in the Y direction.

the orbital localised on the ligand. In the case of *Ru*-bpm this excitation occurs at sufficiently high energies such that it appears as a slight shoulder of the primary excitation (see also Table A2.4). We can conclude that the difference in the wavelength between these two peaks is characteristic for each catalyst. By comparing the calculated TDDFT spectrum of *Ru*-mbpy to the pulse radiolysis spectra (Table 2.4), it can be seen that the difference in the position of the two peaks agrees reasonably well, even though the absolute position of the peaks is significantly shifted to lower energy in the computed spectrum. This is likely due to the environmental effects within the pulse radiolysis experiments, which are not included theoretically. This analysis supports the observation of the $[Ru^{III}\text{-}OH]^{2+}$ intermediate.

Recently there have been a number of, initially monomeric, iridium based water oxidation catalysts which have been shown to form a dimeric active species. [28,64] An initial exploration was performed as to the possibility of dimer formation using a number of possible dimers (the computationally stable ones are shown in the appendix). However, preliminary calculations do not provide clear evidence of dimer formation.

2.4. Conclusions

A group of mononuclear ruthenium water oxidation catalysts has been analysed with the main goal of characterizing their catalytic mechanism. Catalyst stability is established using OLEMS and SERS. Electrochemical data combined with free-energy calculations using density functional theory clearly point to a catalytic cycle involving four consecutive proton-coupled electron transfer steps. The most

thermodynamic demanding step is the third PCET step starting from the Ru-oxo species and involving the oxygen-oxygen bond formation, which shows an overpotential of about 0.6 V for all the complexes studied. The comparisons between the experimental optical properties and the absorption spectra computed with time-dependent DFT, as well as between SERS and Raman frequency calculations, provide a convincing validation of the proposed catalytic cycle and a clear characterization of the intermediate complexes observed spectroscopically. This combination of experimental data with DFT based modelling is indeed an ideal strategy, one which can be generally applied in the characterisation of water oxidation catalysts.

2.5. References

[1] D. G. H. Hetterscheid and J. N. H. Reek. *Angew. Chem. Int. Ed.* **2012**, *51*, 9740–9747.
[2] H. Dau *et al. ChemCatChem* **2010**, *2*, 724–761.
[3] M. Natali *et al. Chem. Commun.* **2012**, *48*, 8808–8810.
[4] D. J. Stewart *et al. Proc. Natl. Acad. Sci.* **2013**, *110*, 876–880.
[5] J. D. Blakemore *et al. J. Am. Chem. Soc.* **2010**, *132*, 16017–16029.
[6] T. Wang *et al. J. Chem. Theory Comput.* **2010**, *6*, 2395–2401.
[7] K. J. Young *et al. Coord. Chem. Rev.* **2012**, *256*, 2503–2520.
[8] H. Lv *et al. Chem. Soc. Rev.* **2012**, *41*, 7572–7589.
[9] Q. Zeng *et al. Coord. Chem. Rev.* **2015**, *304–305*, 88–101.
[10] N. Kaveevivitchai *et al. Inorg. Chem.* **2012**, *51*, 2930–2939.
[11] L. Duan *et al. Nat. Chem.* **2012**, *4*, 418–423.
[12] L. Duan *et al. Proc. Natl. Acad. Sci.* **2012**, *109*, 15584–15588.
[13] L. Duan *et al. Chem. – Eur. J.* **2010**, *16*, 4659–4668.
[14] J. L. Vallés-Pardo *et al. ChemPhysChem* **2012**, *13*, 140–146.
[15] D. E. Polyansky *et al. J. Am. Chem. Soc.* **2011**, *133*, 14649–14665.
[16] M. D. Kärkäs *et al. Angew. Chem. Int. Ed.* **2012**, *51*, 11589–11593.
[17] L. Tong *et al. Angew. Chem. Int. Ed.* **2011**, *50*, 445–449.
[18] D. C. Marelius *et al. Eur. J. Inorg. Chem.* **2014**, *2014*, 676–689.
[19] D. G. H. Hetterscheid and J. N. H. Reek. *Chem. Commun.* **2011**, *47*, 2712–2714.
[20] K. S. Joya *et al. Angew. Chem. Int. Ed.* **2012**, *51*, 9601–9605.
[21] J. D. Blakemore *et al. Chem. Sci.* **2010**, *2*, 94–98.
[22] A. Savini *et al. Chem. Commun.* **2010**, *46*, 9218–9219.
[23] R. Lalrempuia *et al. Angew. Chem. Int. Ed.* **2010**, *49*, 9765–9768.
[24] M. T. Vagnini *et al. Proc. Natl. Acad. Sci.* **2012**, *109*, 15651–15656.
[25] J. F. Hull *et al. J. Am. Chem. Soc.* **2009**, *131*, 8730–8731.
[26] M. de Respinis *et al. J. Phys. Chem. C* **2015**.
[27] K. S. Joya and H. J. M. de Groot. *Int. J. Hydrog. Energy* **2012**, *37*, 8787–8799.
[28] O. Diaz-Morales *et al. J. Am. Chem. Soc.* **2014**, *136*, 10432–10439.
[29] K. S. Joya. "Molecular catalytic system for efficient water splitting." Dissertatie, Universiteit Leiden: Leiden, 2011.
[30] A. H. Wonders *et al. J. Appl. Electrochem.* **2006**, *36*, 1215–1221.
[31] O. Diaz-Morales *et al. Chem. Sci.* **2013**, *4*, 2334–2343.
[32] S. C. S. Lai *et al. J. Phys. Chem. C* **2008**, *112*, 19080–19087.
[33] P. Gao *et al. J. Electroanal. Chem. Interfacial Electrochem.* **1987**, *233*, 211–222.
[34] J. Suntivich *et al. J. Electrochem. Soc.* **2010**, *157*, B1263–B1268.
[35] G. V. Buxton and Q. G. Mulazzani. In *Electron Transfer in Chemistry*; Wiley-VCH Verlag GmbH, 2001; pp 503–557.
[36] A. Hutton *et al. Quad Area Ric Emilia-Romagna* **1974**, *5*, 67.

[37] Q. G. Mulazzani *et al. J. Phys. Chem.* **1986**, *90*, 5347–5352.
[38] G. V. Buxton *et al. J. Phys. Chem. Ref. Data* **1988**, *17*, 513–886.
[39] P. Wardman. *J. Phys. Chem. Ref. Data* **1989**, *18*, 1637–1755.
[40] E. Wadsworth *et al. Anal. Chem.* **1957**, *29*, 1824–1825.
[41] D. E. Polyansky *et al. Eur. J. Inorg. Chem.* **2014**, *2014*, 619–634.
[42] C. F. Guerra *et al. Theor. Chem. Acc.* **1998**, *99*, 391–403.
[43] G. te Velde *et al. J. Comput. Chem.* **2001**, *22*, 931–967.
[44] SCM. *ADF 2012*; Theoretical Chemistry, Vrije Universiteit, Amsterdam, The Netherlands.
[45] S. Grimme *et al. J. Comput. Chem.* **2011**, *32*, 1456–1465.
[46] M. Swart *et al. Mol. Phys.* **2004**, *102*, 2467–2474.
[47] A. R. Groenhof *et al. J. Am. Chem. Soc.* **2007**, *129*, 6204–6209.
[48] M.-S. Liao *et al. J. Phys. Chem. A* **2007**, *111*, 5927–5935.
[49] M. Güell *et al. JBIC J. Biol. Inorg. Chem.* **2009**, *14*, 273–285.
[50] P. J. Stephens *et al. J. Phys. Chem.* **1994**, *98*, 11623–11627.
[51] A. Klamt. *COSMO-RS: From Quantum Chemistry to Fluid PhaseThermodynamics and Drug Design*; Elsevier Science: Amsterdam, 2005.
[52] J. K. Nørskov *et al. J. Phys. Chem. B* **2004**, *108*, 17886–17892.
[53] J. Rossmeisl *et al. Chem. Phys.* **2005**, *319*, 178–184.
[54] J. Rossmeisl *et al. J. Electroanal. Chem.* **2007**, *607*, 83–89.
[55] M. J. Frisch *et al. Gaussian 09, Revision D.01*; Gaussian, Inc.,Wallingford CT, 2009.
[56] W. R. Wadt and P. J. Hay. *J. Chem. Phys.* **1985**, *82*, 284–298.
[57] P. J. Hay and W. R. Wadt. *J. Chem. Phys.* **1985**, *82*, 299–310.
[58] P. J. Hay and W. R. Wadt. *J. Chem. Phys.* **1985**, *82*, 270–283.
[59] M. Chandrasekharam *et al. RSC Adv.* **2013**, *3*, 26035–26046.
[60] S. Rodríguez *et al. Adv. Synth. Catal.* **2014**, *356*, 301–307.
[61] J. Tomasi *et al. Chem. Rev.* **2005**, *105*, 2999–3094.
[62] N. M. O'Boyle *et al. J. Comput. Chem.* **2008**, *29*, 839–845.
[63] A. Savini *et al. Green Chem.* **2011**, *13*, 3360–3374.
[64] U. Hintermair *et al. J. Am. Chem. Soc.* **2013**, *135*, 10837–10851.
[65] H. Yamada and J. K. Hurst. *J. Am. Chem. Soc.* **2000**, *122*, 5303–5311.
[66] J. DePasquale *et al. Inorg. Chem.* **2013**, *52*, 9175–9183.
[67] D. J. Wasylenko *et al. Inorg. Chem.* **2011**, *50*, 3662–3672.
[68] A. R. Parent *et al. Chem. Soc. Rev.* **2013**, *42*, 2247–2252.
[69] D. Moonshiram *et al. Materials* **2013**, *6*, 392–409.
[70] Y. M. Badiei *et al. Inorg. Chem.* **2013**, *52*, 8845–8850.
[71] R. Staehle *et al. Inorg. Chem.* **2014**, *53*, 1307–1319.
[72] D. J. Wasylenko *et al. Inorg. Chem.* **2010**, *49*, 2202–2209.
[73] L. Wang *et al. Chem. Commun.* **2014**, *50*, 12947–12950.
[74] J. J. Concepcion *et al. J. Am. Chem. Soc.* **2010**, *132*, 1545–1557.
[75] K. G. Kottrup and D. G. H. Hetterscheid. *Chem. Commun.* **2016**, *52*, 2643–2646.
[76] J. L. Vallés Pardo. "In silico study of reaction mechanisms and design principles for water oxidation catalysts." Dissertatie, Universiteit Leiden: Leiden, 2012.
[77] I. R. Paeng and K. Nakamoto. *J. Am. Chem. Soc.* **1990**, *112*, 3289–3297.
[78] D. A. Freedman *et al. Inorg. Chem.* **2006**, *45*, 9558–9568.
[79] G. H. Allen *et al. J. Am. Chem. Soc.* **1984**, *106*, 2613–2620.
[80] S. Hohloch *et al. Dalton Trans.* **2014**, *43*, 4437–4450.
[81] M. K. Nazeeruddin *et al. J. Phys. Chem.* **1993**, *97*, 9607–9612.
[82] G. L. Hug. *Natl. Stand. Ref. Data Syst.* **1981**, *69*, 167.
[83] R. W. Matthews *et al. J. Phys. Chem.* **1970**, *74*, 2475–2479.
[84] K. Henbest *et al. J. Photochem. Photobiol. Chem.* **1994**, *80*, 299–305.

Table A2.1 Determination of the most energetically stable multiplicity for each of the catalytic intermediates of Ru-bpc. ΔE is the energy relative to the lowest energy multiplicity for that intermediate (indicated by asterisks). ΔS^2 is here defined as the difference between the exact and expected value for S^2, which can be considered an indication of the level of spin contamination for that multiplicity.[1]

		B3LYP			OPBE		
		ΔE (eV)	ΔE (kcal/mol)	ΔS^2	ΔE (eV)	ΔE (kcal/mol)	ΔS^2
$[Ru^{II}\text{-}OH_2]^{2+}$	*singlet*	0.00	0.00	0.00	0.00	0.00	0.00
	triplet	1.29	29.85	0.01	1.60	36.79	0.01
	quintet	1.86	42.94	0.01	2.75	63.36	0.02
$[Ru^{III}\text{-}OH]^{2+}$	*doublet*	0.00	0.00	0.01	0.00	0.00	0.00
	quartet	1.36	31.33	0.02	1.62	37.29	0.02
	sextet	2.11	48.59	0.01	4.28	98.64	0.03
$[Ru^{IV}\text{=}O]^{2+}$	singlet	0.27	6.31	0.95	0.25	5.67	0.89
	triplet	0.00	0.00	0.01	0.00	0.00	0.01
	quintet	1.22	28.24	0.02	1.65	38.07	0.01
$[Ru^{III}\text{-}OOH]^{2+}$	*doublet*	0.00	0.00	0.01	0.00	0.00	0.00
	quartet	1.33	30.78	0.02	1.63	37.53	0.02
	sextet	2.06	47.62	0.01	2.86	65.91	0.01
$[Ru^{II}\text{-}OO]^{2+}$	singlet	0.22	5.13	0.00	0.06	1.49	0.00
	triplet	0.00	0.00	0.01	0.00	0.00	0.01
	quintet	0.96	22.10	0.02	1.16	26.70	0.02
	septet	1.95	45.06	0.02	2.60	59.95	0.02

2.A.2. Validation of the TDDFT methodology

The computational set-up employed for the TDDFT calculations in this work (B3LYP/TZP/COSMO) is tested using a benchmark ruthenium-based WOC, for which experimental data is available for comparison.[15] Further calculations were also performed with the larger QZ4P basis set for Ru and TZ2P for H,C,N,O. The calculated results (Figure A2.1) show a close agreement with the published experimental data,[15] though the intensities of the peaks around 525 nm and 625 nm are interchanged. Furthermore, using the larger basis sets does not significantly affect the key features. A summary of the key features is given in Table A2.2. The computed spectra validate the ability of this method to accurately reproduce the optical properties of compounds chemically similar to the WOC of interest for this study.

Table A2.2 Primary excitations for the intermediates of the benchmark catalyst calculated using TDDFT, as compared to experiment performed by Polyanski et al.[15]

		Wavelength (nm)		Energy (eV)	
		Exp	Calc	Exp	Calc
$[Ru^{II}\text{-}OH_2]^{2+}$	λ_{max}	605	630	2.05	1.97
	$\lambda_{shoulder}$	520	515	2.38	2.41
$[Ru^{III}\text{–}OH]^{2+}$	λ_{max}	360	355	3.44	3.49
	$\lambda_{shoulder}$	450	430	2.76	2.88
$[Ru^{IV}\text{=}O]^{2+}$	λ_{max}	370	380	3.35	3.26
	λ_{onset}	500	500	2.48	2.48

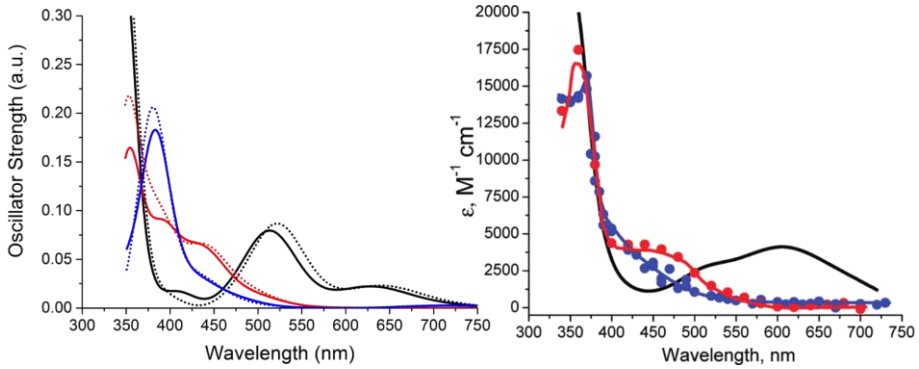

Figure A2.1 Calculated TDDFT spectra (left) of the Ru-based WOC investigated by Polyanski et al.,[15] with $[Ru^{II}\text{-}OH_2]^{2+}$ in black, $[Ru^{III}\text{-}OH]^{2+}$ in red and $[Ru^{IV}\text{=}O]^{2+}$ in blue. The dotted lines indicate the calculations done with the larger basis set. These calculated curves have a Gaussian broadening of 0.3 eV. The experimental data is reproduced at right from Polyansky, D. E.; Muckerman, J. T.; et al. J. Am. Chem. Soc. 2011, 133 (37), 14649.

2.A.3. Raman frequency calculations

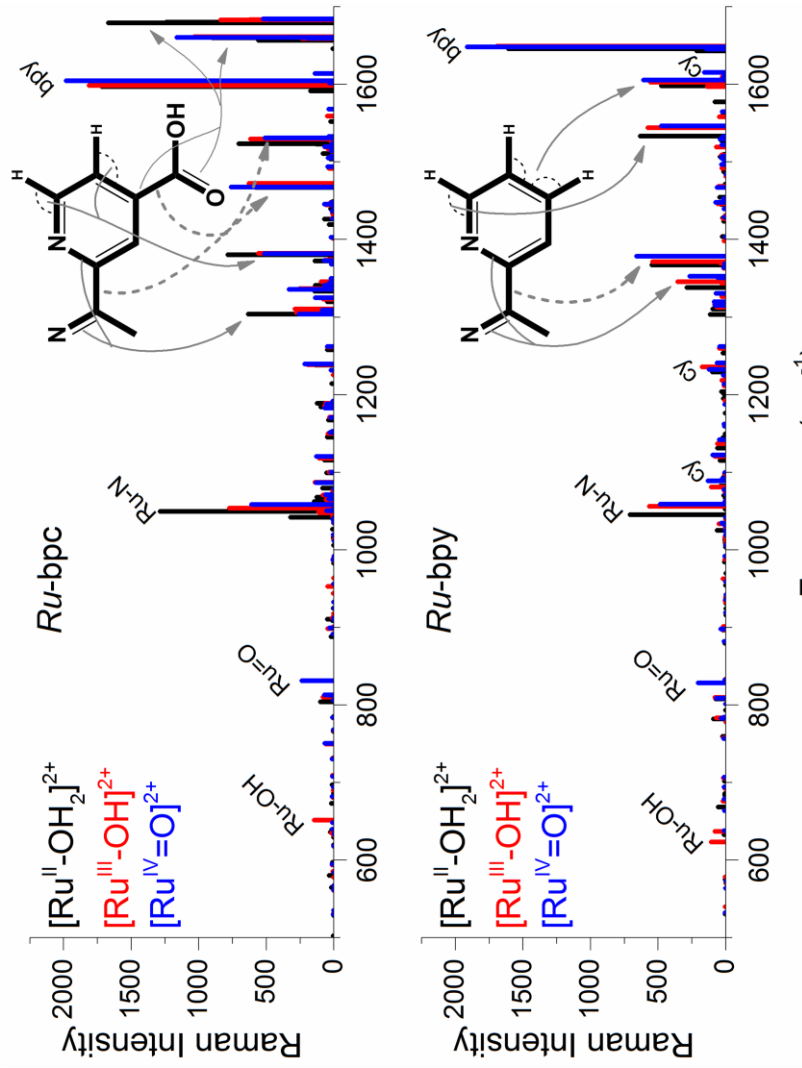

Figure A2.2 Raman frequency calculations of $[Ru^{II}\text{-}OH_2]^{2+}$, $[Ru^{III}\text{-}OH]^{2+}$ and $[Ru^{IV}{=}O]^{2+}$ as calculated for *Ru*-bpc and *Ru*-bpy. Annotations show the nature of each mode.

2.A.4. Time-dependent UV-Vis absorption of Ce^{IV}

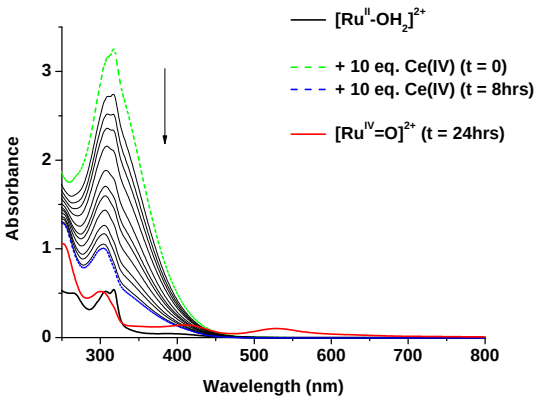

Figure A2.3 Spectral evolution of *Ru*-bpy upon addition of 10 equivalents of CAN in H_2SO_4 1N. Black curve is the spectrum of the Ru complex (c = $5x10^{-5}$ M) before mixing; red curve is the spectrum of the oxidised species, $[Ru^{IV}=O]^{2+}$, obtained after 24 hours upon addition of CAN.

2.A.5. Calculated absorption spectra entire cycle *Ru*-bpy

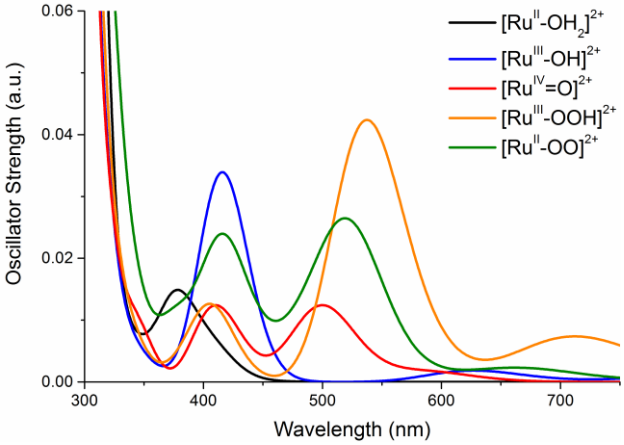

Figure A2.4 TDDFT computed spectra of the entire catalytic cycle of *Ru*-bpy.

These calculations may be used to verify the existence of *Ru*-bpy catalytic intermediates when compared to experimental absorption spectra. The characteristic peak at 500 nm in the $[Ru^{IV}=O]^{2+}$ spectrum is due to one excitation (shown in Figure A2.5), whereas most of the other peaks originate from a mixture of different orbital transitions. It is of note that the catalytic intermediates share a peak around 410 nm (with $[Ru^{III}\text{-}OH]^{2+}$ and $[Ru^{III}\text{-}OOH]^{2+}$, and $[Ru^{IV}=O]^{2+}$ and $[Ru^{IV}\text{-}OO]^{2+}$ being relatively similar) while the only peak in the $[Ru^{II}\text{-}OH_2]^{2+}$ spectrum is slightly higher in energy. That the peak in the $[Ru^{II}\text{-}OH_2]^{2+}$ spectrum is higher in energy is likely due to the doubly occupied nature of all the occupied valence d orbitals of ruthenium. Comparatively, the other catalytic intermediates

have singly occupied d orbitals, which leads to the corresponding unoccupied d orbitals forming low lying unoccupied states

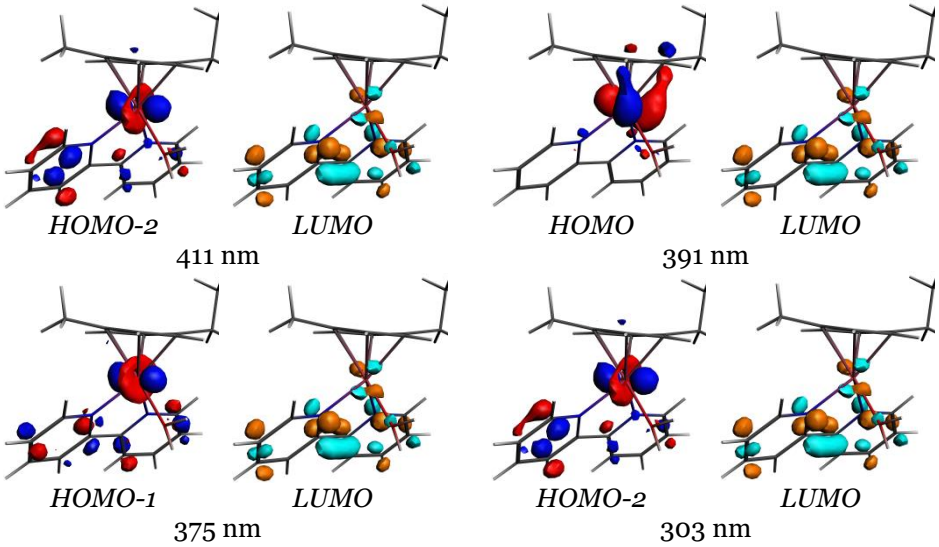

Figure A2.5 Molecular orbitals involved in the excitations calculated for the $[Ru^{II}\text{-}OH_2]^{2+}$ catalytic intermediate of *Ru*-bpy.

2.A.6. Calculated spin density localisation proposed intermediates

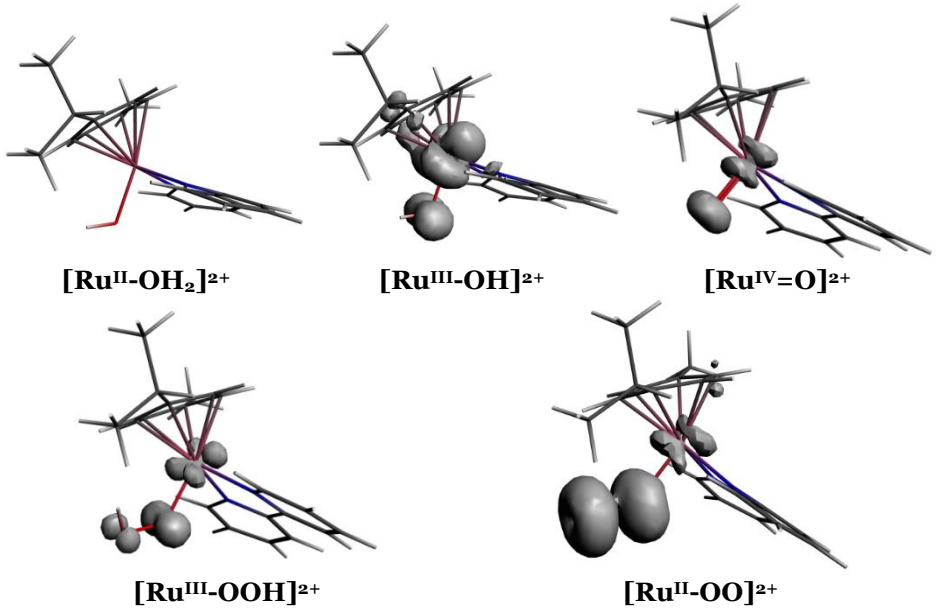

Figure A2.6 Localisation of electron spin density, calculated for the catalytic intermediates of *Ru*-bpy

2.A.7. Orbital comparison of $[Ru^{IV}=O]^{2+}$ intermediates

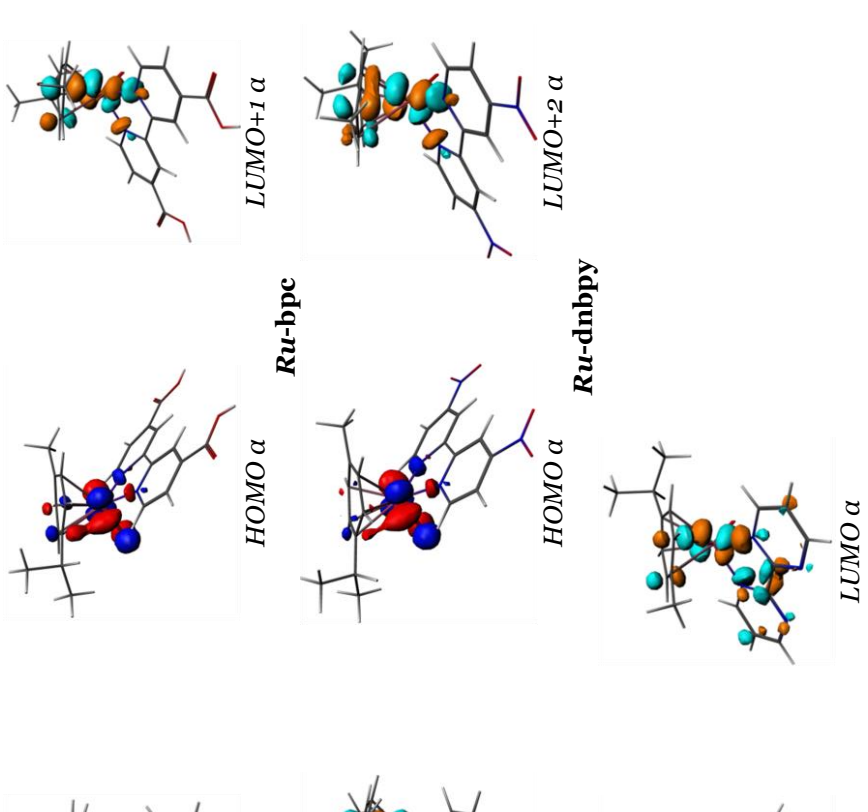

Figure A2.7 Molecular orbitals involved in the signature excitation around 500 nm for the $[Ru^{IV}=O]^{2+}$ catalytic intermediate of the different derivative catalysts.

2.A.8. UV-Vis absorption data for $[Ru^{II}\text{-}OH_2]^{2+}$ complexes

Table A2.3 Absorption properties of the catalysts in their aqua-form in H_2SO_4 1N solution.

	λ nm, ε M^{-1} cm^{-1}
***Ru*-bpy**	246 (10800), 307 (10400), 317 (10800), 400 (800)
***Ru*-bpc**	286 (13400), 323 (12100), 335 (13000), 400 (2100)
***Ru*-bpm**	250 (15500), 400 (1400)
***Ru*-bpn**	319 (12200), 400 (3400)
***Ru*-phen**	278 (23400), 302 sh (8400), 400 (800)
***Ru*-mbpy**	263 (12300), 304 (10900), 314 (11100), 400 (900)

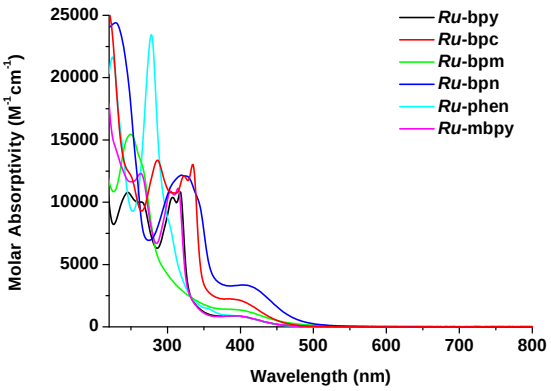

Figure A2.8 Absorption spectra of the catalysts in their aqua-form in H_2SO_4 1N solution

2.A.9. Elucidation $[Ru^{III}\text{-}OH]^{2+}$

Pulse radiolysis in basic solution

The reactivity of *Ru*-bpy with $CO_3^{\bullet-}$ was determined by following the decay of the carbonate radical absorption at 600 nm in the presence of increasing concentrations of the substrate. The natural decay of $CO_3^{\bullet-}$ follows second order kinetics in the absence of any reducing moieties. When the radical reacts with a target, the pulse radiolysis kinetics become first order reactions whose observed rate constants increase with increasing concentration of the reducing moiety.

By using Na_2CO_3/ $NaHCO_3$ (5 mM : 5 mM) (pH = 10) the pH of the solution is too high to observe the absorption of the oxidised forms of *Ru*-bpy, because they decompose too fast to be observed, i.e. below the time resolution of our apparatus (rise-time ~ 2.5 ns). The spectra in Figure A2.9 can be attributed to the $CO_3^{\bullet-}$ decay, with some evidence for *Ru*-bpy transient formation in the region 250-350 nm. From these experiments it was possible to determine the rate constant for the reaction of *Ru*-bpy with $CO_3^{\bullet-}$ by following the first order decay at

600 nm: the value obtained is k ($CO_3^{\bullet-}$ + *Ru*-bpy) = (3.0±0.3)×10^7 M^{-1} s^{-1}.

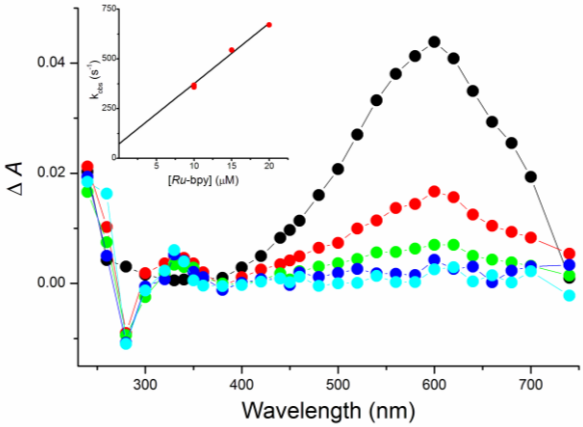

Figure A2.9 Transient absorption spectra obtained by $CO_3^{\bullet-}$ radical oxidation of Ru-bpy (c = 10 μM) after pulse radiolysis of N_2O-saturated solution containing Na_2CO_3/$NaHCO_3$ (5 mM: 5 mM) at pH 10: (black) 200 μs, (red) 2 ms, (green) 6 ms, (blue) 10 ms and (cyan) 17 ms after the pulse. Optical path = 2 cm, dose per pulse = 22.2 Gy. Inset: Plot of k_{obs} vs [*Ru*-bpy] molar concentration (red dots) for the decay of the main signal at 600 nm after pulse radiolysis of Ru-bpy in N_2O-saturated solution containing Na_2CO_3/$NaHCO_3$ (5 mM: 5 mM) at pH 10. Optical path = 2 cm, dose per pulse 44.4 Gy; solid line represents the linear regression fit to the data.

Pulse radiolysis in acidic solution

When $SO_4^{\bullet-}$ is produced in acidic solution, in the absence of any reducing species, the transient spectra show the same behaviour observed at neutral pH with a lower extinction coefficient, ε. The resulting ε is three times smaller than that reported in the literature at pH = 5.1 (ε = 361 M^{-1} cm^{-1} compared to ε_{lit} = 1100 M^{-1} cm^{-1}).[82] Ar-saturated aqueous solutions containing 10 μM *Ru*-mbpy, 10 mM $K_2S_2O_8$ and 0.1 M *t*-BuOH were pulse-irradiated at pH = 1.4 at two different doses, 38 and 82 Gy. From the $SO_4^{\bullet-}$ extinction coefficient ε obtained at acidic pH, we can assume that ~33% of e_{aq}^- generates $SO_4^{\bullet-}$ (Eqn. (2.1)) with a concentration of 3.4 μM when the dose was 38 Gy (see Figure 2.7) and 7.3 μM when the dose was 80 Gy (see Figure A2.10). The remaining hydrated electron reacts with H_3O^+ (Eqn. (2.2), k_4 = 2.3×10^{10} M^{-1} s^{-1})[38] giving the H$^\bullet$ transient species.

$$e_{aq}^- + S_2O_8^{2-} \rightarrow SO_4^{\bullet-} + SO_4^{2-} \qquad (2.1)$$

$$e_{aq}^- + H_3O^+ \rightarrow H^\bullet + H_2O \qquad (2.2)$$

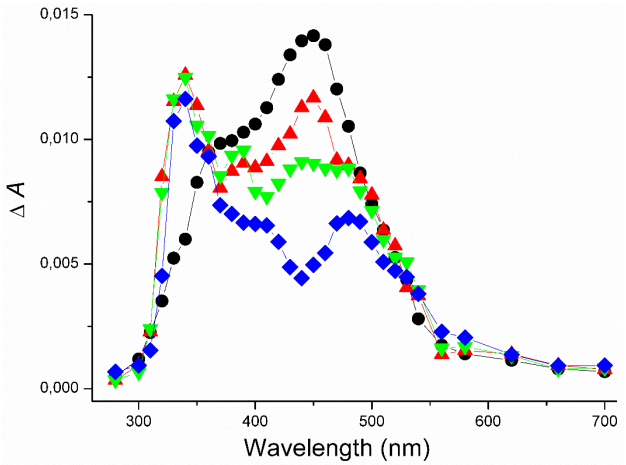

Figure A2.10 Transient absorption spectra obtained by $SO_4^{\bullet-}$ radical oxidation of Ru-mbpy (c = 10^{-5} M) after pulse radiolysis of Argon purged solution containing 10 mM $K_2S_2O_8$ and 0.1 M t-BuOH at pH 1.3: (black) 1.5 µs, (red) 3 µs, (green) 5 µs, and (blue) 15-40 µs after the pulse. Optical path = 2 cm, dose per pulse = 80 Gy.

$H^{\bullet}$ can react with $S_2O_8^{2-}$ to produce the $HSO_4^{\bullet}$ radical,[83] a species whose standard redox potential is not reported in literature, but is able to oxidize moieties similar to *Ru*-mbpy. A photochemical study on the reaction between $SO_4^{\bullet-}$ and $[Ru(bpy)_3]^{2+}$ at acidic pH showed that oxidation occurs, though with a lower rate constant with respect to that already reported by Yamada and Hurst.[84] The contribution of $HSO_4^{\bullet}$ to the oxidation of *Ru*-mbpy must be considered since the yield of oxidant species, i.e. 33%, is higher than expected from the only $SO_4^{\bullet-}$ reaction. It was not experimentally possible to achieve a higher concentration of oxidizer or to apply a higher dose to achieve 100% conversion of e_{aq}^- to $SO_4^{\bullet-}$.

TDDFT analysis: A characteristic peak for $[Ru^{III}\text{-}OH]^{2+}$

The difference between the primary excitation in the calculated spectra for the $[Ru^{III}\text{-}OH]^{2+}$ intermediates and a less intense peak due to a LMCT excitation (Figure A2.11) may be considered characteristic for each catalyst. Though the primary excitation occurs at relatively similar wavelengths for each catalyst (Table A2.4), this secondary peak occurs at varying wavelengths. In comparing the pulse radiolysis experiment done for *Ru*-bpy (Figure A2.9) to that of *Ru*-mbpy (Figure 2.6), it is noted that there is a similar peak at around 350 nm. This peak is likely the primary excitation for the $[Ru^{III}\text{-}OH]^{2+}$ intermediate. In considering the difference in wavelength between this primary excitation and the secondary excitation for *Ru*-bpy, the secondary peak should be observed around 560 nm. However, as seen in Figure A2.9, this is largely swamped by the signal due to $CO_3^{\bullet-}$.

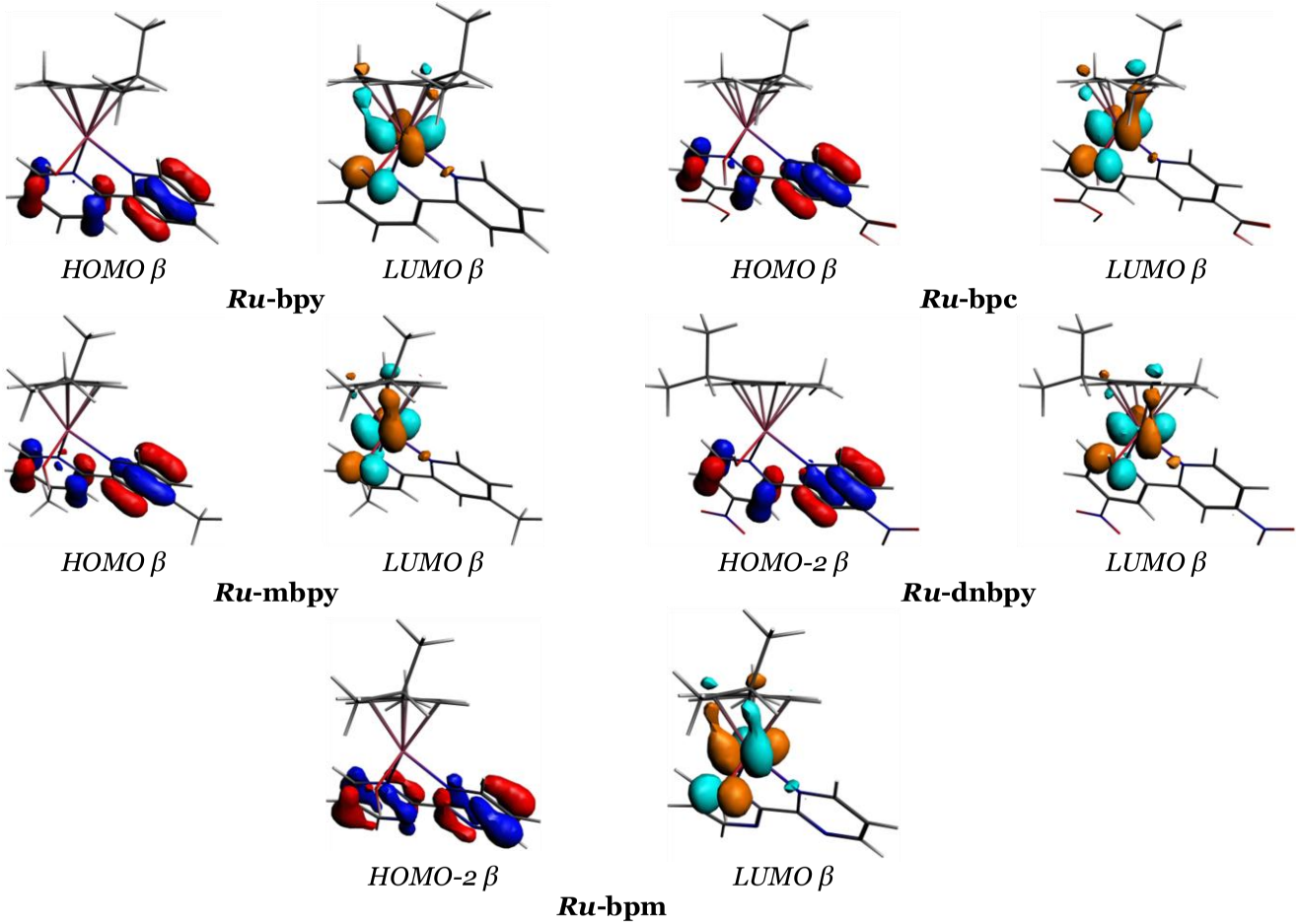

Figure A2.11 Molecular orbitals involved in the signature excitation around 550 – 625 nm for the $[Ru^{III}\text{-}OH]^{2+}$ catalytic intermediate of the different derivative catalysts.

Table A2.4 Primary excitations for the $[Ru^{III}\text{-}OH]^{2+}$ intermediates of the examined catalysts calculated using TDDFT

	***Ru*-bpy**	***Ru*-bpc**	***Ru*-mbpy**	***Ru*-dnbpy**	***Ru*-bpm**
λ_1 (nm)	416	414	424	438	402
E_1 (eV)	2.98	2.99	2.92	2.83	3.08
λ_2 (nm)	627	539	573	554	451
E_2 (eV)	1.98	2.30	2.16	2.24	2.75
$\Delta\lambda$ (nm)	211	125	149	116	49
ΔE (eV)	1.00	0.69	0.76	0.59	0.33

Pulse radiolysis in acidic solution: rate constant determination

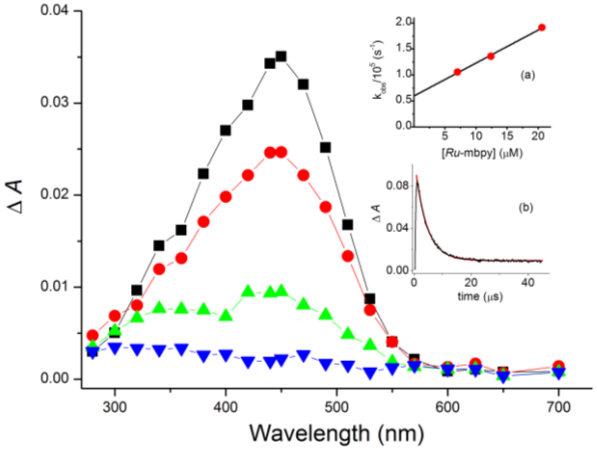

Figure A2.12 Transient absorption spectra after pulse radiolysis of *Ru*-mbpy (c = 7 μM) Ar purged solution containing 0.15 M $K_2S_2O_8$ and 0.1 M t-BuOH at pH 1.4: (black) 1.25 μs, (red) 5 μs, (green) 15 μs, and (blue) 40 μs after the pulse. Optical path = 2 cm, dose per pulse = 38 Gy. Inset (a): Plot of k_{obs} vs [*Ru*-mbpy] for the decay at 450 nm after pulse radiolysis of *Ru*-mbpy Ar purged solution containing 0.15 M $K_2S_2O_8$ and 0.1 M t-BuOH at pH 1.4. Solid line represents the linear regression fit to the data. Inset (b): Graphical representation of absorbance variation vs. time.

Transient absorption spectra are characterised by the decrease of the typical band of $SO_4^{\bullet-}$ at 450 nm and the increase of two new bands at 340 and 480 nm. The isosbestic point at 400 nm indicates that the species absorbing at 450 nm is transformed into the one which absorbs at 340 and 480 nm without parallel or consecutive reactions, i.e. the reaction follows a first order kinetic and is quantitative. In the experimental conditions that enable the observation of the $[Ru^{III}\text{-}OH]^{2+}$ spectra, it was impossible to evaluate and analyse the kinetic decay of the 450 nm $SO_4^{\bullet-}$ absorption (see Figure 2.5 and Figure A2.10) because a long-lived transient build-up is superimposed on the decay at 480 nm.

2.A.10. Initial investigation of two proposed dimeric intermediates

Recently there have been a number of, initially monomeric, iridium-based water oxidation catalysts that have been shown to form a dimeric active species.[28,64] An initial exploration was performed as to the possibility of dimer formation by *Ru*-bpy using the dimers shown in Figure A2.13. For each of them, their geometries were optimised, and TDDFT and Raman spectra calculated following the method as described in the text (Computational Method and Details). The lowest energy multiplicity for both the $[Ru\text{-}O\text{-}O\text{-}Ru]^{4+}$ and the $[Ru\text{-}O\text{-}Ru]^{4+}$ dimer was found to be a triplet. The results of the spectroscopic calculations are compared to experiment below.

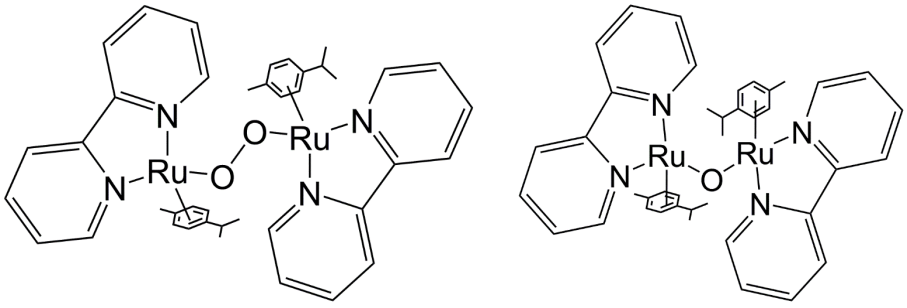

$[Ru\text{-}O\text{-}O\text{-}Ru]^{4+}$ **$[Ru\text{-}O\text{-}Ru]^{4+}$**

Figure A2.13 Dimers investigated

Raman calculations were performed for these dimers following the same methodology described in Computational Method and Details. The conclusions of these calculations are presented below.

Signature Modes Dimers

- **$[Ru\text{-}O\text{-}Ru]^{4+}$**
  - Ru-O-Ru bridge modes calculated at 700 cm^{-1}. This is not observed experimentally as it is swamped by the set-up signal
- **$[Ru\text{-}O\text{-}O\text{-}Ru]^{4+}$**
  - bridge mode calculated at 800 cm^{-1}. This is not observed in the experimental SERS measurement

Comparing the calculated TDDFT spectra of the two dimers to the experimental absorption spectrum after 24 hours, there is little agreement. The spectra calculated for the $[Ru\text{-}O\text{-}Ru]^{4+}$ does show a broad peak around the characteristic wavelength, but does not feature the secondary peak around 400 nm, while the $[Ru\text{-}O\text{-}O\text{-}Ru]^{4+}$ dimer only shows significant excitations at wavelengths higher than 700 nm (Figure A2.14).

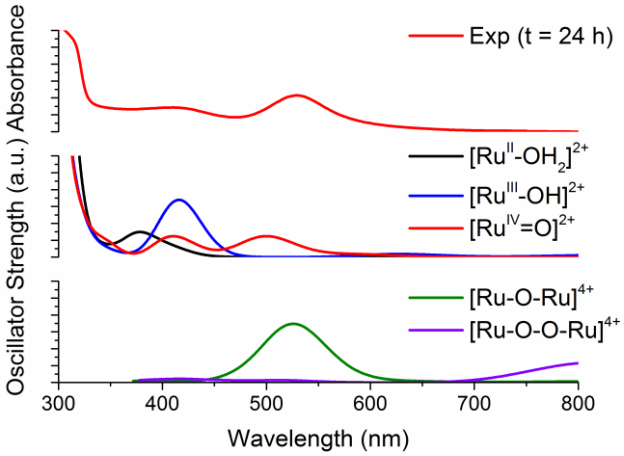

Figure A2.14 TDDFT spectra of $[Ru^{III}\text{-}OH]^{2+}$ and $[Ru^{IV}=O]^{2+}$ of *Ru*-bpy, as well as the two dimers (lower two panels) as compared to experimental absorption spectra after 24 hours upon addition of 10 equivalents of CAN (top panel).

Introducing a Closed System Approach

Chapter Three

3. Introducing a Closed System Approach

Abstract

When examining catalytic steps theoretically, it is often difficult to account for the transfer of protons and electrons from one intermediate to the next. Instead, catalytic intermediates are considered individually, often in an isolated environment. Here a closed system approach is proposed which places the catalytic intermediate in a simulation box filled with explicit solvent; a box which also includes proton and electron acceptors. In this way the system is designed to more closely reflect experimental conditions, and allows for a complete description of proton-coupled electron transfer processes. Using Car-Parrinello Molecular Dynamics, a mononuclear copper water oxidation catalyst $Cu(bpy)(OH)_2$ was used as a model system to explore this closed system approach. This model system shows that, compared to traditional methods, this approach offers extra insight into proposed catalytic steps and allows for clear identification of preferred reaction paths.

This chapter is based on

J. M. de Ruiter, and F. Buda "Introducing a Closed System Approach for the Investigation of Chemical Steps Involving Proton and Electron Transfer; as Illustrated by a Copper-Based Water Oxidation Catalyst."
Physical Chemistry Chemical Physics, **2016**, doi: 10.1039/C6CP07454E

3.1. The call for the Closed System Approach – Mechanistic Considerations

The optimisation of WOCs is a very active field of research,[1–8] especially catalysts based on abundant transition metals such as copper and iron.[9–14] In designing the ideal WOC it is essential to develop a fundamental understanding of the various water oxidation catalytic mechanisms. Traditionally, catalytic cycles are examined computationally by comparing the free energies of the proposed catalytic intermediates and then, usually, assigning the thermodynamically most favourable cycle as the most likely catalytic cycle.[7,8,15–18] This examination often uses an implicit solvent model – the more involved methods which do include explicit solvent molecules are very time-consuming.[19–21] This static analysis of reaction pathways limits the information that can be acquired about the mechanistic bottlenecks between one catalytic intermediate and the next. Furthermore, an increasing number of studies have shown that the solvent molecules surrounding a catalytic site are far from innocent bystanders.[22–25] Dynamic insight into PCET reactions can therefore be very useful in the design of an optimised water oxidation catalyst.

We propose a CSA in which the catalytic step itself can be examined, with the charge carriers being contained within the system to allow for the analysis of the free energy profile from one catalytic intermediate to the next. By constraining the multiplicity of the system the charge of the metal ion Me can be switched between the 2^+ and 3^+ state, as shown in Figure 3.1.

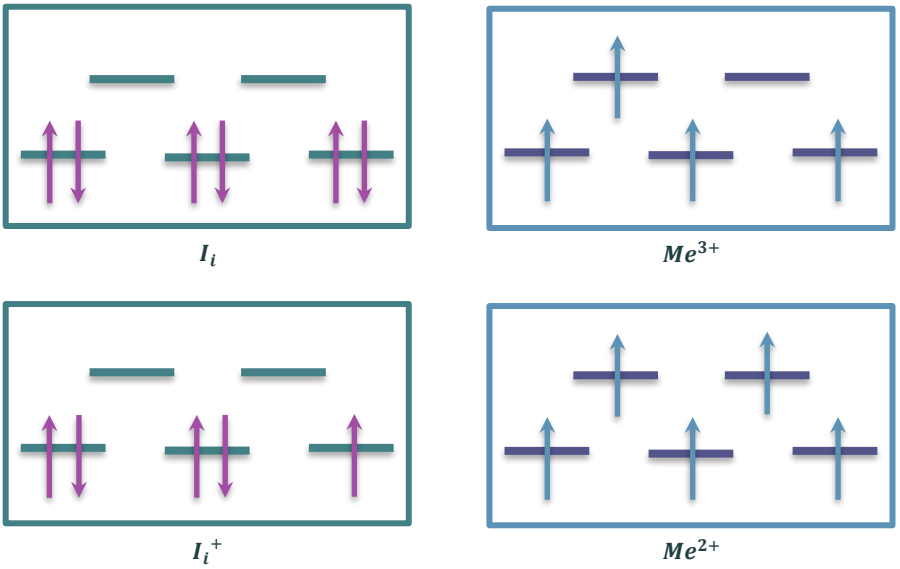

Figure 3.1 Schematic representation of how a change in the total multiplicity of the system leads to the transfer of an electron: I_i + Me^{3+} has quintet multiplicity, while I_i^+ + Me^{2+} has septet multiplicity.

Including explicit water in the simulation box allows for proton transfer from the catalyst to the solvent, while including a metal ion allows for the 'transfer' of an electron within the system. The metal ion behaves like the sacrificial oxidant CAN commonly used in experimental studies of WOC mechanisms. Here transfer is noted in inverted commas as the localisation of the electron *is* constrained by the multiplicity of the whole system: this set-up allows for the analysis of the featured catalyst both before and after a supposed electron transfer within the system. The process of this electron transfer could be examined if the multiplicity of the system both before and after electron transfer were the same. However, that is not something that is considered here. The potential energy profiles of the three systems we can now directly compare,

$$I_i + Me^{3+} \rightleftharpoons I_i^+ + Me^{2+} \rightleftharpoons I_{i+1} + H_{solv}^+ + Me^{2+}, \qquad (3.1)$$

where the solvated proton is denoted H_{solv}^+, are shown in Figure 3.2.

To test the applicability of this CSA we compare two trial catalytic cycles (see Figure 3.3) for the [Cu(bpy)(OH)$_2$] copper based catalyst (denoted [*Cu*(OH)$_2$]).[10] In examining these cycles, we use a pH-independent reference frame. Changes in free energy between the intermediates may shift with respect to changing pH, but relative differences should be constant. The [Cu(bpy)(OH)$_2$] catalyst has been reported to be active at high pH at which it has the [*Cu*(OH)$_2$] form.[10] Although the catalytic cycle of the [*Cu*(OH)$_2$] catalyst has been briefly considered theoretically,[26] a number of open questions remain. After performing a thermodynamic analysis of the two cycles based on DFT calculations, the crucial

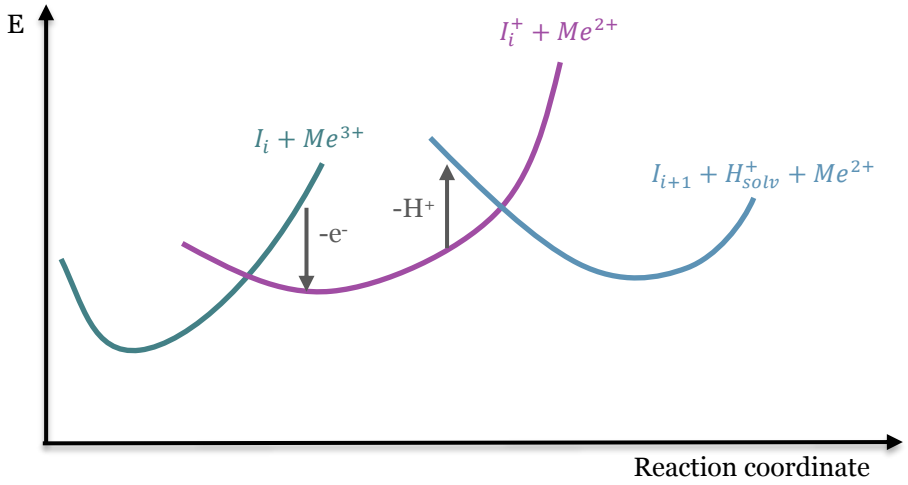

Figure 3.2 Potential energy profiles of a reaction where proton and electron transfer can be examined within CSA. Electron transfer occurs via a change in multiplicity for the total system, while constrained CPMD is used to monitor proton transfer.

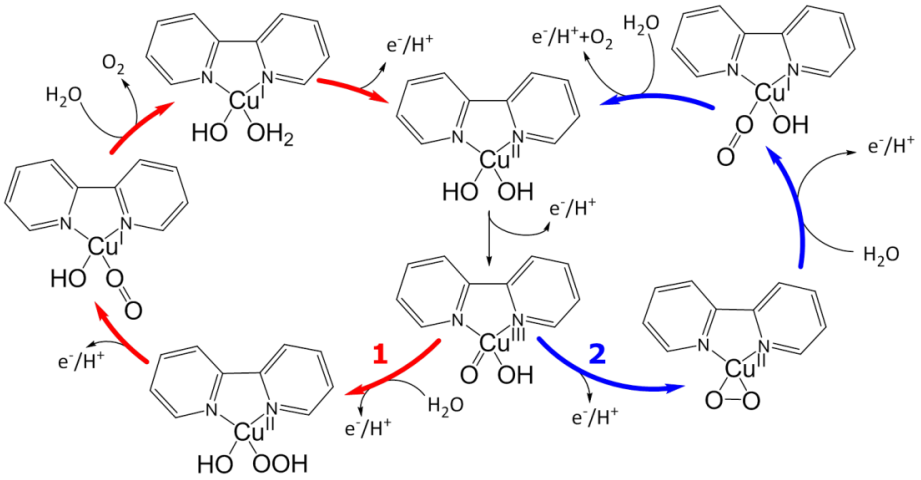

Figure 3.3 Two proposed mechanisms for water oxidation by [Cu(bpy)(OH)$_2$]: Cycle 1 (left) and Cycle 2 (right).

O – O bonding step of Cycle 2 is examined using *ab initio* constrained molecular dynamics in explicit solvent. This explicit solvent examination is furthered by a closed system analysis using constrained molecular dynamics. The CSA is also used to investigate the O – O bonding step of Cycle 1. For this step an examination of the mean constraint force is also performed.

3.2. Computational method and details

Geometry optimisations and thermodynamic calculations are performed for each catalytic intermediate with DFT using the implementation in the ADF software package.[27–29] Van der Waals interactions are accounted for by using the Grimme3 BJDAMP dispersion correction.[30] The geometries of the examined molecules are initially optimised using the OPBE functional,[31] with the TZP basis set and a small frozen core. This GGA functional has shown good performance when describing transition metal complexes.[22,32–35] Benchmark studies of proton transfer energies with GGA functionals show that reaction barriers are underestimated by around 3 to 3.5 kcal mol^{-1} when compared to those calculated with highly correlated *ab initio* methods.[36] However, as we have argued earlier,[23] within CPMD this is likely compensated by the quantum effect error resulting from the classical treatment of proton motion. Comparisons between the optimised geometry of [*Cu*^{II}(OH)$_2$] with the crystal structure of a catalyst with a similar metal centre are included in Table A3.1.[37] These show good agreement, with OPBE/TZP reproducing most metal centre geometric parameters within a few percent. For each of the intermediates the most energetically favourable spin state is determined (see Table A3.2). The geometric information for these intermediates is also shown in the Table A3.3 and Table A3.4.

The CPMD program for AIMD was used to examine the explicitly solvated systems.[38] The solvent environment for the CPMD simulations was generated using Discovery Studio 2.5.[39] The solvent was equilibrated for 0.2 ns using the CHARMM force field and CFF partial charge parameters at 300 K,[40] while the catalyst was kept fixed. The volume was then adjusted using constant pressure for 0.2 ns, after which the system was further allowed to evolve with constant volume for 2 ns. Subsequently CPMD calculations were performed in the canonical NVT ensemble at 300 K, using GTH pseudopotentials for the transition metals,[41] DCACP pseudopotentials for the remaining atoms,[42] and the OPBE exchange-correlation functional.[43] An energy cut-off of 70 Ry was used and a time step of 5 a.u., 1 a.u. = 0.0242 fs. Image rendering for the CPMD output was done using VMD.[44,45]

In this chapter we compare alternative reaction paths using both the traditional static analysis and the CSA, focussing on the differences the two methods predict for the mechanism of the catalytic cycle. To do so we use the methods for calculating changes in free energies as outlined in Chapter 1.

Three different solvated systems were investigated:

System 1

The [Cu^{II}(O)(O)] intermediate within a 17.7 × 17.2 × 8.5 Å^3 box with 73 water molecules, total charge 0, with doublet spin multiplicity (see Table 3.1). This system is used to examine constrained molecular dynamics of the O – O bonding step of Cycle 2 in explicit solvent. A solvent water molecule is constrained at progressively closer distances to the copper centre: d(O→Cu) = 3.82 – 1.95 Å. For each distance the system is allowed to evolve for 242 fs, during which the mean constraint force is seen to stabilise. This constraint analysis is repeated constraining the distance between a solvent water molecule and an oxo ligand: d(O→O) = 2.45 – 1.44 Å. After the constrained dynamics calculation at the shortest distance, the constraint is released and the dynamics allowed to continue for 968 fs.

System 2

The [Cu^{II}(O)(O)] intermediate and an Fe ion are solvated in a 7.6 × 14.9 × 10.3 Å^3 box with 72 water molecules, total charge 3$^+$, with septet ([Cu^{II}(O)(O)] + Fe^{3+}) or quintet ([Cu^{III}(O)(O)]$^+$ + Fe^{2+}) multiplicity. CSA is used to further the explicit solvent examination of the O – O bonding step of Cycle 2. The distance between a solvent water molecule and an oxo ligand d(O→O) is constrained at 2.3 Å and the system allowed to evolve for 1.21 ps.

System 3

In order to investigate the O – O bonding step of Cycle 1 the [Cu^{III}(OH)(O)]

Table 3.1 Summary of the systems considered. The q_{tot} is the total charge of the system, 2S+1is the spin multiplicity, and S_{cat} and S_{Me} represent the spin of the catalyst and metal ion, respectively.

	q_{tot}	2S+1	S_{cat}	S_{Me}
$[Cu^{II}(O)(O)]$	0	2	1/2	-
$[Cu^{II}(O)(O)] + Fe^{3+}$	3	7	1/2	5/2
$[Cu^{III}(O)(O)]^{+} + Fe^{2+}$	3	5	0	2
$[Cu^{III}(OH)(O)] + Mn^{3+}$	3	5	0	2
$[Cu^{II}(OH)(O)]^{+} + Mn^{2+}$	3	7	1/2	5/2

intermediate and an Mn ion are examined within a 17.6 × 14.9 × 10.3 $Å^3$ box with 72 water molecules, a total charge of 3^+. The system was investigated with quintet ($[Cu^{III}(OH)(O)] + Mn^{3+}$) or septet ($[Cu^{II}(OH)(O)]^{+} + Mn^{2+}$) multiplicity. The distance between a solvent water molecule and an oxo ligand is constrained at varying distances (d(O→O) = 2.4 – 1.44 Å) and the system allowed to evolve for 1.2 ps for each distance.

In Systems 2 and 3, those with an extra metal atom, a spin constraint is applied such that the total multiplicity of the system is either quintet or septet. This results in modifying the number of unpaired spins localised on the catalyst and metal atom (see Table 3.1). A posteriori, the localisation of spin density, or lack thereof, on the catalyst was used to confirm the expected transfer of an electron. We also integrated the spin density in two different regions of the simulation box and in this way quantitatively verified that the expected number of unpaired electrons was found on the catalyst and the extra metal atom, respectively. An Fe or Mn ion was used depending on the spin state of the to-be-investigated catalytic intermediate. These elements are selected because of their stability in either 2^+ or 3^+ oxidation states, and their differing multiplicities.

3.3. Results and Discussion

3.3.1. Static Thermodynamics of the Catalytic Cycles

We first examine two trial catalytic cycles (see Figure 3.3) via the static, traditional method: by calculating the free energies of each intermediate in the two cycles. The two cycles are composed of PCET steps and differ primarily in the approach to the oxygen-oxygen bond formation step: Cycle 1 proceeds via nucleophilic attack while Cycle 2 features an intra-molecular O – O coupling step. These two approaches have emerged from within the natural photosynthesis community,[46,47] and have also gained traction within the artificial photosynthetic field.[7,34,48,49] It is therefore apt to compare the two. Geometries of the intermediates were optimised and the most energetically favourable multiplicity for each intermediate determined as shown in Table A3.2 and Table A3.3. The appendix also includes renderings of the spin density of the relevant proposed

Table 3.2 Calculated ΔG for each catalytic step along the two proposed mechanisms for [Cu(bpy)(OH)$_2$] ([Cu^{II}(OH)$_2$])

Cycle 1	ΔG_{calc} (eV)
[Cu^{II}(OH)$_2$] → [Cu^{III}(OH)(O)]	2.28
[Cu^{III}(OH)(O)] → [Cu^{II}(OH)(OOH)]	1.27
[Cu^{II}(OH)(OOH)] → [Cu^{I}(OH)(OO)]	0.75
[Cu^{I}(OH)(OO)] → [Cu^{I}(OH)(OH$_2$)]	1.46
[Cu^{I}(OH)(OH$_2$)] → [Cu^{II}(OH)$_2$]	-0.73
2H$_2$O → 2H$_2$ + O$_2$	5.03

Cycle 2	ΔG_{calc} (eV)
[Cu^{II}(OH)$_2$] → [Cu^{III}(OH)(O)]	2.28
[Cu^{III}(OH)(O)] → [Cu^{II}(O)(O)]	0.86
[Cu^{II}(O)(O)] → [Cu^{I}(OH)(OO)]	1.16
[Cu^{I}(OH)(OO)] → [Cu^{II}(OH)$_2$]	0.73
2H$_2$O → 2H$_2$ + O$_2$	5.03

intermediates (Figure A3.1).

The changes in free energy along the trial catalytic cycles are shown in Table 3.2 and in Figure 3.4. In Table 3.2 we also note the computed ΔG associated to the hydrolysis process; this corresponds to the sum of all the ΔG contributions in the

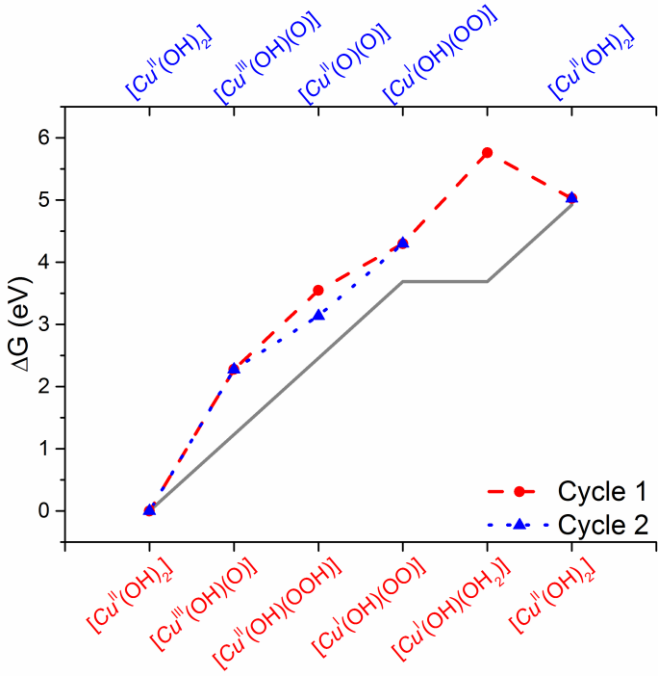

Figure 3.4 Cumulative free energy of the two proposed mechanisms for [Cu(bpy)(OH)$_2$] ([Cu(OH)$_2$]) as calculated by ADF (B3LYP/TZP/COSMO). We also show, as a visual guide, a constant change of 1.23 eV for all four PCET steps (grey line).

complete catalytic cycle. This result deviates only by 0.1 eV with respect to the experimental value of 4.92 eV, which thereby provides an indication that the chosen static computational method is sufficiently accurate in its description of the water oxidation reaction.

The first proposed step $[Cu^{II}(OH)_2] \rightarrow [Cu^{III}(OH)(O)]$, which the two cycles share, has a difference in free energy of 2.28 eV. This is then a calculated overpotential of 1.05 V as compared to the experimentally obtained 0.75 V; cyclic voltammetry shows one large pH-dependent wave.[10] This step is significantly higher than the others (see Table 3.2), making it the thermodynamic bottleneck. Another step with a relatively high calculated change in free energy is the ligand exchange step in which water is exchanged for the formed OO ligand: $[Cu^{I}(OH)(OO)] \rightarrow [Cu^{I}(OH)(OH_2)]$. This differs from the free energy profile for heterogeneous water splitting on metal oxides.[50]

The assumption that the OO/OH_2 ligand exchange is thermodynamically neutral is based on the two ligands both being neutral. However, in this case, the Cu^{I} centre can donate some of its excess charge to the OO ligand, which more readily accepts excess electrons than the OH_2 ligand. This would then make the OO ligand slightly negatively charged, which would electrostatically stabilise this intermediate. This electrostatic attraction is also observed in the shorter Cu – O distance: 2.11 Å in $[Cu^{I}(OH)(OO)]$ and 2.20 Å in $[Cu^{I}(OH)(OH_2)]$. This avenue for charge donation also accounts for the $[Cu^{I}(OH)(OH_2)] \rightarrow [Cu^{II}(OH)_2]$ step being thermodynamically favourable. Considering the high pH at which this catalyst oxidises water,[10] it is likely that the OO ligand exchange with a water molecule is concerted with an immediate PCET step. This is implicit in the $[Cu^{I}(OH)(OO)] \rightarrow [Cu^{II}(OH)_2]$ step of Cycle 2, where $\Delta G = 0.73$ eV. As expected, this is also equal to the sum of ΔG for the two last steps of Cycle 1.

The differences in energies at the point where the two cycles diverge is more explicitly shown in Figure 3.5. Shown in red is the difference in energy for oxygen-oxygen bond formation via nucleophilic attack as per the catalytic cycle on the left in Figure 3.3 (Cycle 1) and in blue that via intra-molecular O – O coupling as per the cycle on the right in Figure 3.3 (Cycle 2). Once the catalyst has reached the $[Cu^{III}(OH)(O)]$ intermediate in the catalytic cycle, we would expect the $[Cu^{II}(O)(O)]$ intermediate in Cycle 2 to be more favourable than the $[Cu^{II}(OH)(OOH)]$ in Cycle 1: $[Cu^{II}(O)(O)]$ is lower in energy by 0.41 eV. The two ligated oxygens in the $[Cu^{II}(O)(O)]$ intermediate strongly interact in the optimised geometry with an O – O distance of 1.47 Å. This distance is comparable to an oxygen-oxygen single bond length in, for example, hydrogen peroxide. This apparently covalent interaction between the oxygen atoms stabilises this intermediate. However, these results were obtained from calculations in implicit water. It is not immediately obvious whether this stabilisation effect will also be

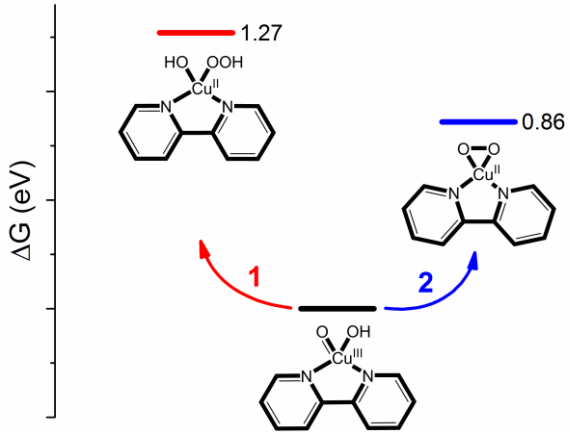

Figure 3.5 Difference in free energy for the two oxygen-oxygen bond formation steps: nucleophilic attack in Cycle 1 (red) and intra-molecular O – O coupling in Cycle 2 (blue) as calculated by ADF (B3LYP/TZP/COSMO).

present within an explicit solvent environment. To examine the impact of including explicit water molecules, as well as how this intra-molecular O – O bond would lead to the next catalytic intermediate in the trial catalytic cycle, we move to an explicitly solvated analysis with CPMD.

3.3.2. Ab-Initio Constrained Molecular Dynamics of System 1

In System 1, which contains the [Cu^{II}(O)(O)] intermediate, two pathways are examined. The first is the constraining of the distance between a solvent water molecule and the copper centre, such that the water molecule approaches axially. It is hypothesised that this may displace one of the oxo ligands which, after a PCET step, would lead to the [Cu^{I}(OH)(OO)] intermediate as shown in Figure 3.3. The constrained pathway is initiated with the incoming water molecule at 3.82 Å and shortened incrementally. Little change is seen besides solvent rearrangement until d(O→Cu) = 1.95 Å. When constrained at 1.95 Å from the copper centre, the incoming water molecule undergoes proton transfer (see Figure 3.6). The proton is transferred to a ligated oxo group via another solvent molecule. This is then effectively a step backwards in the catalytic cycle as we recover the intermediate [Cu^{II}(OH)(O)].

The second pathway examined in System 1 is the approach of a water molecule to one of the oxo ligands (Figure 3.7). The distance between the oxygen atom of the oxo ligand and the oxygen atom of the incoming water molecule is constrained. When constrained at 1.9 Å, a proton is accepted by the oxo ligand not involved in the constraint from a solvent water molecule as shown in Figure 3.7(b). Once again we recover the intermediate [Cu^{II}(OH)(O)].

In the current set-up, the system consistently favours the formation of the

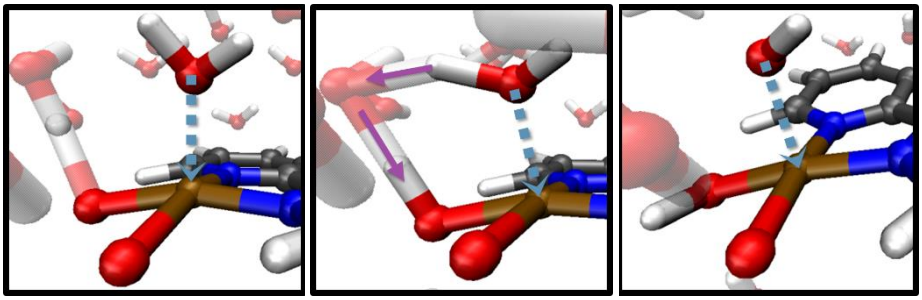

(a) (b) (c)

Figure 3.6. Subsequent snapshots of the MD simulation of System 1: [*Cu*^{II}(O)(O)]. A water molecule is constrained at d(O→Cu) = 1.95 Å (a). This intermediate then undergoes proton exchange via a solvent water molecule (b).The final conformation of the intermediate is shown in (c), where one of the oxo groups has accepted a proton.

transition state [*Cu*^{II}(OH)(O)]. This may be because the oxidation state of the copper must change before advancing to the next catalytic intermediate. In the current MD set-up proton transfer can occur from catalyst to solvent, however there is no electron acceptor which might allow for electron transfer from the catalyst. We therefore move on to the proposed CSA, which includes an additional metal ion capable of acting as an electron acceptor.

3.3.3. Closed System Analysis of the [*Cu*^{II}(O)(O)] intermediate

In the closed system analysis of the [*Cu*^{II}(O)(O)] intermediate, a Fe metal ion is used as an electron acceptor (System 2). We start a constrained molecular dynamic pathway of a solvent water molecule approaching an oxo group, with an initial d(O→O) = 2.3 Å. Two cases are examined: the neutral catalyst [*Cu*^{II}(O)(O)] + Fe^{3+}) and the ionised one ([*Cu*^{III}(O)(O)]$^{+}$ + Fe^{2+}). In this way the total charge in the entire system remains constant. The 'transfer' of an electron is imposed by switching the multiplicity of the entire system from septet to quintet. After

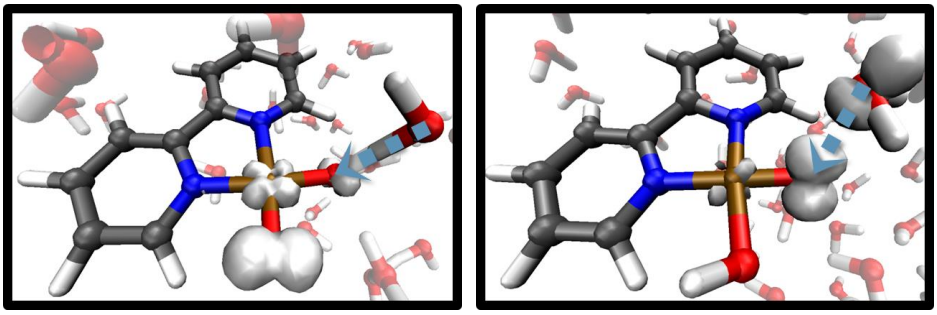

(a) (b)

Figure 3.7. Snapshots of an alternative pathway proposed for System 1: [Cu^{II}(O)(O)]. Localisation of the spin density (grey isosurface) is shown while a water molecule is constrained at increasingly shorter distances to an oxo ligand: d(O→O) = 2.45 Å (a) and d(O→O) = 1.9 Å (b).

allowing the MD simulation to evolve for 1.2 ps, it is seen that in both cases – $[Cu^{II}(O)(O)] + Fe^{3+}$ and $[Cu^{III}(O)(O)]^{+} + Fe^{2+}$ – a proton from a solvent water molecule is accepted by the oxo group (Figure 3.8). This strongly suggests that the $[Cu^{II}(O)(O)]$ intermediate is not stable in a solvated water environment, even if an electron has been removed from the catalyst (as shown in Figure 3.8 $[Cu^{III}(O)(O)]^{+} + Fe^{2+}$). In both System 1 and System 2 solvent water molecules play a crucial role in the shuttling of protons around the catalytic site. Furthermore it appears that the thermodynamic calculations of the $[Cu^{II}(O)(O)]$ intermediate without explicit water molecules led to the artificial stabilisation of an O – O bond. Although thermodynamic analysis suggested that Cycle 2 would be more favourable, in explicit solvent the $[Cu^{II}(O)(O)]$ intermediate decays to the $[Cu^{II}(OH)(O)]$ transition state. Proceeding to the next catalytic intermediate in Cycle 2 via intra-molecular O – O coupling is therefore unlikely. This highlights the need for an explicit solvent when proposing and considering catalytic cycles.

3.3.4. Closed System Analysis of the $[Cu^{III}(OH)(O)]$ intermediate

To further explore the catalytic cycle using the proposed methodology we examine the O – O bond formation step by nucleophilic attack as proposed in Cycle 1. Using System 3, which contains the $[Cu^{III}(OH)(O)]$ intermediate and a Mn ion, a sequence of constrained MD simulations is performed with a quintet multiplicity for the neutral catalyst, or septet for the ionised catalyst. The distance between the oxo ligand and the oxygen of an incoming water, d(O→O), is constrained, and the time-averaged constraint force monitored. In this way we examine the $[Cu^{III}(OH)(O)]$ intermediate as it would hypothetically react to form the $[Cu^{II}(OH)(OOH)]$ intermediate.

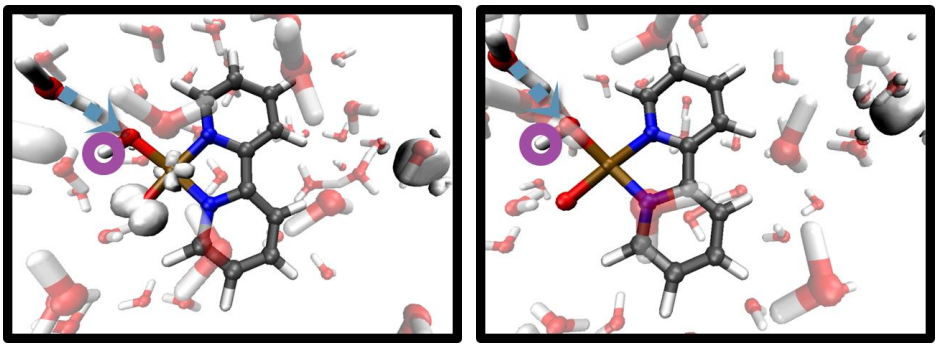

$[Cu^{II}(O)(O)] + Fe^{3+}$ **$[Cu^{III}(O)(O)]^{+} + Fe^{2+}$**

Figure 3.8. Spin density (shown as a grey isosurface) of $[Cu^{II}(O)(O)] + Fe^{3+}$ and $[Cu^{III}(O)(O)]^{+} + Fe^{2+}$, after MD simulation. The constrained water molecule as well as the catalyst are shown in bold. The Fe ion is visible on the right hand side, enveloped by spin density. In the case of $[Cu^{II}(O)(O)] + Fe^{3+}$, spin density is also seen on the copper centre and oxo ligand. In the spin-flipped case $[Cu^{III}(O)(O)]^{+} + Fe^{2+}$, spin density is only seen on the Fe ion as expected. The total charge of the system is 3^{+}. In both cases, a proton (circled) is accepted by an oxo ligand.

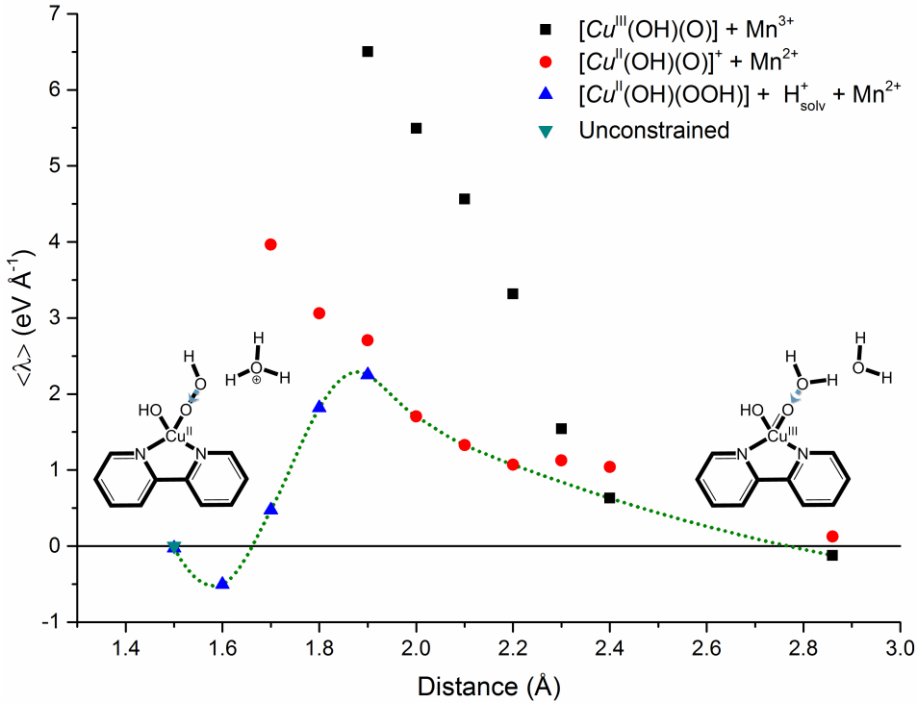

Figure 3.9 The time-averaged constraint force (<λ>) as a function of d(O→O) (blue dotted line in insets). This analysis is performed for [*Cu*^{III}(OH)(O)] + Mn^{3+} and [*Cu*^{II}(OH)(O)]$^{+}$ + Mn^{2+}. The average distance of the unconstrained O - O bond after the proton has been transferred is indicated by a green triangle. The constrained force analysis is also done in reverse: lengthening d(O→O) for [*Cu*^{II}(OH)(OOH)] + H^{+}_{solv} + Mn^{2+}. The green dotted line indicates the lowest energy pathway.

In Figure 3.9 the time-averaged constraint force <λ> of the system containing [*Cu*^{III}(OH)(O)] + Mn^{3+} as d(O→O) is shortened is shown with black squares, while the system containing [*Cu*^{II}(OH)(O)]$^{+}$ + Mn^{2+} is shown with red circles. The average O – O bond length in an unconstrained MD simulation performed after the bond has been formed is also shown in Figure 3.9 as a green triangle. Reversing the process by breaking the recently formed O – O bond i.e. [*Cu*^{II}(OH)(OOH)] → [*Cu*^{II}(OH)(O)]$^{+}$, is shown with blue triangles, while the pathway along the lowest energy intermediates is indicated in Figure 3.9 by a green dotted line.

At d(O→O) = 2.4 – 2.9 Å, <λ> is smaller in the [*Cu*^{III}(OH)(O)] + Mn^{3+} system than when in [*Cu*^{II}(OH)(O)]$^{+}$ + Mn^{2+}. However, between d(O→O) = 2.4 and d(O→O) = 2.1 Å a crossing of the two curves occurs, indicating that at d(O→O) less than ~2.35 Å <λ> is smaller if the electron is found on the Mn ion rather than on the catalyst. That is to say, as soon as an incoming solvent molecule is within 2.35 Å of the oxo group, [*Cu*^{II}(OH)(O)]$^{+}$ experiences less force than [*Cu*^{III}(OH)(O)]. Whether an electron would be transferred at this point would largely be

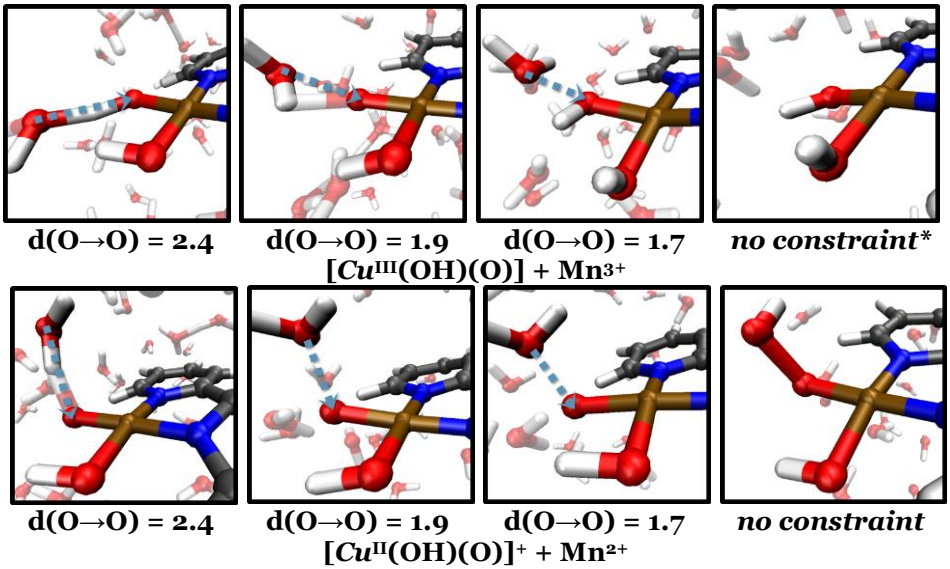

Figure 3.10 Snapshots taken during CPMD calculations of the [Cu^{III}(OH)(O)] intermediate as d(O→O) (blue dotted line) is contracted. *Spin flipped from [Cu^{II}(OH)(O)]$^+$ + Mn^{2+}

dependent on the electronic coupling between the catalyst and the Mn ion.

When the incoming water molecule is 1.7 Å from the oxo ligand of [Cu^{III}(OH)(O)] + Mn^{3+}, a proton is seen to be accepted from a solvent molecule by the oxo group involved in the constraint to give [Cu^{III}(OH)(OH)] (see Figure 3.10, upper panel). [Cu^{III}(OH)(OH)] is also obtained when the multiplicity of [Cu^{II}(OH)(OOH)] + H^+_{solv} + Mn^{2+} is changed to move an electron onto [Cu^{II}(OH)(OOH)]; this momentarily gives [Cu^{III}(OH)(OOH)] + H^+_{solv} + Mn^{3+}. We can therefore conclude that electron removal is indeed necessary to advance through the proposed catalytic cycle. Comparatively, when following the red points ([Cu^{II}(OH)(O)]$^+$ + Mn^{2+}) as d(O→O) is shortened, the proposed [Cu^{II}(OH)(OOH)] intermediate is eventually obtained (Figure 3.10, lower panel). The constraint is then removed and the system allowed to evolve while the bond length of the recently formed bond is monitored. This is seen to stabilise to around 1.50 Å (Figure 3.9, green triangle). This confirms the stability of the proposed [Cu^{II}(OH)(OOH)] intermediate.

Although electron transfer is considered to be favourable from d(O→O) ~2.35 Å, proton transfer is not observed until after d(O→O) = 1.7 Å (see Figure 3.10, lower panel). This proton transfer is mostly dependent on solvent rearrangement. The dependence on solvent rearrangement in these simulations also leads to a 'hysteresis' effect:[51] if the bond is lengthened from the [Cu^{II}(OH)(OOH)] intermediate (Figure 3.9, blue triangles), the intermediate remains deprotonated for some time. This process is shown explicitly in Figure 3.11. Grey arrows show

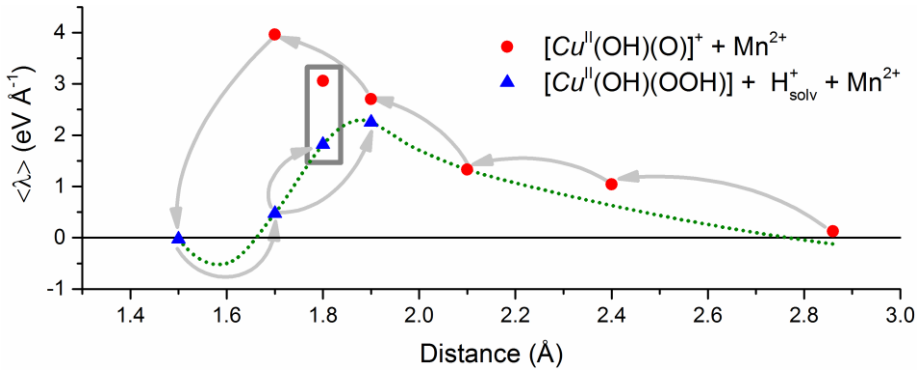

Figure 3.11 The time-averaged constraint force as a function of d(O→O), for $[Cu^{II}(OH)(O)]^+ + Mn^{2+}$ and $[Cu^{II}(OH)(OOH)] + H^+_{solv} + Mn^{2+}$ (as reproduced from Figure 3.9). Grey arrows show sequential order of the simulations. The grey box around the points at 1.8 Å shows the two different mean forces obtained within one single simulation, dependent on proton transfer (see also Figure A3.2). The green dotted line indicates the lowest energy pathway, as per Figure 3.9.

the sequence of simulation. First d(O→O) is contracted for the ionised catalyst ($[Cu^{II}(OH)(O)]^+ + Mn^{2+}$, red circles), then lengthened from the ionised and deprotonated final product ($[Cu^{II}(OH)(OOH)] + H^+_{solv} + Mn^{2+}$, blue triangles). The differences in protonation lead to a marked difference in constraint forces, as bond formation is much more favourable when the extra proton has been released into the solvent.

That solvent configuration has a significant impact on proton release is also demonstrated by the simulation at d(O→O) = 1.8 Å. When increasing d(O→O) from 1.7 to 1.8 Å, a solvent configuration is reached where the proton is transferred back to the catalyst. This results in two different constraint forces within the same simulation, as indicated by the grey box in Figure 3.11. Even though the protonated catalyst does experience a higher constraint force, the system remains stable over the continuation of the simulation for an additional 2.2 ps (as shown in Figure A3.2). Conversely, when increasing d(O→O) from 1.7 to 1.9 Å the catalyst remains deprotonated throughout the entire simulation. Here the sampled solvent configurations favour the solvation of the extra proton.

The catalytic step $[Cu^{III}(OH)(O)] \rightarrow [Cu^{II}(OH)(OOH)]$ can therefore be described as proceeding by the removal of an electron followed by the dissociation of a proton, once the solvent has rearranged such that the proton transfer into the solvent is favourable.[23] That $[Cu^{III}(OH)(O)] \rightarrow [Cu^{II}(OH)(OOH)]$ should be considered the more likely O – O bond formation mechanism is confirmed by a similar investigation of the $[Cu^{III}(OH)(O)] \rightarrow [Cu^{II}(O)(O)]$ step as shown in Figure 3.12, where no transition state was observed along the investigated reaction coordinates.

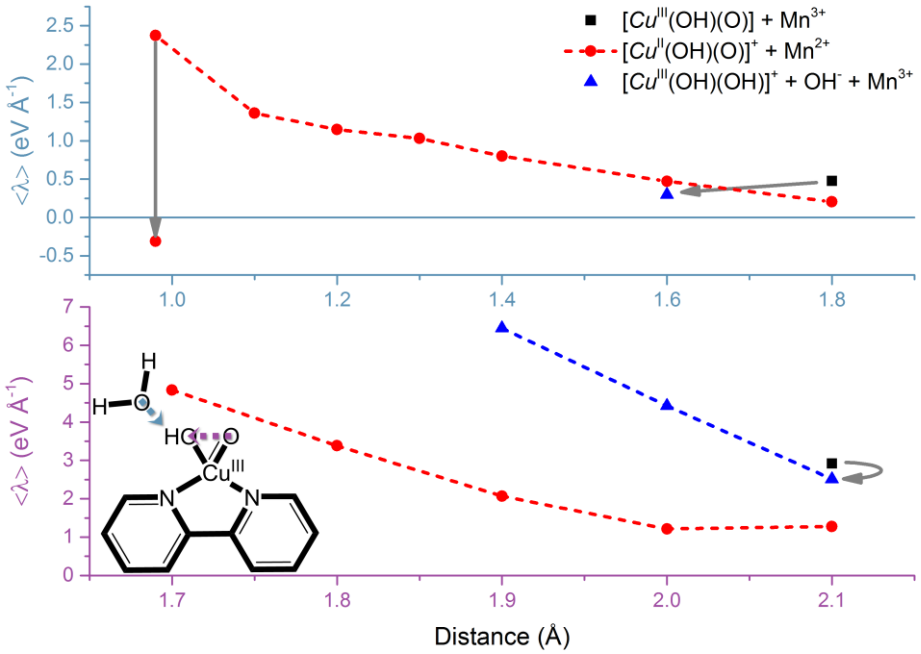

Figure 3.12 The time-averaged constraint force (<λ>) as a function of (top) the d(O→H) distance between the oxygen of a solvent water molecule and the H atom of the hydroxyl ligand (blue dotted line in inset), and (bottom) d(O→O) between the oxygen atoms ligated to the copper centre (pink dotted line in inset). The black square indicates <λ> for the initial [*Cu*^{III}(OH)(O)] + Mn^{3+} intermediate as calculated in the closed system approach. NB. For the [*Cu*^{III}(OH)(O)] + Mn^{3+} system, the average O – O bond length before enforcing any constraints is 2.36 Å, while for [*Cu*^{II}(OH)(O)]$^{+}$ + Mn^{2+} this is 2.39 Å.

For the proton transfer reaction coordinate (Figure 3.12, inset, blue dashed line), the initial [*Cu*^{III}(OH)(O)] + Mn^{3+} (black square, top) intermediate accepts a proton to form the [*Cu*^{III}(OH)(OH)]$^{+}$ + OH^{-} + Mn^{3+} intermediate (blue triangle, top) resulting in a lower <λ>. The red circles (top panel) show the process for the ionised intermediate ([*Cu*^{II}(OH)(O)]$^{+}$ + Mn^{2+}). The proton does not dissociate from the OH ligand , even when an electron has been removed: see the high value of <λ> corresponding to a distance of 1.0 Å where we are forcing the H_3O^+ formation. After a further 1.21 ps of dynamics a proton shuttle occurs in which a proton is accepted by the other oxo group, thus leading back to the initial complex with a very small <λ> (as shown by a grey arrow, top). The [*Cu*^{III}(OH)(O)] → [*Cu*^{II}(O)(O)] step would therefore be very unlikely via this pathway.

For the O – O intermolecular coupling reaction coordinate (Figure 3.12, inset, pink dashed line), the initial [*Cu*^{III}(OH)(O)] + Mn^{3+} (black square, bottom) intermediate again accepts a proton after 90 fs to form the [*Cu*^{III}(OH)(OH)]$^{+}$ + OH^{-} + Mn^{3+} intermediate (blue triangles, bottom). It should be noted that the values for <λ> are significantly higher than those obtained in Figure 3.12 (top).

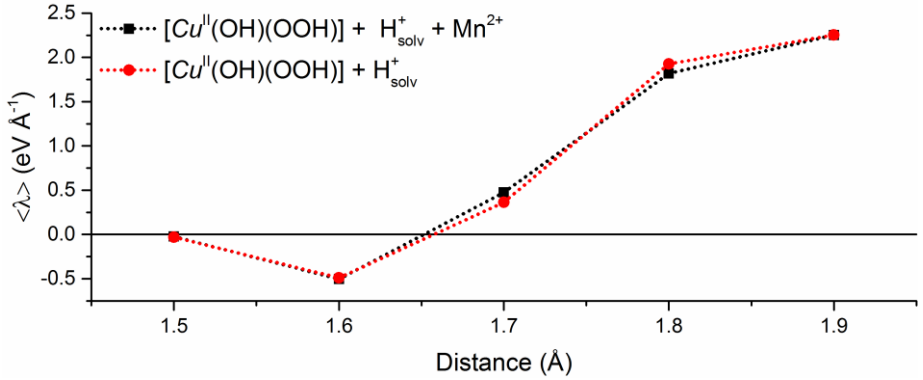

Figure 3.13 The time-averaged constraint force (<λ>) as a function of the O - O distance in the OOH ligating group of the [*Cu*(OH)(OOH)] intermediate, as d(O→O) is lengthened. The black triangles indicate the process as calculated in the closed system approach ([*Cu*^{II}(OH)(OOH)] + H$^{+}_{solv}$ + Mn^{2}, charge = 3^{+}, septet multiplicity), while the red triangles the process calculated without the metal ion ([*Cu*^{II}(OH)(OOH)] + H$^{+}_{solv}$, charge = 1^{+}, triplet multiplicity).

By thermodynamic integration along this reaction coordinate, we obtain a prohibitively high free energy change for both cases.

3.3.5. Implication of Ion Inclusion

To examine the effect of the inclusion of the metal atom, the curve produced via the lengthening of d(O→O), i.e. [*Cu*^{II}(OH)(OOH)] → [*Cu*^{II}(OH)(O)]$^{+}$, is repeated without the metal atom. The same box is used, but with doublet multiplicity and total charge 1^{+}. As the electron would have already been transferred to the electron acceptor at this point, and the proton into solution, the time-averaged constraint force of this constraint should be comparable. These two curves are compared in Figure 3.13, and show very close agreement. The inclusion of the additional metal ion therefore has very little effect on the time-averaged constraint force, and thus the change in free energy of this bond lengthening process.

3.4. Conclusions

The relevant steps of two trial water oxidation catalytic cycles were analysed using a closed system approach in which an electron acceptor is included in a fully solvated simulation setup. Using this approach it is observed that the solvent acts as a proton shuttle, favouring the catalytic cycle which does not include the formation of the [*Cu*^{II}(O)(O)] intermediate (Cycle 1). This is contrary to the expectations based on the static thermodynamic analysis within an implicit solvent model. When investigating the oxygen – oxygen formation step of Cycle 1, it is observed that this reaction proceeds by the electron leaving first, followed by proton transfer when solvent dynamics creates an appropriate hydrogen

bonding network. This closed system approach provides additional insight into PCET catalytic steps by elucidating the dynamic evolution between two stable intermediates.

3.5. References

[1] L. Duan *et al. Nat. Chem.* **2012**, *4*, 418–423.
[2] L. Duan *et al. Proc. Natl. Acad. Sci.* **2012**, *109*, 15584–15588.
[3] L. Duan *et al. Chem. – Eur. J.* **2010**, *16*, 4659–4668.
[4] L. Tong *et al. Angew. Chem. Int. Ed.* **2011**, *50*, 445–449.
[5] N. Kaveevivitchai *et al. Inorg. Chem.* **2012**, *51*, 2930–2939.
[6] A. Savini *et al. Chem. Commun.* **2010**, *46*, 9218–9219.
[7] J. D. Blakemore *et al. J. Am. Chem. Soc.* **2010**, *132*, 16017–16029.
[8] D. E. Polyansky *et al. J. Am. Chem. Soc.* **2011**, *133*, 14649–14665.
[9] D. G. H. Hetterscheid and J. N. H. Reek. *Angew. Chem. Int. Ed.* **2012**, *51*, 9740–9747.
[10] S. M. Barnett *et al. Nat. Chem.* **2012**, *4*, 498–502.
[11] D. J. Wasylenko *et al. Chem. Commun.* **2013**, *49*, 218.
[12] L.-Z. Fu *et al. RSC Adv.* **2014**, *4*, 53674–53680.
[13] J. L. Fillol *et al. Nat. Chem.* **2011**, *3*, 807–813.
[14] K. G. Kottrup and D. G. H. Hetterscheid. *Chem Commun* **2016**, *52*, 2643–2646.
[15] T. Wang *et al. J. Chem. Theory Comput.* **2010**, *6*, 2395–2401.
[16] A. Venturini *et al. Chem. – Eur. J.* **2014**, *20*, 5358–5368.
[17] M. D. Kärkäs *et al. Angew. Chem. Int. Ed.* **2012**, *51*, 11589–11593.
[18] M. Orio *et al. Photosynth. Res.* **2009**, *102*, 443–453.
[19] F. Costanzo *et al. J. Chem. Phys.* **2011**, *134*, 244508.
[20] J. Cheng *et al. J. Chem. Phys.* **2009**, *131*, 154504.
[21] J. Cheng *et al. Acc. Chem. Res.* **2014**, *47*, 3522–3529.
[22] L. Bernasconi *et al. ACS Catal.* **2017**, *7*, 4018–4025.
[23] A. Monti *et al. J. Phys. Chem. C* **2016**, *120*, 23074–23082.
[24] C. Ma *et al. ACS Catal.* **2012**, *2*, 1500–1506.
[25] T. J. Eisenmayer and F. Buda. *ChemPhysChem* **2014**, *15*, 3258–3263.
[26] T. Zhang *et al. J. Am. Chem. Soc.* **2014**, *136*, 273–281.
[27] C. F. Guerra *et al. Theor. Chem. Acc.* **1998**, *99*, 391–403.
[28] G. te Velde *et al. J. Comput. Chem.* **2001**, *22*, 931–967.
[29] SCM. *ADF 2012*; Theoretical Chemistry, Vrije Universiteit, Amsterdam, The Netherlands.
[30] S. Grimme *et al. J. Comput. Chem.* **2011**, *32*, 1456–1465.
[31] M. Swart *et al. Mol. Phys.* **2004**, *102*, 2467–2474.
[32] A. R. Groenhof *et al. J. Am. Chem. Soc.* **2007**, *129*, 6204–6209.
[33] M.-S. Liao *et al. J. Phys. Chem. A* **2007**, *111*, 5927–5935.
[34] J. L. Vallés-Pardo *et al. ChemPhysChem* **2012**, *13*, 140–146.
[35] M. Güell *et al. JBIC J. Biol. Inorg. Chem.* **2009**, *14*, 273–285.
[36] S. Nachimuthu *et al. Chem. Phys.* **2012**, *400*, 8–12.
[37] Bon Kweon Koo. *Bull Korean Chem Soc* **2001**, *22*, 113.
[38] *CPMD*; Copyright IBM Corp 1990-2008, Copyright MPI für Festkörperforschung Stuttgart 1997-2001.
[39] "Accelrys Software Inc." *Discovery Studio Modeling Environment*; Accelrys Software Inc., San Diego: San Diego, 2012.
[40] B. R. Brooks *et al. J. Comput. Chem.* **1983**, *4*, 187–217.
[41] C. Hartwigsen *et al. Phys. Rev. B* **1998**, *58*, 3641–3662.
[42] I.-C. Lin *et al. Phys. Rev. B* **2007**, *75*, 205131.
[43] I.-C. Lin *et al. Phys. Rev. B* **2007**, *75*, 205131.
[44] W. Humphrey *et al. J. Mol. Graph.* **1996**, *14*, 33–38.
[45] *VMD - Visual Molecular Dynamics*; Theoretical Chemistry and Computational Biophysics

Group, University of Illinois, Urbana, U.S.A, 2012.
[46] D. J. Vinyard *et al. Faraday Discuss.* **2015**, *185*, 37–50.
[47] P. E. M. Siegbahn. *Philos. Trans. R. Soc. Lond. B Biol. Sci.* **2008**, *363*, 1221–1228.
[48] F. Acuña-Parés *et al. Chem. - Eur. J.* **2014**, *20*, 5696–5707.
[49] L. Vilella *et al. Dalton Trans.* **2011**, *40*, 11241–11247.
[50] J. Rossmeisl *et al. J. Electroanal. Chem.* **2007**, *607*, 83–89.
[51] B. Ensing *et al. J. Phys. Chem. A* **2001**, *105*, 3300–3310.

Table A3.1 Comparison between geometrical parameters of the metal centre of [*Cu*$(OH)_2$] as calculated with OPBE and B3LYP using two different basis sets. Percentages indicate relative error with respect to experimental data of the Cu(bpy)$(O_2CMe)_2$ crystal structure.[1]

	Cu(bpy)$(O_2CMe)_2$	**OPBE/TZP**		**OPBE/pVQZ**		**B3LYP/TZP**		**B3LYP/pVQZ**	
Cu – N_1 (Å)	2.020	2.068	2.4%	2.000	1.0%	2.097	3.8%	2.043	1.1%
Cu – N_2 (Å)	2.015	2.048	1.6%	2.040	1.2%	2.072	2.8%	2.047	1.6%
Cu – O_1 (Å)	1.952	1.929	1.2%	1.924	1.4%	1.916	1.8%	1.913	2.0%
Cu – O_2 (Å)	1.927	1.922	0.3%	1.909	0.9%	1.915	0.6%	1.922	0.3%
O_1 – Cu – O_2 (°)	90.5	90.7	0.2%	90.9	0.4%	93.0	2.8%	92.7	2.4%
N_1 – Cu – N_2 (°)	79.8	78.7	1.4%	80.2	0.5%	78.3	1.9%	79.3	0.6%
O_1 – Cu – N_2 (°)	172.9	170	1.7%	160.5	7.2%	172	0.5%	165.9	4.0%
O_2 – Cu – N_1 (°)	173.0	166.6	3.7%	165.4	4.4%	167.5	3.2%	159.2	8.0%

Table A3.2 Investigated multiplicities and geometries of possible intermediates as calculated using ADF. ΔE is the energy relative to the lowest energy multiplicity for that intermediate (indicated by asterisks). ΔS^2 is here defined as the difference between the exact and expected value for S^2, which can be considered an indication of the level of spin contamination for that multiplicity.[2]

Intermediate	Charge	Multiplicity	ΔE (eV)	ΔS^2	ΔE (eV)	ΔS^2	Copper conformation
			B3LYP		OPBE		
$[Cu^{II}(OH)_2]$	0	*doublet*	0.00	0.00	0.00	0.00	planar
	0	quartet	2.85	0.02	2.48	0.01	distorted tetrahedral
$[Cu^{III}(OH)(O)]$	0	*singlet*	0.00	0.00	0.00	0.00	planar
	0	triplet	0.03	0.01	0.45	0.01	distorted tetrahedral
$[Cu^{II}(OH)(O)]^-$	-1	*doublet*	0.00	0.00	0.00	0.01	distorted planar
	-1	quartet	1.03	0.02	0.90	0.01	planar
$[Cu^{II}(O)(O)]$	0	*doublet*	0.00	0.01	0.00	0.00	planar
	0	quartet	1.16	0.01	1.70	0.02	distorted tetrahedral
$[Cu^{III}(O)(O)]^+$	+1	singlet	0.33	0.00	0.19	0.00	planar
	+1	*triplet*	0.00	0.01	0.00	0.01	planar
$[Cu^{II}(OH)(OOH)]$	0	doublet	0.00	0.00	0.00	0.00	distorted planar
	0	*quartet*	3.30	0.02	1.90	0.01	distorted tetrahedral
$[Cu^{I}(OH)(OO)]$	0	singlet	0.76	0.00	0.21	0.89	distorted planar
	0	*triplet*	0.00	0.01	0.00	0.01	distorted planar
$[Cu^{I}(OH)(OH_2)]$	0	singlet	-				*H_2O dissociates*
	0	*triplet*	0.00	0.01	0.00	0.00	*$d(Cu - OH_2) = 2.25$, planar*

Table A3.3. Geometrical details of possible intermediates as calculated using ADF (OPBE/TZP).

Intermediate	Cu - O1	Cu - O2	Cu - N1	Cu - N2	O - Cu - O	O1 - O2	O1 - O3
$[Cu^{II}(OH)_2]$	1.916	1.915	2.097	2.072	93.0	2.778	
	1.974	1.977	0.961	1.961	67.8	2.202	
$[Cu^{III}(OH)(O)]$	1.765	1.813	1.952	1.979	85.8	2.435	
	1.805	1.943	2.051	2.091	94.6	2.756	
$[Cu^{II}(OH)(O)]^-$	1.844	1.964	2.101	2.114	88.9	2.669	
	1.819	1.98	2.026	2.045	91.7	2.729	
$[Cu^{II}(O)(O)]$	1.926	1.923	2.011	2.014	44.4	1.453	
	1.854	1.855	2.089	2.097	95.3	2.741	
$[Cu^{III}(O)(O)]^+$	1.837	1.838	1.927	1.928	44.0	1.375	
	1.986	1.984	1.981	1.982	38.6	1.313	
$[Cu^{II}(OH)(OOH)]$	1.966	1.919	2.064	2.064	89.7	2.74	1.444
	2.029	1.895	1.980	1.991	93.0	2.849	1.343
$[Cu^{I}(OH)(OO)]$	1.999	1.900	2.047	2.051	89.8	2.751	1.307
	2.105	1.909	2.049	2.076	90.7	2.858	1.484
$[Cu^{I}(OH)(OH_2)]$	2.253	1.895	1.971	1.965	86.8	2.861	

Table A3.4 Total charge, multiplicities, and the atomic charge of Cu calculated using the Hirshfeld and Voronoi deformation density methods for the investigated intermediates (ADF B3LYP/TZP calculation, using the geometry optimised with OPBE/TZP).

Intermediate	Charge	Multiplicity	Hirschfeld	Voronoi
$[Cu^{II}(OH)_2]$	0	doublet	0.467	0.484
	0	quartet	0.528	0.500
$[Cu^{III}(OH)(O)]$	0	singlet	0.467	0.510
	0	triplet	0.433	0.467
$[Cu^{II}(OH)(O)]^-$	-1	doublet	0.295	0.380
	-1	quartet	0.392	0.439
$[Cu^{II}(O)(O)]$	0	doublet	0.384	0.402
	0	quartet	0.412	0.457
$[Cu^{III}(O)(O)]^+$	+1	singlet	0.572	0.552
	+1	triplet	0.534	0.498
$[Cu^{II}(OH)(OOH)]$	0	doublet	0.462	0.469
	0	quartet	0.458	0.455
$[Cu^{I}(OH)(OO)]$	0	singlet	0.434	0.429
	0	triplet	0.431	0.430
$[Cu^{I}(OH)(OH_2)]$	0	triplet	0.520	0.507

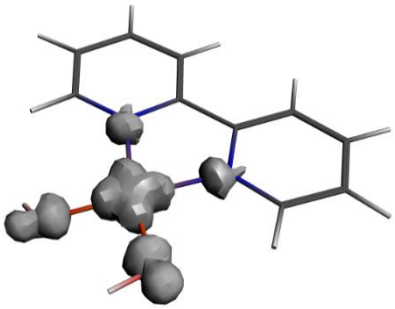

[*Cu*^{II}(OH)$_2$] (doublet)

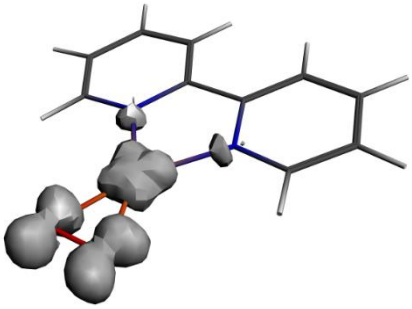

[*Cu*^{II}(O)(O)] (doublet)

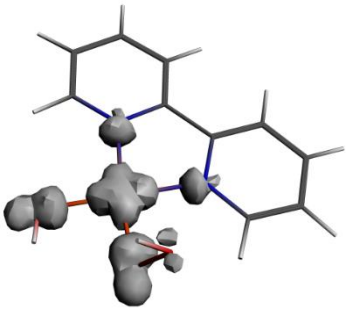

[*Cu*^{II}(OH)(OOH)] (doublet)

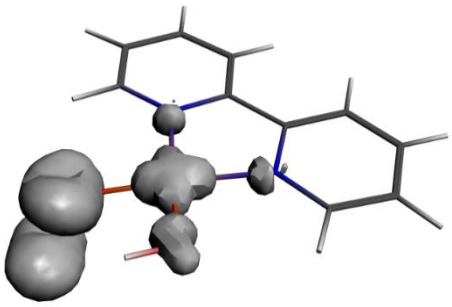

[*Cu*^{I}(OH)(OO)] (triplet)

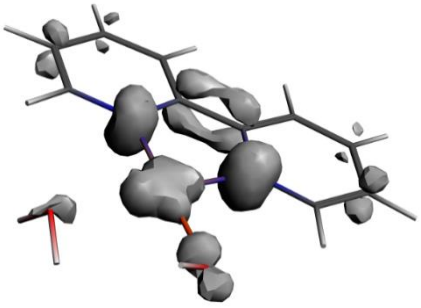

[*Cu*^{I}(OH)(OH$_2$)] (triplet)

Figure A3.1 The localisation of the spin density of the relevant intermediates in Table A3.4, as calculated in ADF (B3LYP/TZP).

3.A.2. Example of convergence of <λ>

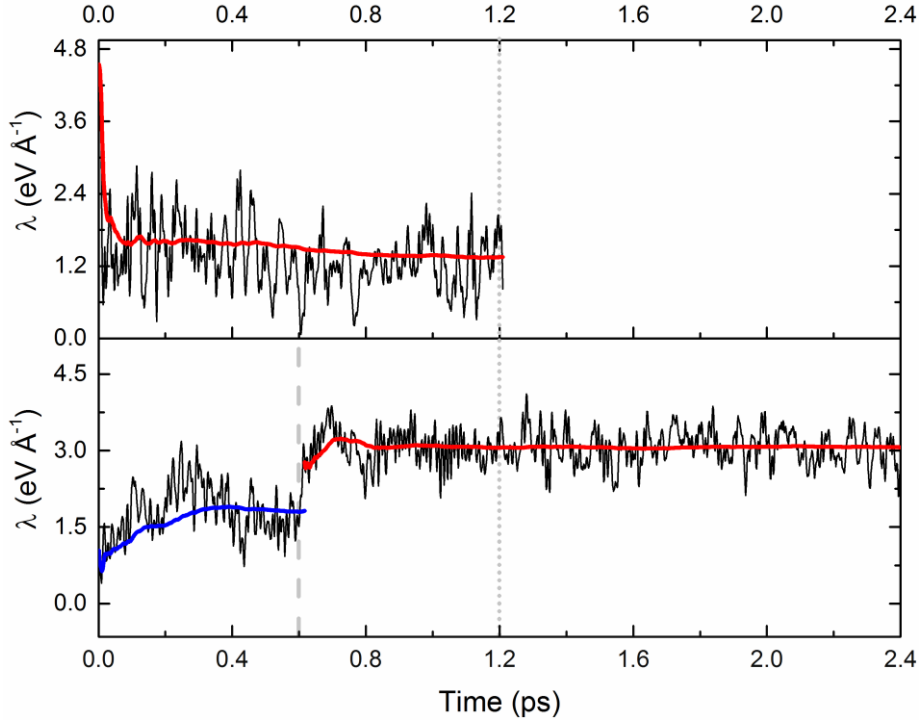

Figure A3.2 The constraint force (λ) as a function of time for two different O - O distance constraints (d(O→O) between the oxo ligand and the oxygen of the incoming water molecule), observed in the investigation of the [Cu^{III}(OH)(O)] intermediate (System 3, [Cu^{II}(OH)(O)]$^{+}$ + Mn^{2+}).

(top) d(O→O) = 2.1 Å as the incoming water molecule is brought increasingly closer. This is a typical constraint run for 1.2 ps (until grey dotted line). The running time-average of λ (<λ>, red line) is seen to converge.

(bottom) d(O→O) = 1.8 Å after lengthening the formed bond for the system with septet multiplicity ([Cu^{II}(OH)(OOH)] + H^{+}_{solv} + Mn^{2+}). This run shows how sensitive λ is to events that occur within the system. After 0.6 ps (grey dashed line), a proton is accepted by the O initially part of the incoming water molecule. <λ> after this event (red line) is seen to converge rapidly, and though the system was allowed to evolve for 1.2 ps beyond the normal run time, no change in <λ> was observed.

Energetic Effects of a Closed System Approach

Chapter Four

4. Energetic Effects of a Closed System Approach

Abstract

When considering water oxidation catalysis theoretically, accounting for the transfer of protons and electrons from one catalytic intermediate to the next remains challenging: correction factors are usually employed to approximate the energetics of electron and proton transfer. Here these energetics were investigated using a closed system approach, which places the catalytic intermediate in a simulation box including proton and electron acceptors, as well as explicit solvent. As a proof of principle, the first two catalytic steps of the mononuclear ruthenium-based water oxidation catalyst $[Ru(cy)(bpy)(H_2O)]^{2+}$ were examined using Car-Parrinello Molecular Dynamics. This investigation shows that this approach offers added insight, not only into the free energy between two stable intermediates, but also into how the solvent environment impacts this dynamic evolution.

This chapter is based on

J. M. de Ruiter, H. J. M. de Groot and F. Buda ""Energetic Effects of a Closed System Approach Including Explicit Proton and Electron Acceptors as Demonstrated by a Mononuclear Ruthenium Water Oxidation Catalyst."
ChemCatChem, **2018**, doi: 10.1002/cctc.201801093

4.1. The Call for the Closed System Approach – Energetics

In the optimisation of WOCs, computational techniques are increasingly employed to test proposed WOC design principles.[1–8] When evaluating proposed catalytic cycles, the free energies of the various catalytic intermediates are compared.[1–6] This comparison often uses correction factors to approximate the energetic contributions of the protons and electrons transferred during the catalytic step. [1,3,5,9–12] Here the pitfalls of the commonly employed approach are highlighted, and an improved framework is suggested based on the CSA.

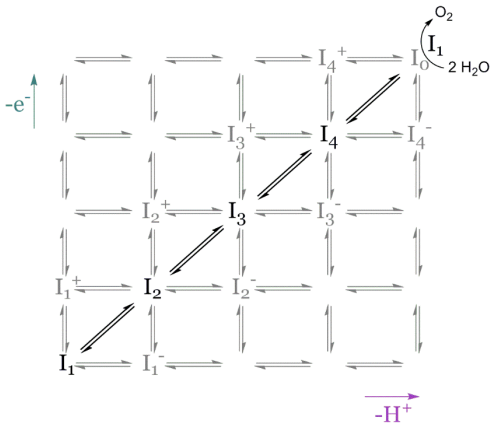

Figure 4.1 The four PCET steps between the catalytic intermediates I_1 - I_0. Vertical lines denote electron transfer, horizontal lines proton transfer. Stable intermediates are shown in black. The ligand exchange $I_0 + 2H_2O \rightarrow I_1 + O_2$ is also shown.

Consider the PCET reaction

$$I_i \longrightarrow I_{i+1} + H^+ + e^-, \tag{4.1}$$

shown in Figure 4.1, which has a change in free energy

$$\Delta G(I_i \longrightarrow I_{i+1}) = G(I_{i+1}) - G(I_i) + \Delta G(H^+) + \Delta G(e^-). \tag{4.2}$$

As mentioned in Chapter One, G has traditionally been approximated by

$$G = (E_{vac} + ZPE_{vac} - TS_{vac}) + \delta E_{solv}, \tag{4.3}$$

$$\delta E_{solv} = E_{solv} - E_{vac}. \tag{4.4}$$

This becomes problematic because it calls for the solvation energy of a proton $\Delta G_{solv}(H^+)$ =-11.45 eV,[13] which will always dominate ΔG completely: ΔG is usually of the order of 1 eV. In the past,[14,15] the energetic contributions of the proton and electron have often been approximated by combining the proton and electron into ½H_2. Upon closer inspection the validity of the ½H_2 approximation is somewhat questionable, as in the PCET reactions considered H^+ is always bonded to another ion. The transfer of H^+ is a combination of the formation of one O – H bond and the breaking of another, with an intermediate step where H is coordinated in between. As noted by Nachimuthu et al. previously,[16] *"modelling proton transfer reactions is often challenging because of the complexity of processes involving H-bond network rearrangement."*

And yet, it is this complexity of the network rearrangement processes that is ignored when using the ½ H_2 approximation. This may have been sufficient when considering heterogeneous catalysts, but as we move into molecular catalysts the how and why of the PCET process needs to be addressed. Two intermediates can no longer be seen as isolated from each other, instead we must also seek to optimise the processes between them. To do so, explicit water molecules and a metal ion (Me) are included within the simulation box, to act as proton and electron acceptors respectively. In this way the charge carriers and the processes via which they are transferred from the catalyst can be considered explicitly. For the PCET reaction shown in Eqn. (4.1), the equivalent equation in the simulation box is

$$I_i + Me^{3+} \longrightarrow I_{i+1} + H^+_{solv} + Me^{2+}, \qquad (4.5)$$

where H^+_{solv} denotes the solvated proton, which is often part of a more complicated structure.[17–19] We can then decouple the PCET reaction into an electron- and proton-transfer process.

For the electron transfer step

$$I_i + Me^{3+} \longrightarrow {I_i}^+ + Me^{2+}. \qquad (4.6)$$

In the context of the CSA methodology, the energy needed to transfer an electron from the catalytic intermediate to the electron acceptor can be calculated by

$$\Delta E_{e^-} = \langle E_{KS}({I_i}^+ + Me^{2+}) \rangle - \langle E_{KS}(I_i + Me^{3+}) \rangle, \qquad (4.7)$$

where $\langle E_{KS} \rangle$ is the time-averaged KS energy at 300 K. One should note that ΔE_{e^-} also includes the reorganisation energetic contributions resulting from the electron transfer.[20] This includes contributions from internal vibrational and

external solvent rearrangement. Because the number of particles, charges, bonding patterns, and conformations of the reactants and products in Eqn. (4.6) remains the same, the change in entropy and zero point energy will be negligible, i.e. $\Delta E_{e^-} \approx \Delta G_{e^-}$.

The proton-transfer process

$$I_i{}^+ \longrightarrow I_{i+1} + H^+_{solv} \tag{4.8}$$

may be investigated using constrained CPMD along the reaction coordinate of proton solvation. ΔG_{H^+} can then be calculated for each reaction step according to Eqn. (1.24) in Chapter 1, where the respective x = d(O→H) (see also Figure 4.2).

So practically, in CSA the total change in energy for the $I_i \longrightarrow I_{i+1}$ PCET reaction simulation is given by

$$\Delta G_{CSA} = \Delta G_{H^+} + \Delta E_{e^-}. \tag{4.9}$$

ΔE_{e^-} includes energetic contributions from both the oxidation of the catalyst, as well as the reduction of Me^{3+}. If these events are to be considered independently from each other,

$$\Delta E_{e^-} = \Delta E_{e^-}(I_i \longrightarrow I_i{}^+) + \Delta E_{e^-}(Me^{3+} \longrightarrow Me^{2+}), \tag{4.10}$$

then it is of crucial importance that $\Delta E_{e^-}(Me^{3+} \longrightarrow Me^{2+})$ remains constant throughout the catalytic cycle. If this is the case, then the change in free energy for the catalyst would be given by

$$\begin{aligned} \Delta G(I_i \longrightarrow I_{i+1}) &= \Delta G_{H^+}(I_i \longrightarrow I_{i+1}) + \Delta G_{e^-}(I_i \longrightarrow I_{i+1}) \\ &= \Delta G_{H^+}(I_i \longrightarrow I_{i+1}) \\ &\quad + \left(\Delta E_{e^-} - \Delta E_{e^-}(Me^{3+} \longrightarrow Me^{2+})\right). \end{aligned} \tag{4.11}$$

Via this formalism, the way has been paved for an energetic consideration of the *process* of a reaction step which includes both electron and proton transfer. Although this transcends the static consideration which uses the correction term ½ H_2, it does introduce the extra complication of the energetic contribution due to the electron acceptor. We propose that if this contribution is kept constant throughout the catalytic cycle, it will provide less of a complication than one may initially expect.

To demonstrate this methodology the ruthenium based mononuclear molecular

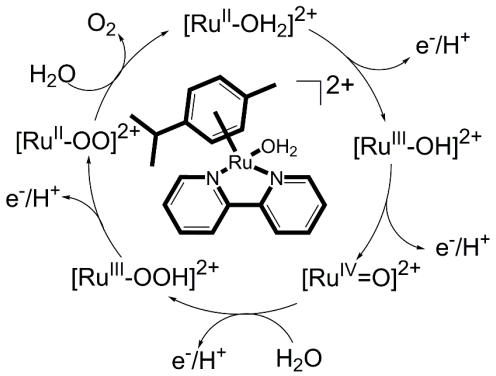

Scheme 4.1 Proposed catalytic cycle for water oxidation by *Ru*-bpy. Inset: Schematic structure of *Ru*-bpy.

WOC *Ru*-bpy is used, whose catalytic cycle is described in Chapter Two (see also Scheme 4.1). *Ru*-bpy provides an excellent text case as its catalytic cycle has been explored both experimentally and computationally using static methods.[21] Furthermore, it has a relatively small number of atoms, which for a test case is an attractive property computationally. Here the first and second catalytic PCET steps of this WOC are examined within CSA. The results of this are then compared to experimental data, as well as computational data obtained using static methods.

4.2. Computational Method and Details

The CPMD program for AIMD was used to examine the explicitly solvated systems.[22] The solvent environment for the CPMD simulations was generated using Discovery Studio 2.5.[23] The solvent was equilibrated for 0.2 ns using the CHARMM force field and CFF partial charge parameters at 300 K,[24] while the catalyst was kept fixed. The volume was then adjusted using constant pressure for 0.2 ns, after which the system was further allowed to evolve with constant volume for 2 ns. Subsequently CPMD calculations were performed in the canonical NVT ensemble at 300 K, using GTH pseudopotentials for the transition metals,[25] DCACP pseudopotentials for the remaining atoms,[26] and the OPBE exchange-correlation functional.[27] KS orbitals are expanded on a plane wave basis set with an energy cut-off of 70 Ry. A time step of 5 a.u. = 0.121 fs was used. Image rendering for the CPMD output was done using VMD.[28,29]

The general methodology for the CPMD simulations was as follows:

a. The system was initially allowed to equilibrate with CPMD for 0.1 ps.
b. A solvent water molecule was constrained at progressively closer distances to one of the protons of the water molecule ligated to the Ru centre (Figure 4.2), at 0.1 Å intervals. The system is allowed to evolve for at least 1 ps to allow the time-averaged constraint force $\langle\lambda\rangle_x$ to stabilise.

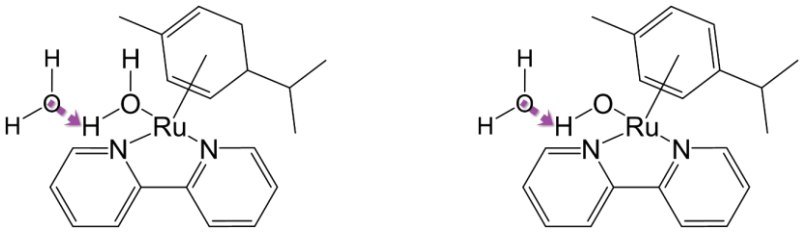

Figure 4.2 The distance constraints d(O→H), shown in purple, considered in this chapter for (left) $[Ru^{II}\text{-}OH_2]^{2+}$ + H_2O_{solv} and (right) $[Ru^{III}\text{-}OH]^{2+}$ + H_2O_{solv}.

In cases where stabilisation was difficult, simulation length was extended to a maximum of 2.5 ps.

c. If d(O→H) was contracted to 1.0 Å, the distance constraint was then removed and the system allowed to evolve for 1 ps.
d. If the formed bond is stable, <λ> at this distance is set to 0. <λ> is then fitted with a 100 pt Akima Spline,[30,31] a fit based on cubic functions. Cubic-based functions have long been used as a fitting method for <λ>.[32]

The simulation box

Simulations are performed on the catalytic intermediate and an Mn^{2+} or Mn^{3+} ion within a 17.52 × 15.78 × 13.65 $Å^3$ box with 94 water molecules, total charge 5^+. The water environment around the Mn ion was constrained to avoid spurious effects on ΔG due to changes in the coordination sphere of the electron acceptor. The coordination sphere is stabilised by constraining the coordination numbers around the Mn ion. The number of oxygen atoms is constrained to four, based on unconstrained simulations where the $Mn^{2+}(H_2O)_4$ structure was formed spontaneously (see Appendix 4.A.1). The coordination radius, r_c = 2.25 Å was also determined from these unconstrained Mn simulations. At 2.25 Å the radial distribution function of O atoms around Mn was zero after the first solvation shell. The parameter κ = 9.4 $Å^{-1}$, where κ^{-1} is the width of the transition region, is chosen such that κ^{-1} is significantly smaller than r_c.[33]

Although the four-fold coordination is anomalous for Mn in water, it can be attributed to the relatively close location of the charged catalyst affecting the Mn ion. Mn chemistry has been shown to be very sensitive to the charge of the complex, as well as the surrounding environment.[34] Each O atom was saturated with two H atoms using r_c = 1.2 Å and κ = 17.6 $Å^{-1}$. 1.2 Å may be considered the H – O distance at which a proton is equally shared between two oxygens,[35] which makes it an appropriate r_c.

$[Ru^{II}\text{-}OH_2]^{2+}$ + Mn^{3+}

In order to calculate ΔE_e–, a d(O→H) = 1.6 Å was imposed for 2 ps for $[Ru^{II}\text{-}OH_2]^{2+}$ + Mn^{3+} (System **1** in Table 4.1). The multiplicity was then flipped to a septet to give $[Ru^{III}\text{-}OH_2]^{3+}$ + Mn^{2+} (System **2** in Table 4.1), and the system

Table 4.1 Summary of the systems considered. q_{tot} is the total charge of the system, 2S+1 the spin multiplicity, and S_{cat} and S_{Mn} the spin of the catalyst and Mn ion respectively.

		q_{tot}	$(2S+1)_{tot}$	S_{cat}	S_{Mn}
1	$[Ru^{II}\text{-}OH_2]^{2+} + Mn^{3+}$	5	5	0	2
2	$[Ru^{III}\text{-}OH_2]^{3+} + Mn^{2+}$	5	7	1/2	5/2
3	$[Ru^{III}\text{-}OH]^{2+} + Mn^{3+}$	5	6	1/2	2
4	$[Ru^{IV}\text{-}OH]^{3+} + Mn^{2+}$	5	8	1	5/2

allowed to evolve for a further 2 ps. For the calculation of ΔG_{H^+} the system was allowed to evolve for at least 1 ps for each d(O→H): 1.4, 1.3, 1.2, 1.1, and 1.0 Å.

$[Ru^{III}\text{-}OH]^{2+} + Mn^{3+}$

The initial geometry was obtained by removing the solvated proton once the final product had stabilised during the unconstrained ΔG_{H^+} calculation for $[Ru\text{-}OH_2]^{3+} + Mn^{2+}$ (System **2**). The $[Ru^{III}\text{-}OH]^{2+} + Mn^{3+}$ system was equilibrated for 0.5 ps with sextet multiplicity (System **3** in Table 4.1). This system was allowed to evolve for 2.5 ps, then for 2.5 ps with octet multiplicity $[Ru^{IV}\text{-}OH]^{3+} + Mn^{2+}$ (System **4** in Table 4.1).

In order to calculate ΔE_{e^-} the $[Ru^{III}\text{-}OH]^{2+} + Mn^{3+}$ system after 2.5 ps with sextet multiplicity was restarted. It was allowed to evolve for 2.5 ps with d(O→H) = 2.04 Å, where d(O→H) was initiated from the restarted geometry. The multiplicity was then flipped to octet multiplicity $[Ru^{IV}\text{-}OH]^{3+} + Mn^{2+}$ (System **4**), and the system allowed to evolve for a further 2.5 ps. For the calculation of ΔG_{H^+} d(O→H) was contracted from 2.04 Å, d(O→H) = 1.9, 1.7, 1.5, 1.4, 1.3, 1.2, 1.1, 1.0 Å, where the initial contraction was more rapid.

4.3. Results and Discussion

The first two catalytic steps of the ruthenium-based WOC were investigated within the CSA. The catalytic intermediates and electron- and proton-transfer steps examined are shown in Scheme 4.2. Analogous to cyclic voltammetry, we first removed an electron from the catalyst (green arrows, Scheme 4.2), and then observe how the system responds. Proton transfer (pink arrows, Scheme 4.2) was investigated by means of constrained CPMD. In Appendix 4.A.2 the $[Ru^{II}\text{-}OH_2]^{2+} + Mn^{3+} \rightleftharpoons [Ru^{II}\text{-}OH]^{+} + H^{+}_{solv} + Mn^{3+}$ proton transfer process is discussed, which would be a proton-first pathway (e.g. $I_1 \rightarrow I_1^-$ as shown in the inset in Scheme 4.2, which is reproduced from Figure 4.1.).

4.3.1. Energetic analysis of the PCET step $[Ru^{II}\text{-}OH_2]^{2+} \rightarrow [Ru^{III}\text{-}OH]^{2+}$

First the PCET step $[Ru^{II}\text{-}OH_2]^{2+} \rightarrow [Ru^{III}\text{-}OH]^{2+}$ (cf. Scheme 4.2: $[Ru^{II}\text{-}OH_2]^{2+} + Mn^{3+} \rightleftharpoons [Ru^{III}\text{-}OH_2]^{3+} + Mn^{2+} \rightleftharpoons [Ru^{III}\text{-}OH]^{2+} + H^{+}_{solv} + Mn^{2+}$) is analysed. Considering the proton transfer process after electron transfer, $[Ru^{III}\text{-}OH_2]^{3+} + Mn^{2+} \rightleftharpoons [Ru^{III}\text{-}OH]^{2+} + H^{+}_{solv} + Mn^{2+}$ (Figure 4.3, top), the variation of $\langle\lambda\rangle$ along the reaction coordinate is well in line with a normal activated reaction profile. At d(O→H) = 1.4 Å $\langle\lambda\rangle$ is only slightly above zero. When d(O→H) = 1.2 Å, the distance between the ligated water oxygen and the proton involved in the constraint is (1.20 ± 0.06) Å. $\langle\lambda\rangle$ is very close to zero, indicating the transition state, and the proton is equidistant between the two oxygen atoms.

At d(O→H) = 1.1 Å the standard deviation is notably larger. During the d(O→H) = 1.1 Å simulation there is significant rearrangement in the solvent surrounding the reaction site, in preparation for proton diffusion into the solvent. This diffusion is facilitated by an appropriate 'water wire'. We define a water wire to be a chain of water molecules which are hydrogen bonded together such that a proton may transfer rapidly along it. The proton can be considered to be delocalised along these water wires.[36] The formation of a water wire has a large effect on λ. If a suitable wire has formed, the formation of the d(O→H) bond is more favourable as the extra proton on the solvent molecule may diffuse away and $\langle\lambda\rangle$ is negative. The extra proton cannot be released from the solvent molecule if this water wire is broken, so forming the d(O→H) bond is unfavourable. At these moments λ is seen to be positive. After the simulation with d(O→H) = 1.0 Å, the distance constraint is released and the system is again allowed to evolve freely. The formed O – H bond has an equilibrium distance of 0.97 Å. We set $\langle\lambda\rangle$ = 0 at that distance, as shown in Figure 4.3 (top).

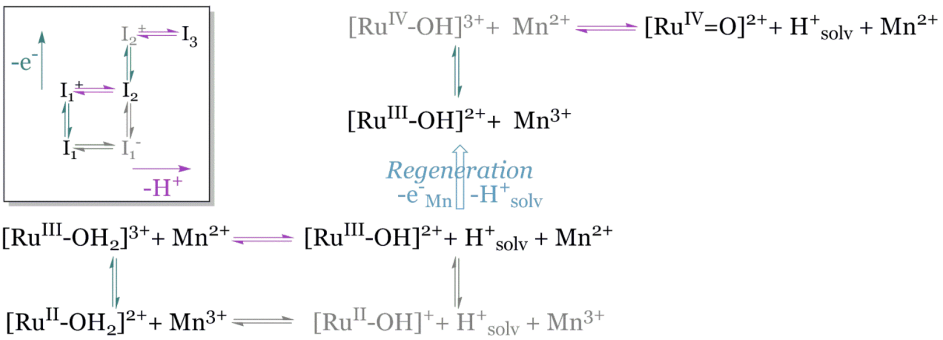

Scheme 4.2 The electron- and proton-transfer steps examined in this work. Vertical lines denote electron transfer, horizontal lines proton transfer. The regeneration step corresponds to the removal of an electron from the Mn ion, as well as the removal of the solvated proton. Stable intermediates are shown in black, unstable intermediates in grey. The inset shows the corresponding intermediates in Figure 4.1.

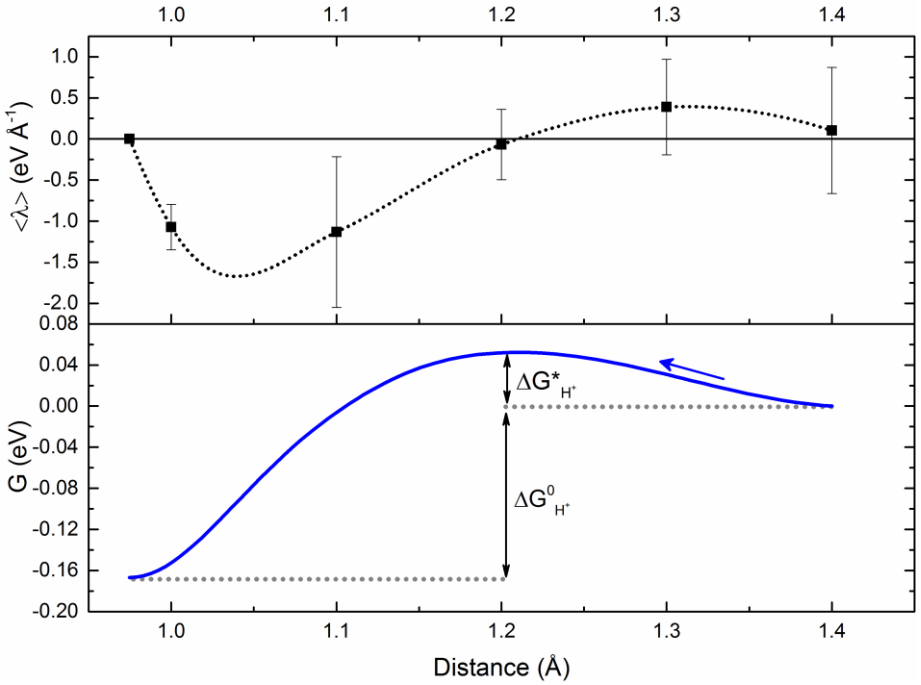

Figure 4.3 (top)The time-averaged constraint force (<λ>) as a function of d(O→H). This analysis is performed for $[Ru^{III}\text{-}OH_2]^{3+}$ + Mn^{2+} ⇌ $[Ru^{III}\text{-}OH]^{2+}$ + H^+_{solv} + Mn^{2+}. The error bars show standard deviations. The dotted line shows the fit of the calculated points. (bottom) The integral of the <λ> fit with respect to distance. The definite integral has a value $\Delta G^0_{H^+}$ = -0.17 eV (-3.8 kcal/mol). $\Delta G^*_{H^+}$ = 0.05 eV (1.2 kcal/mol)

The free energy profile of the complete proton transfer into solvent was obtained from integrating the fit of <λ> and is shown in Figure 4.3 (bottom). This gives a $\Delta G^0_{H^+}$ = (-0.2 ± 0.1) eV (see Appendix 4.A.3), and a transition state energy $\Delta G^*_{H^+}$ = 0.05 eV. Because $\Delta G^0_{H^+}$ is less than zero we can conclude that proton transfer is thermodynamically favourable, once the electron has been removed from the catalyst. An electron transfer energy ΔE_{e^-} = (1.8 ± 1.0) eV was obtained from the time-averaged KS Energy according to Eqn. (4.7), with the distant constraint d(O → H) = 1.6 Å (purple arrow in the left panel of Figure 4.2). This distance corresponds to a typical hydrogen bond distance at equilibrium where <λ> is around 0. ΔG_{CSA} = (1.6 ± 1.0) eV can then be calculated using Eqn. (4.9). Table 4.2 summarizes the total free energy differences for the two PCET reactions.

4.3.2. Proton Diffusion $[Ru^{III}\text{-}OH_2]^{3+}$ → $[Ru^{III}\text{-}OH]^{2+}$

Above it was concluded that proton transfer into the solvent is dependent on the proton at the reaction site having access to a viable water wire. During normal solvent dynamics these wires are formed and broken as water molecules move and rotate. The solvent environment during potential proton transfer was

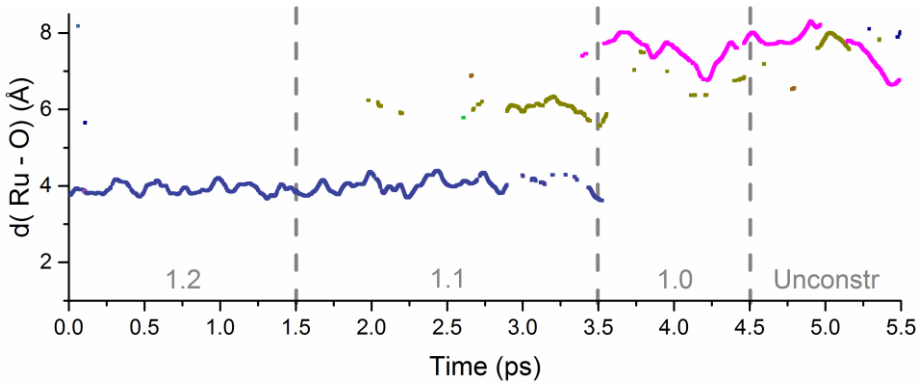

Figure 4.4 The distance between Ru and H_3O^+, defined as an oxygen atom with 3 H within a radius of 1.2 Å, as measured for the CPMD simulations showing diffusion of a single released proton for $[Ru^{III}\text{-}OH_2]^{3+} + Mn^{2+} \rightleftharpoons [Ru^{III}\text{-}OH]^{2+} + H^+_{solv} + Mn^{2+}$. d(O→H) is noted in grey, and subsequent runs with decreasing d(O→H) are separated by dashed lines. According to the simulation, only one oxygen is in the H_3O^+ form at any time, and although the proton associates with seven different oxygens during the simulation, indicated with different colours, it is primarily bonded to three oxygens (blue, gold and magenta).

therefore examined, scanning to identify whether a solvent O atom was bonded to a number of protons different from two i.e. whether it was an OH^- or H_3O^+ ion. If a proton is within 1.2 Å of an O atom, it is considered to be bonded.[35] For the H_3O^+, the distance to the Ru catalytic centre, taking periodic boundaries into account, was then plotted as a function of time (Figure 4.4). This then gives an overview of how the H^+ moves through the solvent, visiting seven different oxygens as it travels from the first to the third hydration shell.

During the d(O→H) = 1.2 Å simulation there is already an initial attempt at proton transfer from the first solvation shell at around 4 Å, to the second solvation shell at around 6 Å. Towards the end of the d(O→H) = 1.1 Å simulation the proton resides mainly within the second solvation shell, though it is still shared with the first. At the start of the d(O→H) = 1.0 Å simulation the proton has been transferred into the third solvation shell at 8 Å. After releasing the distance constraint, the proton remains in the third solvation shell for the 1 ps duration of the simulation, though it is mobile: the distance between its O atom and the ruthenium atom of the catalyst ranges between 6.5 and 8.9 Å. Of further interest here, is that the mobility of the water molecules themselves is also shown. During the d(O→H) = 1.1 Å simulation the proton is transferred to a water molecule in the second solvation shell (gold). During the simulation after d(O→H) has been released, at around 5 ps, the proton is again transferred to this water molecule, which has now moved into the third solvation shell.

4.3.3. Energetic analysis of the PCET step $[Ru^{III}\text{-}OH]^{2+} \rightarrow [Ru^{IV}{=}O]^{2+}$

In the reaction from $[Ru^{III}\text{-}OH]^{2+}$ to $[Ru^{IV}{=}O]^{2+}$, the second PCET step (cf.

Scheme 4.2: $[Ru^{III}\text{-}OH]^{2+} + Mn^{3+} \rightleftharpoons [Ru^{IV}\text{-}OH]^{3+} + Mn^{2+} \rightleftharpoons [Ru^{IV}{=}O]^{2+} + H^{+}_{solv} + Mn^{2+}$), the catalyst changes multiplicity from doublet to triplet, where spin density is localised on the metal centre and on the oxo ligand. In the triplet state, it is very unfavourable for the proton to remain on the oxo ligand, and so proton release should be thermodynamically favourable. This would lead to spontaneous proton release once the multiplicity of the system has been flipped. To investigate this, we first consider the system without an applied d(O→H).

Unconstrained

When $[Ru^{III}\text{-}OH]^{2+} + Mn^{3+}$ is restarted as $[Ru^{IV}\text{-}OH]^{3+} + Mn^{2+}$, without an applied d(O→H), there is proton transfer into the first solvation shell after 0.8 ps. In Figure 4.5 the relative positions of the "non-water" O atoms are shown as the proton is solvated, and the Ru – O bond contracts and stabilises. For clarity, this is decomposed into the various species present: H_3O, and the O atom ligated to

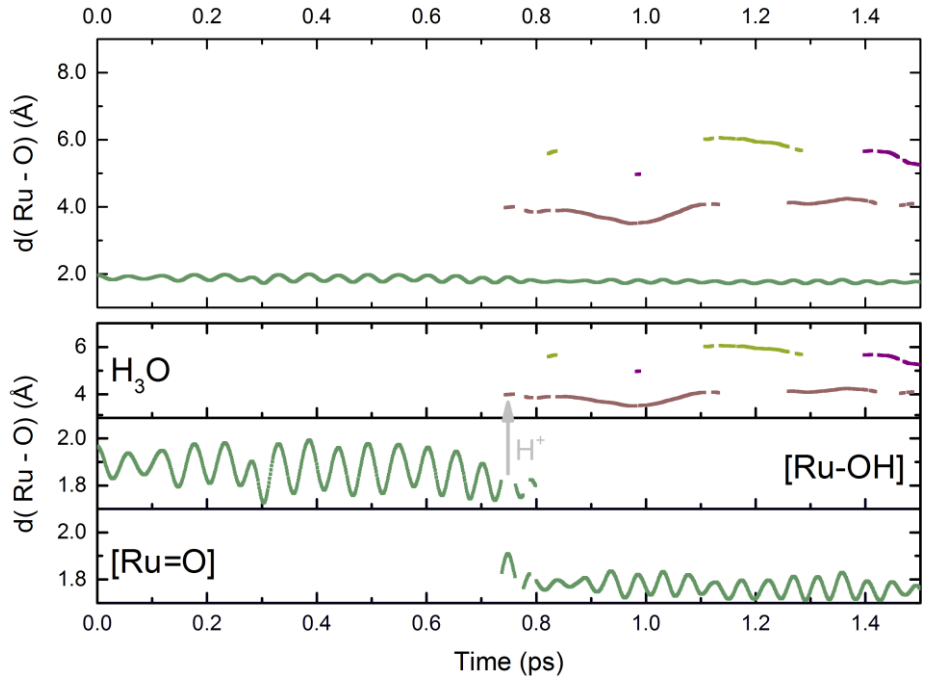

Figure 4.5 (top) The distance between Ru and H_3O^+, OH^- and O^{2-} as measured during $[Ru^{IV}\text{-}OH]^{3+} + Mn^{2+} \rightarrow [Ru^{IV}{=}O]^{2+} + H^{+}_{solv} + Mn^{2+}$, where → indicates spontaneous proton transfer from the catalyst into the solvent. The ions are defined by the number of H within a radius of 1.2 Å of the oxygen, and are specified in (bottom): H_3O - three H atoms, [Ru-OH] - one H atom, [Ru=O] - no H atoms. At first the oxygen ligated to the Ru centre has one proton bonded to it ([Ru-OH], green trace), but at around 0.8 ps a proton is transferred. The oxygen ligated to the Ru centre then has no bonded protons ([Ru=O], green trace), and the Ru - O distance is seen to shorten and stabilise. Meanwhile the excess proton is transferred to an oxygen in the first solvation shell (H_3O, brown trace). It then continues to interact with three different oxygens within the solvent (brown, light green, pink).

the Ru centre as first OH, then O, ligand. After 0.8 ps, a proton is transferred from the ligated OH to the first solvation shell at 4 Å. This proton then interacts with two different water molecules in the second solvation shell, much like the previous system considered in which proton diffusion was successful. The Ru – O distance reaches equilibrium fairly quickly. This simulation encompasses the entire proton transfer into solution. The difference in time-averaged KS energies between $[Ru^{IV}=O]^{2+} + H^{+}_{solv} + Mn^{2+}$ and $[Ru^{III}\text{-}OH]^{2+} + Mn^{3+}$ is (2.7 ± 0.7) eV. This encompasses both electron and proton transfer.

Constrained

To allow for a quantification of the proton and electron transfer energies independently, as well as allowing for a systematic comparison with the first catalytic step, $[Ru^{IV}\text{-}OH]^{3+} + Mn^{2+} \rightleftharpoons [Ru^{IV}=O]^{2+} + H^{+}_{solv} + Mn^{2+}$ was also considered with constrained CPMD. In the unconstrained simulation of this step (as discussed above), spontaneous proton transfer was observed. If this observation is translated to constrained proton transfer, i.e. along d(O→H) as defined in Figure 4.2 (right), <λ> should be less than 0: a force exists in the direction of transfer. As shown in Figure 4.6 (top), <λ> does indeed remain

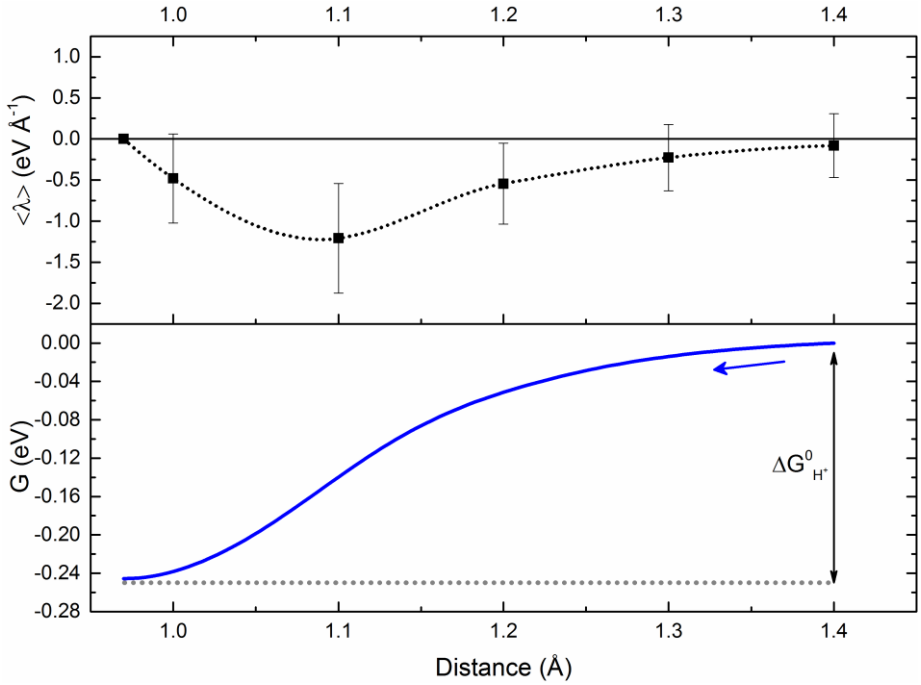

Figure 4.6 (top) The time-averaged constraint force (<λ>) as a function of d(O→H) between one of the ligated water hydrogens and a solvent water oxygen for $[Ru^{IV}\text{-}OH]^{3+} + Mn^{2+} \rightleftharpoons [Ru^{IV}=O]^{2+} + H^{+}_{solv} + Mn^{2+}$. (bottom) The integral of the interpolated <λ> fit with respect to distance. The definite integral has a value $\Delta G^{0}_{H^{+}}$ = -0.25 eV (-5.8 kcal/mol).

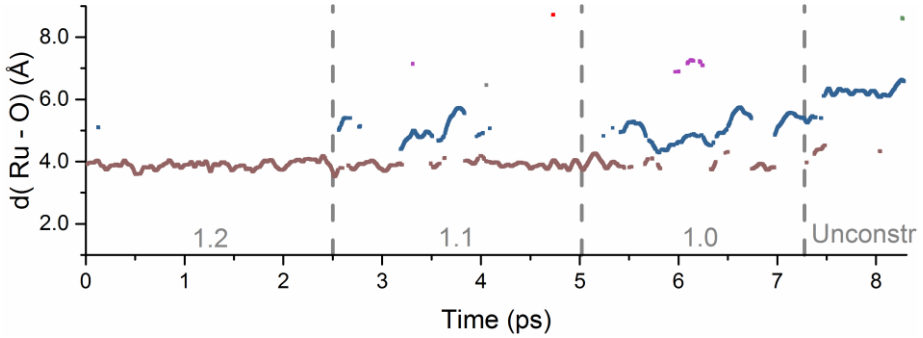

Figure 4.7 The distance between Ru and the H_3O^+ ion associated with the proton transferred during $[Ru^{IV}\text{-}OH]^{3+} + Mn^{2+} \rightleftharpoons [Ru^{IV}{=}O]^{2+} + H^+_{solv} + Mn^{2+}$. d(O→H) is noted in grey, and subsequent runs with decreasing d(O→H) are separated by dashed lines. The proton is primarily associated with an oxygen in the first solvation shell (brown trace), and interacts with, then transfers to, the oxygen with the dark blue trace. There are a number of momentary interactions between the proton and other oxygens; these oxygens each have a different coloured trace.

negative, with a minimum at 1.1 Å. The newly formed O – H bond is stable, with a bond distance of (0.970 ± 0.009) Å.

<λ> is integrated to give the free energy profile (Figure 4.6 , bottom). This gives $\Delta G^0_{H^+}$ = (-0.3 ± 0.2) eV (see also Appendix 4.A.3). Using Eqn. (4.7) the electron transfer energy is calculated as ΔE_{e^-} = (2.3 ± 0.8) eV, and so, from Eqn. (4.9), ΔG_{CSA} = (2.1 ± 0.8) eV; this is also noted in the summarising Table 4.2. For the unconstrained case the change in KS energies between $[Ru^{IV}\text{-}OH]^{3+} + Mn^{2+} \rightarrow [Ru^{IV}{=}O]^{2+} + H^+_{solv} + Mn^{2+}$ and $[Ru^{III}\text{-}OH] + Mn^{3+}$ was (2.7 ± 0.7) eV. Comparing this to ΔG_{CSA}, the two values do fall within the standard deviation of each other. The differences between the two values will, in part, be due to the slightly different final configurations of the solvated proton.

As in the case for the first catalytic step, for $[Ru^{IV}\text{-}OH]^{3+} + Mn^{2+} \rightleftharpoons [Ru^{IV}{=}O]^{2+} + H^+_{solv} + Mn^{2+}$ the first attempt at proton transfer from the first solvation shell, at 4 Å, to the second solvation shell, now at around 5 Å, occurs in the d(O→H) = 1.1 Å simulation (Figure 4.7). However, instead of moving into the third shell, it collapses back to the first solvation shell within the same d(O→H) = 1.1 Å simulation. The extra proton remains shared between these two solvation shells, with brief transfers to the third shell. The water molecule in the second solvation shell receiving the proton gradually moves away from the reaction site, until, during the simulation without distance constraint (Unconstr), the additional proton stabilises in the second solvation shell (Figure 4.7, blue trace). The final simulation ends with the additional proton on a water molecule around 8.7 Å from the Ru catalytic centre.

4.3.4. Experimental Comparison and Evaluation

One of the dilemmas in comparing the values of ΔG obtained so far to experiment is that the values of ΔG still contain a contribution from the electron acceptor. Although one could use reference data for the experimental or calculated redox potentials of Mn, this would not be methodologically rigorous. Instead we introduce the quantity

$$\Delta(\Delta G) = \Delta G(I_i \longrightarrow I_{i+1}) - \Delta G(I_{i+1} \longrightarrow I_{i+2}). \qquad (4.12)$$

This provides a quantity independent of charge carriers which may be compared with experimental data, as well as data obtained from previous theoretical methodologies. The previous methodology tested here is outlined in Chapter 1. The changes in free energy for the two catalytic steps investigated here are summarised in Table 4.2, as are the resulting values for Δ(ΔG). For the CSA methodology Δ(ΔG) = (-0.5 ± 1.3) eV, although this is in very good agreement with experiment (see Table 4.2), there is a very large standard deviation. This is primarily due to the method of calculating ΔE_{e^-}. Because of the fluctuations in KS energy during the simulations, longer simulation time or a larger box size with more water molecules would be needed to decrease the standard deviation.

Initially it was proposed that the energetic contribution due to the electron acceptor should be kept constant throughout the catalytic cycle. This contribution includes not only the redox potential, it also accounts for the solvated proton. The changes in free energy for each step as calculated with the CSA were therefore compared to experimental and static theoretical values (see Table 4.2). Considering the static calculations, the Δ(ΔG) deviates only 0.01 eV when compared to the CSA, where the static calculations were calculated using a different functional: B3LYP vs OPBE for the CSA. Furthermore, there is a deviation of 0.1 eV between Δ(ΔG) when comparing the CSA to experimental values. It may therefore be concluded that the initial proposition does indeed

Table 4.2 Summary of the changes in free energy ΔG, in eV, for the first two PCET steps of the catalyst *Ru*-bpy, as obtained by the CSA methodology, experiment (Exp),[21] and static theoretical methods (B3LYP/TZP).[21] Δ(ΔG) is the difference between the ΔG obtained for the first two catalytic steps (top two rows of the table).The differences between CSA and the latter two are also noted: Δ_1 = CSA - Exp and Δ_2 = CSA - B3LYP/TZP.

	CSA	**Exp**	**Δ_1**	**B3LYP/TZP**	**Δ_2**
$\Delta G([Ru\text{-}OH_2]^{2+} \rightarrow [Ru\text{-}OH]^{2+})$	1.6	0.67	**0.93**	0.87	**0.73**
$\Delta G([Ru\text{-}OH]^{2+} \rightarrow [Ru{=}O]^{2+})$	2.1	1.27	**0.83**	1.38	**0.72**
Δ(ΔG)	-0.5	-0.60	**0.1**	-0.51	**0.01**

hold. Future calculations can then use the (0.88 ± 0.05) eV constant to account for the use of the CSA with a Mn ion.

4.4. Conclusions

The energetics of the first two steps of a water oxidation catalytic cycle were examined using a closed system approach in which an electron acceptor is included in a fully solvated simulation setup. This set up allows for the examination of the energetic contribution of electron transfer, as well as the energetics and process of proton transfer. In both the steps examined, proton transfer was thermodynamically favourable after electron transfer: proton transfer was an energy activated reaction during the first catalytic step, and barrier-less for the second. The closed system approach compares well with experiment, within 0.1 eV, though a large standard deviation results from the statistical uncertainty of the electron transfer energies. Mechanistically, it was observed that a viable water wire is essential for proton release into the solvent, which further emphasises the importance of considering the environmental influence on a catalytic reaction.

4.5. References

[1] D. E. Polyansky *et al. J. Am. Chem. Soc.* **2011**, *133* (37), 14649–14665.
[2] J. D. Blakemore *et al. J. Am. Chem. Soc.* **2010**, *132* (45), 16017–16029.
[3] T. Wang *et al. J. Chem. Theory Comput.* **2010**, *6* (8), 2395–2401.
[4] M. D. Kärkäs *et al. Angew. Chem. Int. Ed.* **2012**, *51* (46), 11589–11593.
[5] A. Venturini *et al. Chem. – Eur. J.* **2014**, *20* (18), 5358–5368.
[6] M. Orio *et al. Photosynth. Res.* **2009**, *102* (2), 443–453.
[7] H. A. Younus *et al. ChemSusChem* **2017**, *10* (5), 862–875.
[8] S. Hammes-Schiffer. *Acc. Chem. Res.* **2017**, *50* (3), 561–566.
[9] T. Zhang *et al. J. Am. Chem. Soc.* **2014**, *136* (1), 273–281.
[10] A. V. Marenich *et al. Angew. Chem. Int. Ed.* **2012**, *51* (51), 12810–12814.
[11] J. J. Concepcion *et al. J. Am. Chem. Soc.* **2008**, *130* (49), 16462–16463.
[12] R.-Z. Liao and P. E. M. Siegbahn. *ChemSusChem* **2017**, *10* (22), 4236–4263.
[13] M. D. Tissandier *et al. J. Phys. Chem. A* **1998**, *102* (40), 7787–7794.
[14] J. K. Nørskov *et al. J. Phys. Chem. B* **2004**, *108* (46), 17886–17892.
[15] J. Rossmeisl *et al. Chem. Phys.* **2005**, *319* (1–3), 178–184.
[16] S. Nachimuthu *et al. Chem. Phys.* **2012**, *400*, 8–12.
[17] M. Tuckerman *et al. J. Chem. Phys.* **1995**, *103* (1), 150–161.
[18] R. Biswas and G. A. Voth. *J. Chem. Sci.* **2017**, *129* (7), 1045–1051.
[19] N. Agmon *et al. Chem. Rev.* **2016**, *116* (13), 7642–7672.
[20] R. A. Marcus. *Rev. Mod. Phys.* **1993**, *65* (3), 599–610.
[21] J. M. de Ruiter *et al. ACS Catal.* **2016**, *6* (11), 7340–7349.
[22] *CPMD*; Copyright IBM Corp 1990-2008, Copyright MPI für Festkörperforschung Stuttgart 1997-2001.
[23] "Accelrys Software Inc." *Discovery Studio Modeling Environment*; Accelrys Software Inc., San Diego: San Diego, 2012.
[24] B. R. Brooks *et al. J. Comput. Chem.* **1983**, *4* (2), 187–217.
[25] C. Hartwigsen *et al. Phys. Rev. B* **1998**, *58* (7), 3641–3662.
[26] I.-C. Lin *et al. Phys. Rev. B* **2007**, *75* (20), 205131.
[27] M. Swart *et al. Molecular Physics* **2004**, *102* (23-24), 2467–2474.
[28] W. Humphrey *et al. J. Mol. Graph.* **1996**, *14* (1), 33–38.
[29] *VMD - Visual Molecular Dynamics*; Theoretical Chemistry and Computational Biophysics Group, University of Illinois, Urbana, U.S.A, 2012.
[30] H. Akima. *J. ACM* **1970**, *17* (4), 589–602.
[31] L. Bernasconi *et al. ACS Catal.* **2017**, *7* (6), 4018–4025.

[32] B. Ensing *et al. J. Phys. Chem. A* **2001**, *105* (13), 3300–3310.
[33] M. Sprik. *Faraday Discuss.* **1998**, *110* (0), 437–445.
[34] K. S. Yamaguchi and D. T. Sawyer. *Isr. J. Chem.* **1985**, *25* (2), 164–176.
[35] A. Monti *et al. J. Phys. Chem. C* **2016**, *120* (40), 23074–23082.
[36] A. Hassanali *et al. Proc. Natl. Acad. Sci.* **2013**, *110* (34), 13723–13728.

4.A. Appendix

4.A.1. CSA with an electron acceptor in a constrained environment

Here we outline a treatment of Mn ion that will serve throughout the simulations to establish the stable electron acceptor Mn^{3+}/Mn^{2+}. We do this first by examining the system where no constraint is placed upon the Mn ion environment. The different solvation environments observed are shown in Figure A4.1.

Figure A4.1 The different solvation environments observed around the Mn ion when the environment is not constrained.

Simulations are performed on the catalytic intermediate $[Ru^{II}\text{-}OH_2]^{2+}$ and an Mn ion within a 17.52 × 15.78 × 13.65 $Å^3$ box with 94 water molecules, total charge 5^+. Two cases are examined:

1. The system was allowed to equilibrate and evolve as $[Ru^{II}\text{-}OH_2]^{2+} + Mn^{3+}$ for 1 ps.
    a. The relevant constraint distance was contracted from 1.6 Å.
    b. The multiplicity was flipped to $[Ru^{III}\text{-}OH_2]^{3+} + Mn^{2+}$, and the constraint distance contracted from 1.6 Å.
2. The system was allowed to equilibrate and evolve as $[Ru^{III}\text{-}OH_2]^{3+} + Mn^{2+}$ for 1 ps. The relevant constraint distance was then contracted from 1.4 Å.

During the initial equilibration and evolution of the unconstrained $[Ru^{II}\text{-}OH_2]^{2+} + Mn^{3+}$, it was observed that there was a significant amount of activity around the Mn ion. The Mn^{3+} ion spontaneously reacted with the surrounding water molecules to form a $Mn(OH)_3$ complex (see Figure A4.1), releasing three H^+ ions into solution. Flipping the multiplicity of the system after the formation of this $Mn(OH)_3$ complex to form $[Ru^{III}\text{-}OH_2]^{3+} + Mn^{2+}$ did not lead to significant changes in the Mn solvation environment, leaving the $Mn(OH)_3$ complex intact. Comparatively, there is no such reaction during the initial equilibration and

evolution of the unconstrained $[Ru^{III}\text{-}OH_2]^{3+}$+ Mn^{2+} system. Instead the solvation shell rearranges spontaneously to form a four-coordinate complex $Mn(H_2O)_4$ (shown in Figure A4.1).

The Mn ion had been introduced as an electron acceptor, but does not behave as an innocent bystander. In order to establish an innocent bystander, we constrain the solvation shell of Mn based on the $Mn(H_2O)_4$ structure. The $Mn(H_2O)_4$ structure was seen to be stable for $[Ru^{III}\text{-}OH_2]^{3+}$+ Mn^{2+} throughout all the simulations in which d(O→H) was examined (see Figure A4.2). Throughout the proton dissociation, <λ> is consistently lower for the $Mn^{2+}(H_2O)_4$ + $[Ru^{III}\text{-}OH_2]^{3+}$ system than for both $Mn^{3+}(OH)_3$ + $[Ru^{II}\text{-}OH_2]^{2+}$ and $Mn^{2+}(OH)_3$ + $[Ru^{III}\text{-}OH_2]^{3+}$.

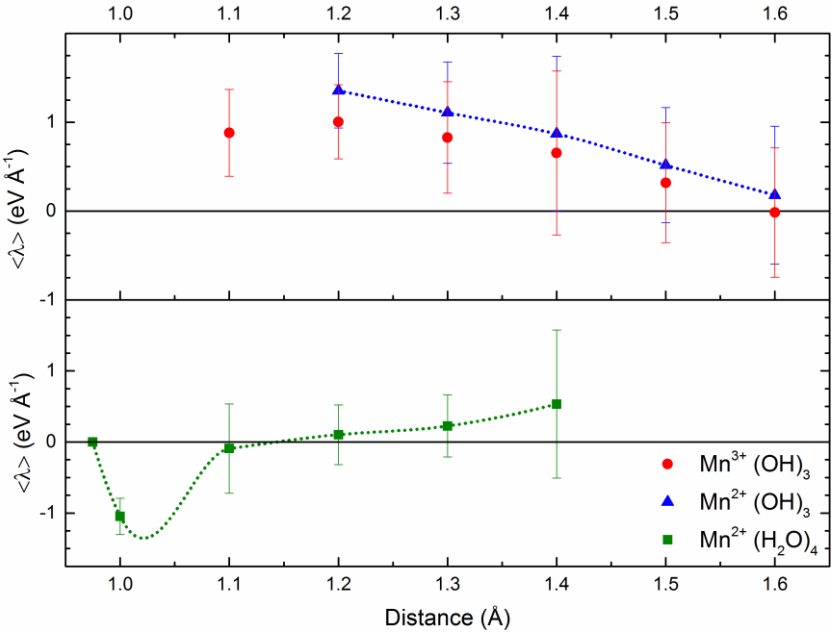

Figure A4.2 The time-averaged constraint force (<λ>) as a function of d(O→H), $[Ru^{III}\text{-}OH_2]^{3+}$ + Mn^{2+} ⇌ $[Ru^{III}\text{-}OH]^{2+}$ + H^+_{solv} + Mn^{2+}, and $[Ru^{II}\text{-}OH_2]^{2+}$ + Mn^{3+} for the $Mn(OH)_3$ and $Mn(H_2O)_4$ solvation environments (see Figure A4.1).

4.A.2. Consideration of the first reaction step proceeding via $[Ru^{II}\text{-}OH]^+$ + H^+_{solv} + Mn^{3+}

As mentioned in Chapter One, one might modify the sequence of proton and electron transfer throughout the water splitting reaction. In the main text we consider the electron first process, analogous to experiment. However, PCET may also proceed via a proton first mechanism. We therefore compare proton dissociation for $[Ru^{II}\text{-}OH_2]^{2+}$ + Mn^{3+} to $[Ru^{III}\text{-}OH_2]^{3+}$ + Mn^{2+}, the latter being mentioned in the main text. The time-averaged constraint force (<λ>) for both systems is shown in Figure A4.3. From d(O→H) = 1.4 Å it is clear that

$[Ru^{II}\text{-}OH_2]^{2+}$ + Mn^{3+} has a consistently higher <λ>. Furthermore, unlike in the case of $[Ru^{III}\text{-}OH_2]^{3+}$ + Mn^{2+} there is no observed transition state: <λ> remains greater than zero. This makes the stability of $[Ru^{II}\text{-}OH]^{+}$ + H^{+}_{solv} + Mn^{3+} unlikely. The instability of $[Ru^{II}\text{-}OH]^{+}$ + H^{+}_{solv} + Mn^{3+} is confirmed after the d(O→H) constraint has been released, as shown in Figure A4.4. Although the solvated proton is partially transferred to the second solvation shell while d(O→H) = 1.0 Å, when the constraint is released the proton returns to the reaction site within 0.4 ps.

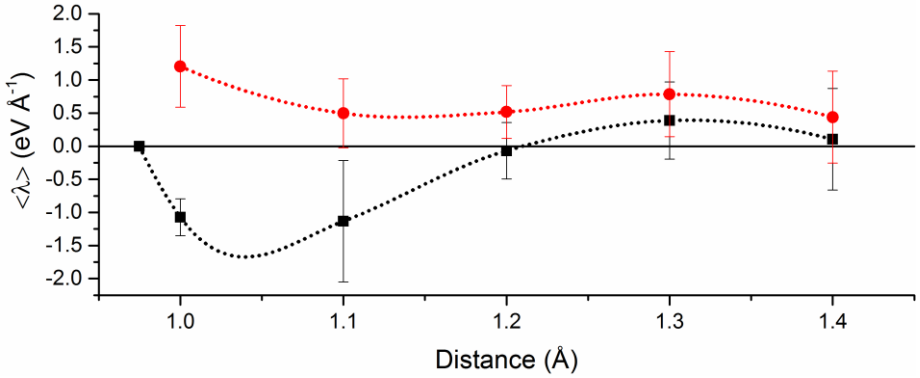

Figure A4.3 The time-averaged constraint force (<λ>) as a function of d(O→H). This analysis is performed for $[Ru^{III}\text{-}OH_2]^{3+}$ + Mn^{2+} ⇌ $[Ru^{III}\text{-}OH]^{2+}$ + H^{+}_{solv} + Mn^{2+} (black) and $[Ru^{II}\text{-}OH_2]^{2+}$ + Mn^{3+} ⇌ $[Ru^{II}\text{-}OH]^{+}$ + H^{+}_{solv} + Mn^{3+} (red). The error bars show standard deviations. The dotted line shows the fit of the calculated points. When the constraint is released for $[Ru^{II}\text{-}OH_2]^{2+}$ + Mn^{3+} ⇌ $[Ru^{II}\text{-}OH]^{+}$ + H^{+}_{solv} + Mn^{3+} after d(O→H) = 1.0 Å, the formed bond is broken and the dissociated proton returns to the catalyst.

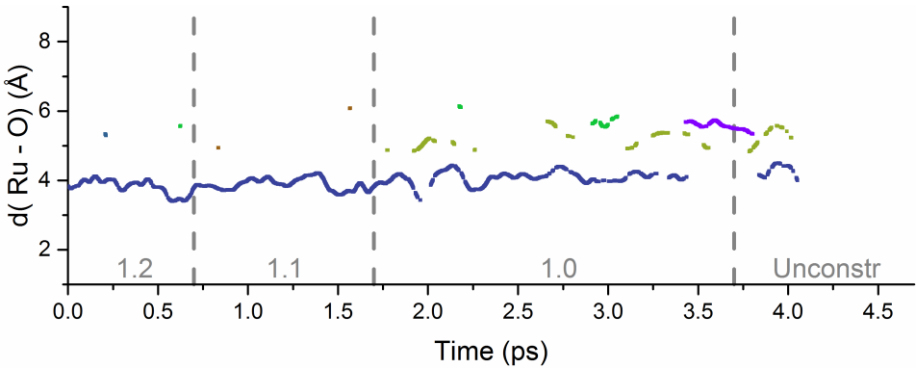

Figure A4.4 The distance between Ru and the H_3O^{+} ion associated with the proton transferred during $[Ru^{II}\text{-}OH_2]^{2+}$ + Mn^{3+} ⇌ $[Ru^{II}\text{-}OH]^{+}$ + H^{+}_{solv} + Mn^{3+}. d(O→H) is noted in grey, and subsequent runs with decreasing d(O→H) are separated by dashed lines. The different oxygens to which the proton associates are monitored by assigning a specific colour trace to each different oxygen. Recombination of the proton is seen at around 4 ps.

4.A.3. Calculation standard deviation ΔG_{H^+}

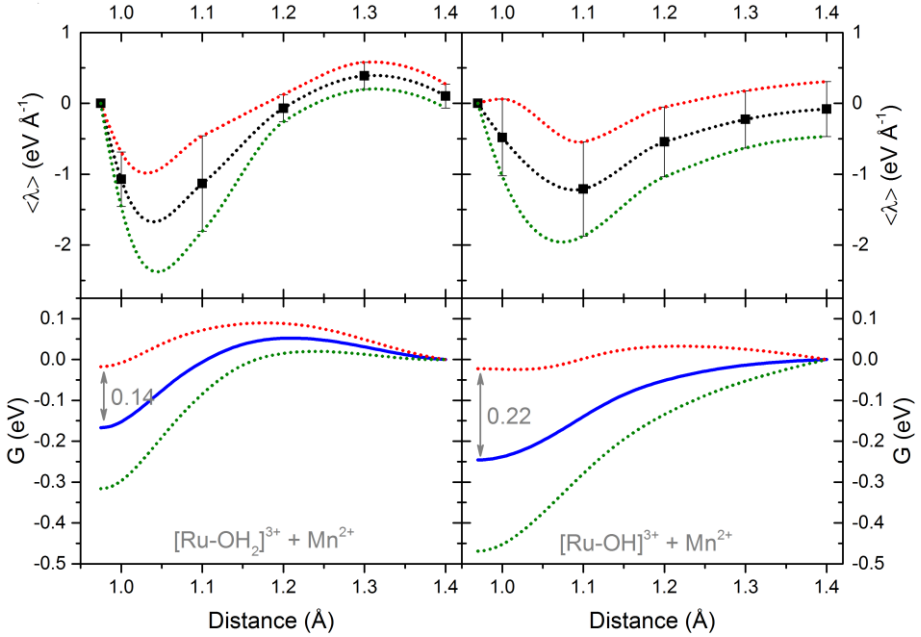

Figure A4.5 Here we reproduce Figure 4.3 (left, $[Ru^{III}\text{-}OH_2]^{3+}$ + Mn^{2+}) and Figure 4.6 (right, $[Ru^{IV}\text{-}OH]^{3+}$ + Mn^{2+}). We have also included the maximum (red) and minimum (green) interpolations of <λ> (top panels), which are then integrated with respect to distance (bottom panels). The standard deviations are noted in grey: 0.14 and 0.22 eV for $[Ru^{III}\text{-}OH_2]^{3+}$ + Mn^{2+} and $[Ru^{IV}\text{-}OH]^{3+}$ + Mn^{2+} respectively.

4.A.4. Radial Distribution Functions Ru – O during proton diffusion

In the case of $[Ru^{III}\text{-}OH_2]^{3+}$ + Mn^{2+} there are three solvation shells visible: around 4 Å, 5 – 7 Å and 7 – 9 Å. This expands on the conclusions reached in Figure 4.4.

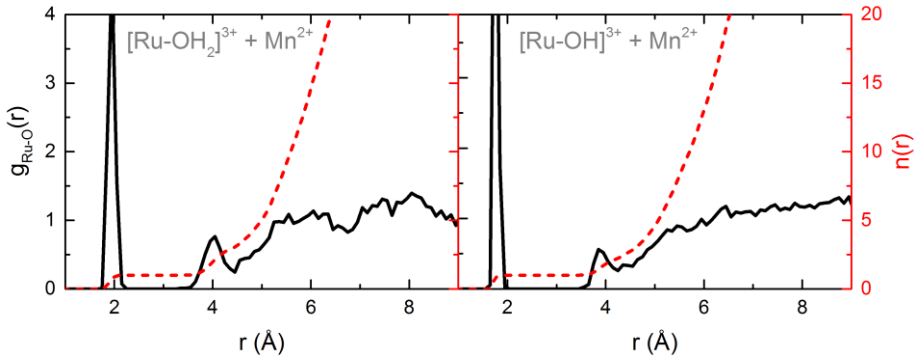

Figure A4.6 The radial distribution functions for the proton diffusion simulations d(O→H) = 1.2 - unconstrained for (left) $[Ru^{III}\text{-}OH_2]^{3+}$ + Mn^{2+}, and (right) $[Ru^{IV}\text{-}OH]^{3+}$ + Mn^{2+}.

In Figure 4.7 the proton released from $[Ru^{IV}\text{-}OH]^{3+}$ was seen to stabilise in the second shell. Only the first solvation shell is well defined, at around 4 Å. The 'second' solvation shell is a broad distribution from 5 Å. This is likely due to the high mobility of the water molecules during this simulation, as demonstrated in Figure 4.7, where the O with three H atoms moves from 4.5 – 6 Å over the course of the simulation. Of further note, here the contraction of the Ru – O distance between $[Ru^{II}\text{-}OH_2]^{2+}$ and $[Ru^{III}\text{-}OH]^{2+}$ can be seen.

4.A.5. <λ> for $[Ru^{III}\text{-}OH]^{2+}$ including initial accelerated contraction

For completeness, <λ> for $[Ru^{III}\text{-}OH]^{2+}$ as d(O→H) was contracted from 2.04 Å, where the initial contraction was more rapid is included here. The more rapid contraction is seen in the larger standard deviation for d(O→H) ≥ 1.5 Å.

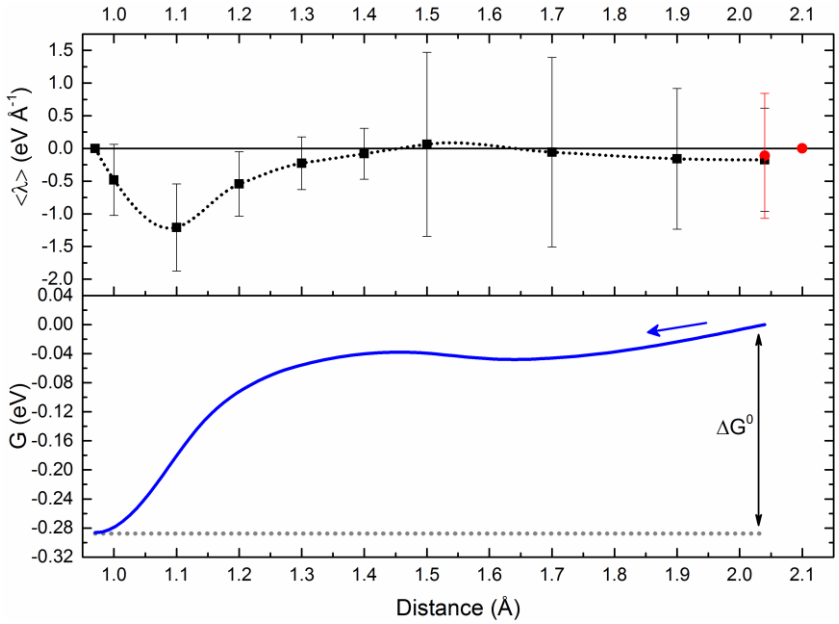

Figure A4.7 (top)The time-averaged constraint force (<λ>) as a function of d(O→H). This analysis is performed for $[Ru^{IV}\text{-}OH]^{3+}$ + Mn^{2+} ⇌ $[Ru^{IV}{=}O]^{2+}$ + H^+_{solv} + Mn^{2+} (black) and initially also for $[Ru^{III}\text{-}OH]^{2+}$ + Mn^{3+} (red). The error bars show standard deviations. The dotted line shows the fit of the calculated points. For d(O→H) ≥ 1.5 Å <λ> remains around zero, as expected. (bottom) the integral of the <λ> fit with respect to distance. The definite integral has a value $\Delta G^0_{H^+}$ = -0.29 eV (-6.7 kcal/mol). For comparison, the integral from 1.4 Å has a value $\Delta G^0_{H^+}$ = -0.25 eV (-5.8 kcal/mol). The difference is slight.

4.A.6. Gaussian fits of KS Energies for ΔE_{e^-}

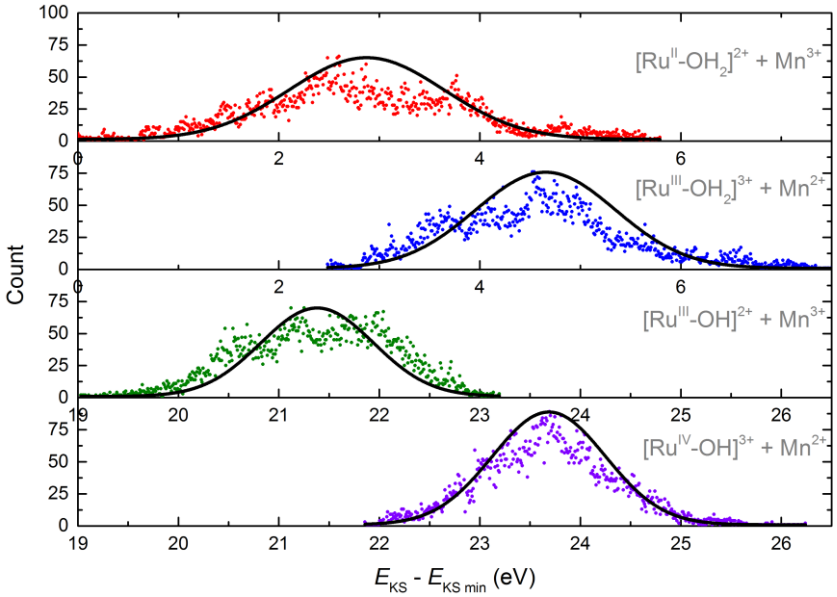

Figure A4.8 Gaussian fits used to determine ΔE_{e^-} and its standard deviation. E_{KS} – $E_{KS\ min}$ is the KS Energy normalised such that the global minimum of all KS energies is 0. The interval size is given by ($E_{KS\ max}$ – $E_{KS\ min}$)/3000, which is equal to 0.009 eV. The KS energy distributions do deviate to some extent from a single Gaussian distribution; in the top panel one could suppose the overlap of two Gaussians. This deviation can be attributed to the fluctuations in the hydrogen bonding network of the solvent, which at this time-scale retains a memory of the initial configuration. In order to get memory-less distribution, the simulation would either have to be repeated with different initial conditions, or extended for a significant amount of time. Nevertheless, the estimated <E_{KS}> should not be effected, especially considering the standard deviation.

Increasing Deprotonation Rate: Tuning the Environment

Chapter Five

5. Increasing the Rate of the Deprotonation Step in a Single-site Water Oxidation Catalyst: Tuning the Environment

Abstract

The solvent environment of the reaction site of a water oxidation catalyst has a significant impact on the catalytic mechanism and performance of the catalyst. The solvent environment is of great importance when considering the proton transfer pathways away from the reaction centre. These proton channels are essential to the catalytic mechanism, yet are often overlooked in theoretical investigations of water oxidation catalysis. Here, insight into the proton diffusion process is obtained by considering the first three catalytic steps for an explicitly solvated water oxidation catalyst, $[Ru(cy)(bpy)(H_2O)]^{2+}$. It is shown that the inclusion of a proton acceptor in the vicinity of the reaction site leads to very rapid proton transfer along the adjacent water wire, as well as a decrease in both the thermodynamic barrier and the overall free energy difference in the O – O bond formation step. These results provide design principles for the assembly of photo-catalytic devices for solar fuel production.

5.1. Introduction

Understanding the mechanism of PCET is one of the foundations of rational catalyst design.[1–3] Alternation of electron and proton transfer prevents high energy intermediates, by avoiding accumulation of charge at the catalyst complex.[3] Computationally, proton transfer is often associated with either high activation barriers,[4] or high changes in free energy.[5] To ameliorate this, a growing amount of research is considering the first and second coordination spheres of a reaction site,[6–8] allowing for targeted proton transfer pathways. An increasingly popular way of modifying these proton pathways is by the use of non-innocent ligands around the catalytic metal centre.[7,9–15] These non-innocent ligands are used to influence proton transfer, usually by including localised proton acceptor functionalities. Additives, including counter ions, bases, and various solvent molecules,[4] can also be used as proton acceptors. These proton acceptors may be used in combination with the embedding of a WOC within a proton exchange membrane.[16]

Some static calculations in implicit solvent have been performed regarding the inclusion of localised proton acceptors.[4,7,11,17,18] However, it is becoming increasingly clear that the inclusion of an explicit solvent is important when considering WOC reactions, and that proton migration away from the catalytic site plays a significant role.[19–21] This has implications for reaction barriers and process rates (see Chapter Four). There has been a substantial amount of research investigating the hydrated proton and its migration mechanism within bulk water.[22–24] However, little has been done in combination with a WOC. The introduction of a WOC introduces different structural constraints than those of bulk water.

Here we specifically examine proton transport from the WOC reaction site to a proton acceptor within dynamically formed water wires surrounding a catalytic centre. To do so, we use the ruthenium based mononuclear molecular WOC $[Ru(cy)(bpy)(H_2O)]^{2+}$ (cy = *p*-cymene, bpy = 2,2'-bipyridine; (*Ru*-bpy)), earlier

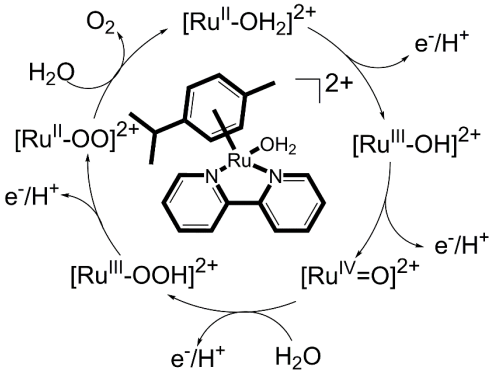

Scheme 5.1 Proposed catalytic cycle for water oxidation by *Ru*-bpy.

examined in Chapters Two and Four (see also Scheme 5.1). Experimentally, the [Ru(cy)(bpy)Cl]Cl salt was activated by exchange of Cl^- by H_2O to give the $[Ru^{II}\text{-}OH_2]^{2+}$ aqua form.[25] This dramatically increases the local proton density and induces catalytic activity. The introduction of an OH^- proton acceptor will further change the proton density. The resulting activity for the first two proton transfer steps $[Ru^{II}\text{-}OH_2]^{2+} + OH^- \rightleftharpoons [Ru^{II}\text{-}OH]^+ + H_2O$ and $[Ru^{III}\text{-}OH]^{2+} + OH^- \rightleftharpoons [Ru^{III}\text{-}O]^+ + H_2O$ is examined, as well as the third step $[Ru^{IV}{=}O]^{2+} + OH^- \rightleftharpoons [Ru^{II}\text{-}OOH]^+$ which includes the crucial O – O bond formation step.

5.2. Computational Method and Details

The CPMD program for AIMD was used to examine the explicitly solvated systems.[26] The water solvent environment for the CPMD simulations was generated using Discovery Studio 2.5.[27] The solvent was equilibrated for 0.2 ns using the CHARMM force field with the TIP3P model for water and CFF partial charge parameters at 300 K,[28,29] while the catalyst was kept fixed. The volume was then adjusted using constant pressure MD for 0.2 ns, after which the system was further allowed to evolve with constant volume for 2 ns. Subsequently CPMD simulations were performed in the canonical NVT ensemble at 300 K, using GTH pseudopotentials for the transition metals,[30] DCACP pseudopotentials for the remaining atoms,[31] and the OPBE exchange-correlation functional.[32] KS orbitals are expanded on a plane wave basis set with an energy cut-off of 70 Ry. A time step of 5 a.u = 0.121 fs was used. Image rendering for the CPMD output was done using VMD.[33,34]

The simulation box

First, the $[Ru^{II}\text{-}OH_2]^{2+}$ intermediate was solvated with 123 water molecules in a cubic box with periodic boundary conditions and sides of 16.63 Å. This box has a total charge of 2^+ and singlet multiplicity. Within the periodic boundary conditions the total charge density is compensated by a neutralizing homogeneous negative charge background.[35] The system was initially allowed to equilibrate and evolve for 0.4 ps. After this simulation the spontaneously formed water wires, or hydrogen bonding network, adjacent to the reaction site was visualised, as shown in Figure 5.1. Proton transport is examined by removing one proton from one of the various water molecules along the water wires connected to the reaction site. This creates $[Ru^{II}\text{-}OH_2]^{2+} + OH^- \rightleftharpoons [Ru^{II}\text{-}OH]^+ + H_2O$ (initially shifted to the left) in a box filled with 122 water molecules, with a total charge of 1^+ and singlet multiplicity. For each of the positions examined, $O_{ii} - O_{vi'}$, as defined in Figure 5.1, the system is allowed to evolve freely for 0.25 ps to examine the proton rearrangement. This is repeated for $[Ru^{III}\text{-}OH]^{2+} + OH^- \rightleftharpoons [Ru^{III}\text{-}O]^+ + H_2O$, where the removal of an electron from the catalyst is accompanied by the extraction of a proton from O_i. This system, with the charge maintained at 1^+, now has doublet multiplicity.

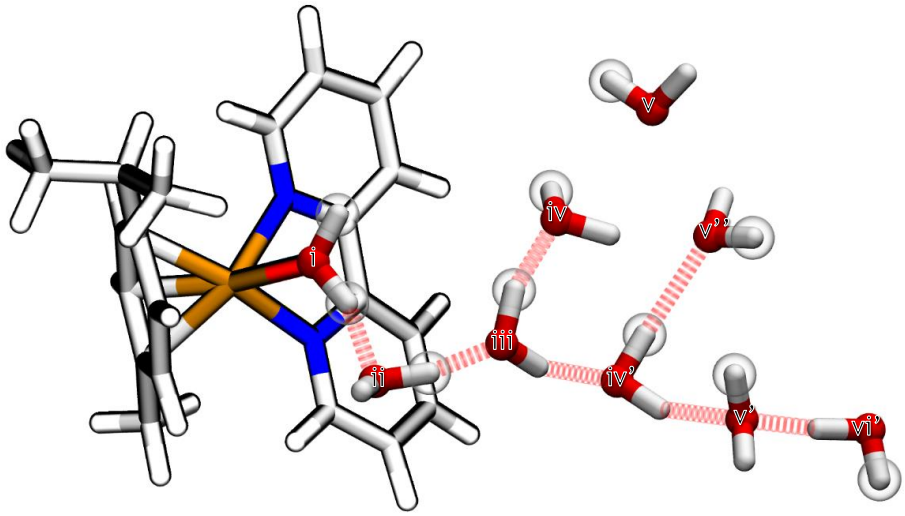

Figure 5.1 The solvated *Ru*-bpy catalyst showing the hydrogen bonding chain branching from the reaction site. Roman numerals indicate the subscripts used to refer to the O atoms in the chains. H bonds are also indicated (cut-off angle 30°, distance 3.5 Å as per Biswath and Voth).[24] The H^+ removed at the start of the simulation are circled.

O - O bond formation investigated using constrained MD

The same MD box was used to examine the dynamics of the $[Ru^{IV}{=}O]^{2+} + OH^- \rightleftharpoons [Ru^{II}\text{-}OOH]^+$ step and the effect of the OH^- ion on the barrier height of O – O bond formation. First, $[Ru^{IV}{=}O]^{2+} + H_2O$ was generated from the initial $[Ru^{II}\text{-}OH_2]^{2+}$ system by removing the two hydrogen atoms from the ligated O_i. While maintaining a total charge of 2+, a triplet multiplicity is imposed, following previous studies indicating the triplet state is most stable for the $[Ru^{IV}{=}O]^{2+}$ intermediate.[25] Subsequently, O – O bond formation was examined by progressively shortening the constraint distance d(O→O) between the oxygen atom of a solvent water molecule and the oxo ligand (see Figure 5.2).

The system is allowed to evolve for at least 0.25 ps to allow the time-averaged constraint force $\langle\lambda\rangle_x$ to stabilise. In cases where large fluctuations in $\langle\lambda\rangle_x$ were still observed after this time, the simulation length was extended to a maximum of 1 ps. After d(O→O) was contracted to 1.4 Å, close to the O – O bond length

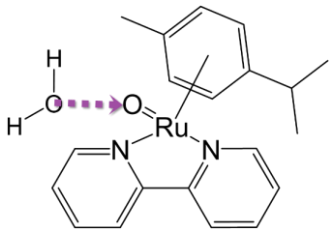

Figure 5.2 The distance constraint d(O→O), shown in purple, considered in this chapter for the catalytic intermediate $[Ru^{IV}{=}O]^{2+}$.

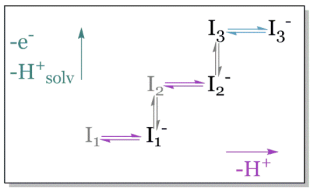

$$[Ru^{IV}{=}O]^{2+} + OH^- \rightleftharpoons [Ru^{II}\text{-}OOH]^+$$

$$[Ru^{III}\text{-}OH]^{2+} + OH^- \rightleftharpoons [Ru^{III}\text{-}O]^+ + H_2O$$

$$[Ru^{II}\text{-}OH_2]^{2+} + OH^- \rightleftharpoons [Ru^{II}\text{-}OH]^+ + H_2O$$

Scheme 5.2 The catalytic steps examined in this work. Vertical lines denote electron transfer, as well as the extraction of a solvent proton from the surrounding water wire; horizontal lines proton transfer at the catalytic intermediates, which for the third step includes a nearby H_2O/OH^-. Stable intermediates are shown in black, unstable intermediates in grey. The inset shows the corresponding generalised intermediates following the same notation introduced in Chapter 1 (see Figure 1.2)

obtained from geometry optimisation (see Chapter Two), the constraint was removed and the system was allowed to evolve freely. Next, the effect of including a proton acceptor within viable water wires is examined by comparing bond formation while the water wire contains only water molecules, i.e. $[Ru^{IV}{=}O]^{2+} + H_2O \rightleftharpoons [Ru^{II}\text{-}OOH]^+ + H^+_{solv}$, to bond formation when one of the closest water molecules, O_{iii}, has been deprotonated, i.e. $[Ru^{IV}{=}O]^{2+} + OH^- \rightleftharpoons [Ru^{II}\text{-}OOH]^+$ with a total charge of 1^+. The whole procedure was repeated for $[Ru^{IV}{=}O]^{2+} + H_2O$ and $[Ru^{IV}{=}O]^{2+} + OH^-$, starting from the same initial conditions, but imposing a singlet multiplicity.

5.3. Results and Discussion

While the simulation box is kept at a charge 1^+, the effect of a proton acceptor within the explicit solvent environment on the first two proton transfer steps, and O – O bond formation, of the ruthenium-based WOC (as shown in Scheme 5.2) was investigated. The first two steps, $[Ru^{II}\text{-}OH_2]^{2+} + OH^- \rightleftharpoons [Ru^{II}\text{-}OH]^+ + H_2O$ and $[Ru^{III}\text{-}OH]^{2+} + OH^- \rightleftharpoons [Ru^{III}\text{-}O]^+ + H_2O$, are used to examine proton transport. For the O – O bond formation step, constrained CPMD was performed for $[Ru^{IV}{=}O]^{2+} + H_2O \rightleftharpoons [Ru^{II}\text{-}OOH]^+ + H^+_{solv}$ which is then compared to the $[Ru^{IV}{=}O]^{2+} + OH^- \rightleftharpoons [Ru^{II}\text{-}OOH]^+$ case. This comparison can be used to determine the effect of a proton acceptor in the surrounding solvent on the most thermodynamically challenging step of this catalytic cycle.[25]

5.3.1. Proton Transport

Proton transport was investigated by examining the relative positions of proton holes in the solvation environment surrounding the catalytic centre. The proton holes effectively create hydroxide ions within the water wire, and it is the relative positions of these hydroxide ions that were monitored during the simulations. It

should be acknowledged that there has been some discussion as to the nature of OH^- propagation,[36,37] specifically that it should not be considered the inverse of proton transfer due to the resting state of OH^- being a hypercoordinated species $OH^-(H_2O)_4$.[38] In this work however, proton holes are generated within water wires which have already been formed, and on the short time scale of the simulations performed here (0.25 ps) it is highly unlikely that the fourth water molecule will complete the $OH^-(H_2O)_4$ structure before a proton has been further transferred down the wire.

The initial position of the OH^- ion corresponds to a water molecule from which one proton is removed. This water molecule is chosen freely from within one of the water wires adjacent to the catalytic centre (Figure 5.1). OH^- migration is first examined for the $[Ru^{II}\text{-}OH_2]^{2+} + OH^- \rightleftharpoons [Ru^{II}\text{-}OH]^+ + H_2O$ process. The diffusion of the OH^- ion in the vicinity of $[Ru^{II}\text{-}OH_2]^{2+}$ is monitored by plotting the distance between the ruthenium centre and OH^- ions in solution (as shown in Figure 5.3), where an OH^- ion is defined as an oxygen with only one proton within a distance of 1.2 Å. If a proton is within 1.2 Å of an O atom, it can be considered bonded.[19]

Consider first the case where a proton is removed from the water molecule closest to the reaction centre (O_{ii} in Figure 5.1). As a result, the OH^- ion is initially located

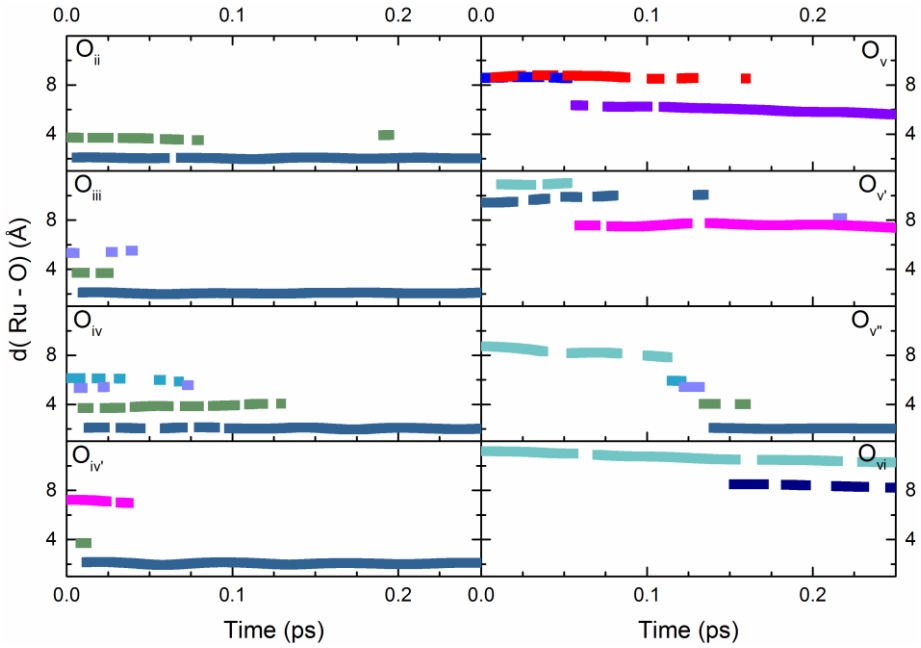

Figure 5.3 The distance between Ru and OH^-, defined as an oxygen atom which has only one H atom within a radius of 1.2 Å for $[Ru^{II}\text{-}OH_2]^{2+} + OH^- \rightleftharpoons [Ru^{II}\text{-}OH]^+ + H_2O$. The initial distance depends on which water molecule in the vicinity of the reaction site has been deprotonated to mimic the presence of a OH^- ion (for the O label see Figure 5.1). The different oxygen sites at which the OH^- ion is located are monitored by assigning a specific colour trace to each different oxygen.

at 4 Å from Ru on an oxygen with a green trace (O_{ii}, Figure 5.3, top left). In this case, a proton transfer attempt occurs from the H_2O ligated to the Ru catalytic centre almost immediately. This results in OH^- migration from an oxygen in the first solvation shell (green trace) to the O ligated to the catalytic centre (dark blue trace). At 0.1 ps the proton transfer is completed and the catalyst has been deprotonated to form $[Ru^{II}\text{-}OH]^+$: the Ru – OH distance is then around 2 Å.

For the case where the proton has been removed from O_{iii}, we see that OH^- is originally at around 5.5 Å from the Ru centre (O_{iii}, Figure 5.3, purple trace). Also in this case a proton is rapidly transferred to form an OH^- at around 4 Å (green). This is quickly followed by a further transfer to the catalytic site where it remains stable for the whole simulation at ≈2 Å (again, dark blue). For the O_{iv} case, the OH^- is originally around 6 Å away from the Ru centre (blue). It then propagates via two other water molecules (purple, then green) before reaching the catalytic site after around 150 fs. $O_{iv'}$ behaves similarly to $O_{iii.}$ In contrast, O_v is initially 8 Å away from the Ru centre (blue), after which the OH^- quickly migrates to another site in the same solvation shell (red). From there it migrates to a site at around 6 Å from the Ru centre (purple), but no further proton transfer is observed within the simulation time frame examined here. This is the case for most of the water molecules in the same solvation shell at distances ≥ 8 Å (O_v – O_{vi}).

It may be concluded that if the OH^- ion is within ≈8 Å of the Ru centre, connected to the ligated water molecule through 3 hydrogen bonds (Figure 5.1), the proton transfer along the water wire can be completed within 150 fs. In other words, proton transfer along a water wire consisting of 4 water molecules occurs very rapidly. This also suggests that when considering proton diffusion, a proton would need a water chain of at least 8 Å.

The procedure is repeated for the $[Ru^{III}\text{-}OH]^{2+} + OH^- \rightleftharpoons [Ru^{III}\text{-}O]^+ + H_2O$ step, as shown in Figure 5.4. If an OH^- ion is placed in the first solvation shell at about 4 Å (O_{ii}, Figure 5.4, brown), the OH ligated to Ru at 2 Å (blue) transfers its proton very rapidly to form a water molecule with the OH^- in the solvent. This is confirmed by the emergence of the deprotonated $[Ru^{III}\text{-}O]^+$ species after 180 fs; $[Ru^{III}\text{-}O]^+$ is stable for the remaining time of the simulation. If the OH^- ion is in the second – fourth solvation shells, it does propagate towards the metal centre but does not accept a proton from the catalyst within the 250 fs examined here. However, for the OH^- located at O_{iii}, a longer simulation was performed during which recombination was seen after 300 fs. In Chapter Four it was observed that proton dissociation was spontaneous for $[Ru^{III}\text{-}OH]^{2+} + H_2O$ (i.e. total charge 2^+) after an electron had been transferred from the catalyst to form $[Ru^{IV}\text{-}OH]^{3+} + H_2O \rightleftharpoons [Ru^{IV}{=}O]^{2+} + H^+_{solv} + H_2O$. Comparatively, $[Ru^{III}\text{-}OH]^{2+} + OH^-$ spontaneously undergoes proton transfer to form $[Ru^{III}\text{-}O]^+ + H_2O$ without electron removal. This convincingly demonstrates that a proton acceptor can have a dominant role.

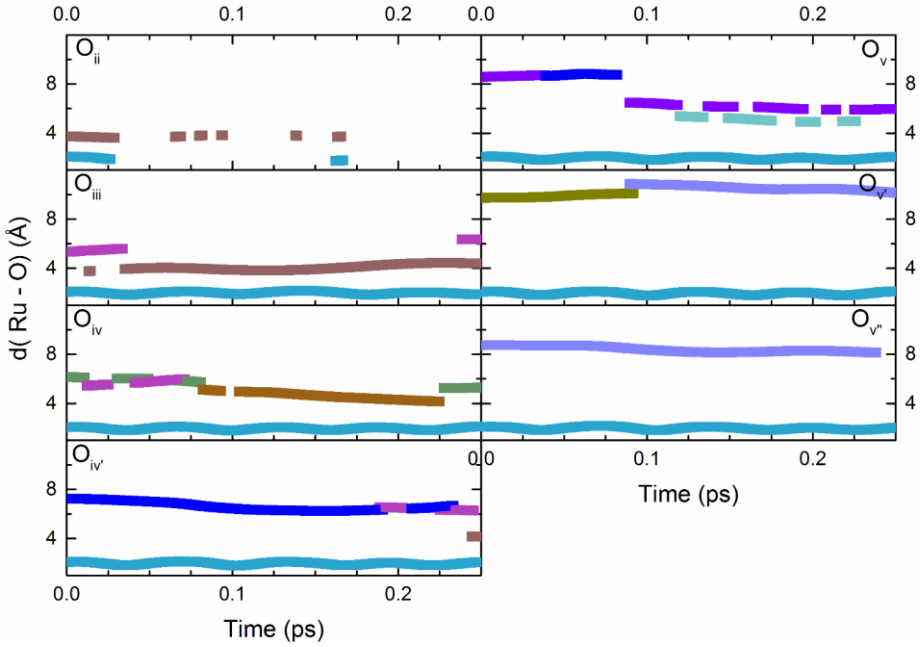

Figure 5.4 The distance between Ru and OH^-, defined as an oxygen atom which has only one H atom within a radius of 1.2 Å for $[Ru^{II}\text{-}OH]^{2+}$ + OH^- ⇌ $[Ru^{II}\text{-}O]^+$ + H_2O. The ligated OH is also monitored (blue trace at 2 Å). The initial distance depends on which water molecule in the vicinity of the reaction site has been deprotonated to mimic the presence of a OH^- ion (for the O label see Figure 5.1). The different oxygen sites at which the OH^- ion is located are monitored by assigning a specific colour trace to each different oxygen.

5.3.2. O – O bond formation via nucleophilic attack on $[Ru^{IV}=O]^{2+}$: proton transfer coupled with multiplicity interchange

For the *Ru*-bpy catalytic system O – O bond formation is the most thermodynamically demanding step, as discussed in Chapter Two. The formation of an O – O bond between the ligated O and a solvent water molecule, and the influence of an adjacent water wire containing OH^-, is examined below using constrained dynamics. The O – O bonding step of a similar ruthenium based WOC $[Ru(benzene)(bpy)]^{2+}$, where the cymene group was substituted for benzene, had been investigated previously.[20] Based on static calculations for $[Ru(benzene)(bpy)]^{2+}$ with only two explicit solvent water molecules, it was inferred that a spin-crossover occurs during the reaction. Here an in-depth investigation of the reaction $[Ru^{IV}=O]^{2+}$ + H_2O ⇌ $[Ru^{II}\text{-}OOH]^+$ + H^+_{solv} in a fully solvated system is presented.

The electron spin density of the $[Ru^{IV}=O]^{2+}$ and $[Ru^{II}\text{-}OOH]^+$ intermediates with both triplet ($^3[Ru^{IV}=O]^{2+}$) and singlet ($^1[Ru^{IV}=O]^{2+}$) multiplicity is shown in Figure 5.5. The $[Ru^{II}\text{-}OOH]^+$ intermediates were obtained by constrained CPMD along d(O→O) shown in Figure 5.2. For $^3[Ru^{IV}=O]^{2+}$ (Figure 5.5, a), delocalisation

of spin density is already observed on the incoming water molecule. After the O – O bond has been formed (Figure 5.5, b), the spin density delocalises over the system, including bpy ligand. In the case of $^1[Ru^{IV}=O]^{2+}$ two anti-parallel spins occupy orbitals which are localised on the Ru centre and oxo group (Figure 5.5, c). These two half occupied orbitals with anti-parallel spins are then able to each receive half of the same electron pair from the incoming water molecule. After the O – O bond has formed (Figure 5.5, d), no spin density is observed. It may therefore also be postulated that O – O bond formation should proceed better in the singlet state than in the triplet state of the $[Ru^{IV}=O]^{2+}$ intermediate.

Spin intersystem crossing during the reaction may also be concluded when considering the change in the time-averaged KS energies for $[Ru^{IV}=O]^{2+} + H_2O \rightleftharpoons [Ru^{II}\text{-}OOH]^+ + H^+_{solv}$ (top line in Table 5.1). For $[Ru^{IV}=O]^{2+}$ the triplet state is more stable by 6.9 eV, while for the $[Ru^{II}\text{-}OOH]^+$ the singlet state is more stable by 2.8 eV. The change in KS energy for $^3[Ru^{IV}=O]^{2+} + H_2O \rightleftharpoons {}^1[Ru^{II}\text{-}OOH]^+ + H^+_{solv}$ is around 1.6 eV.

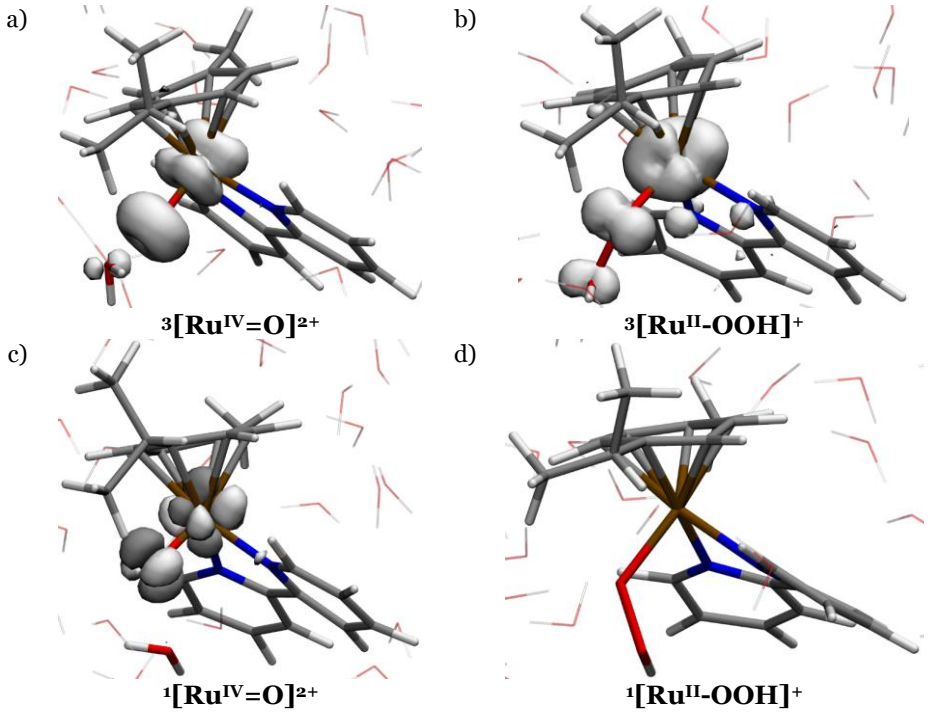

Figure 5.5 Spin density on the catalyst for $[Ru^{IV}=O]^{2+} + H_2O \rightleftharpoons [Ru^{II}\text{-}OOH]^+ + H^+_{solv}$ with different multiplicities, where the isosurfaces with opposite signs are shown in light and dark grey respectively: a) $^3[Ru^{IV}=O]^{2+}$; b) $^3[Ru^{II}\text{-}OOH]^+$; c) $^1[Ru^{IV}=O]^{2+}$; d) $^1[Ru^{II}\text{-}OOH]^+$. $[Ru^{IV}=O]^{2+}$ in both (a) and (c) is obtained during the d(O→O) = 2.4 Å constrained CPMD simulation and $[Ru^{II}\text{-}OOH]^+$, (b) and (d), when d(O→O) = 1.5 Å.

Table 5.1 The difference in the time-averaged KS energy $\langle E_{KS} \rangle$ between the triplet and singlet states as calculated for the reactant and product of the $[Ru^{IV}=O]^{2+} \rightleftharpoons [Ru^{II}\text{-}OOH]^{+}$ reaction, where the former is obtained during the d(O→O) = 2.4 Å simulation, and the latter at d(O→O) = 1.5 Å.

	$\langle E_{KS} \rangle_{singlet} - \langle E_{KS} \rangle_{triplet}$ (eV)	
	$[Ru^{IV}=O]^{2+}$	$[Ru^{II}\text{-}OOH]^{+}$
$[Ru^{IV}=O]^{2+} + H_2O \rightleftharpoons [Ru^{II}\text{-}OOH]^{+} + H^{+}_{solv}$	6.9	-2.8
$[Ru^{IV}=O]^{2+} + OH^{-} \rightleftharpoons [Ru^{II}\text{-}OOH]^{+}$	5.5	-1.6

The time-averaged constraint force <λ> is examined for $[Ru^{IV}=O]^{2+} + H_2O \rightleftharpoons [Ru^{II}\text{-}OOH]^{+} + H^{+}_{solv}$ as d(O→O) is contracted from 2.4 Å (see black line, Figure 5.6, top left). Although when examining $^3[Ru^{IV}=O]^{2+} + H_2O$ for 2.4 ≥ d(O→O) ≥ 1.6 Å one might initially assume that the O – O bond will not form due to the high forces present, a late transition state appears around 1.5 Å. For the $[Ru(benzene)(bpy)]^{2+}$ WOC vibrational analysis was performed in implicit solvent which indicated that the transition state around 1.5 Å was associated to proton transfer from the constrained water molecule to the solvent.[20] In the same study,[20] metadynamics simulations were performed for the O – O bonding step which showed proton transfer from the catalyst at around d(O→O) = 1.5 Å. This

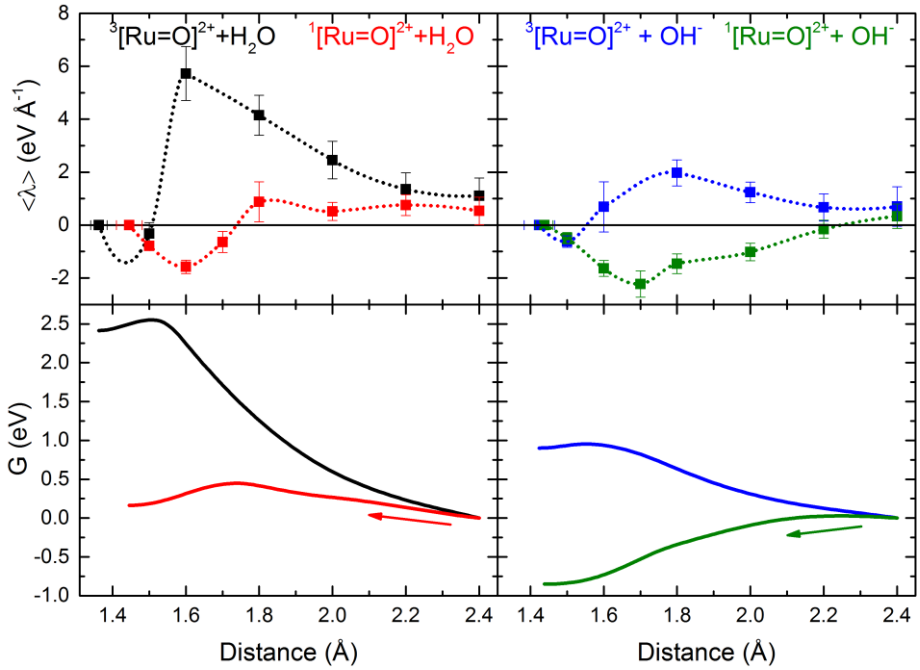

Figure 5.6 (top) The time-averaged constraint force (<λ>) as a function of d(O→O). This analysis is performed for (left) $[Ru^{IV}=O]^{2+} + H_2O \rightleftharpoons [Ru^{II}\text{-}OOH]^{+} + H^{+}_{solv}$ and (right) $[Ru^{IV}=O]^{2+} + OH^{-} \rightleftharpoons [Ru^{II}\text{-}OOH]^{+}$ with both triplet and singlet multiplicity. The error bars show standard deviations and the dotted line shows the fit of the calculated points. The integral of the <λ> fit with respect to distance is shown in the bottom panels. Definite integrals ΔG^0_{O-O} are shown in Table 5.2.

Table 5.2 ΔG^{0}_{O-O} and ΔG^{*}_{O-O} for the $[Ru^{IV}=O]^{2+}$ + H_2O and $[Ru^{IV}=O]^{2+}$ + OH^- systems with both triplet (t) and singlet (s) multiplicity.

	ΔG^{0}_{O-O} (eV)	ΔG^{*}_{O-O} (eV)
$^3[Ru^{IV}=O]^{2+}$ + H_2O	2.41	2.55
$^1[Ru^{IV}=O]^{2+}$ + H_2O	0.16	0.45
$^3[Ru^{IV}=O]^{2+}$ + OH^-	0.90	0.95
$^1[Ru^{IV}=O]^{2+}$ + OH^-	-0.85	0.03

is consistent with the simulation performed here for $^3[Ru^{IV}=O]^{2+}$ + H_2O (see Figure 5.7, top).

It is immediately obvious that <λ> is drastically reduced when the spin is flipped to $^1[Ru^{IV}=O]^{2+}$ + H_2O (red line in Figure 5.6, top left). This supports the conclusion drawn from Figure 5.5 (c and d). A transition state is observed at around d(O→O) = 1.75 Å, which is earlier than in the triplet case. Furthermore, the first proton transfer attempt from $^1[Ru^{IV}=O]^{2+}$ + H_2O also occurs earlier, during the d(O→O) = 1.7 Å simulation (see Figure 5.7, bottom). In Figure 5.6, bottom left, the free energy profile for the singlet state (red line) shows a lower

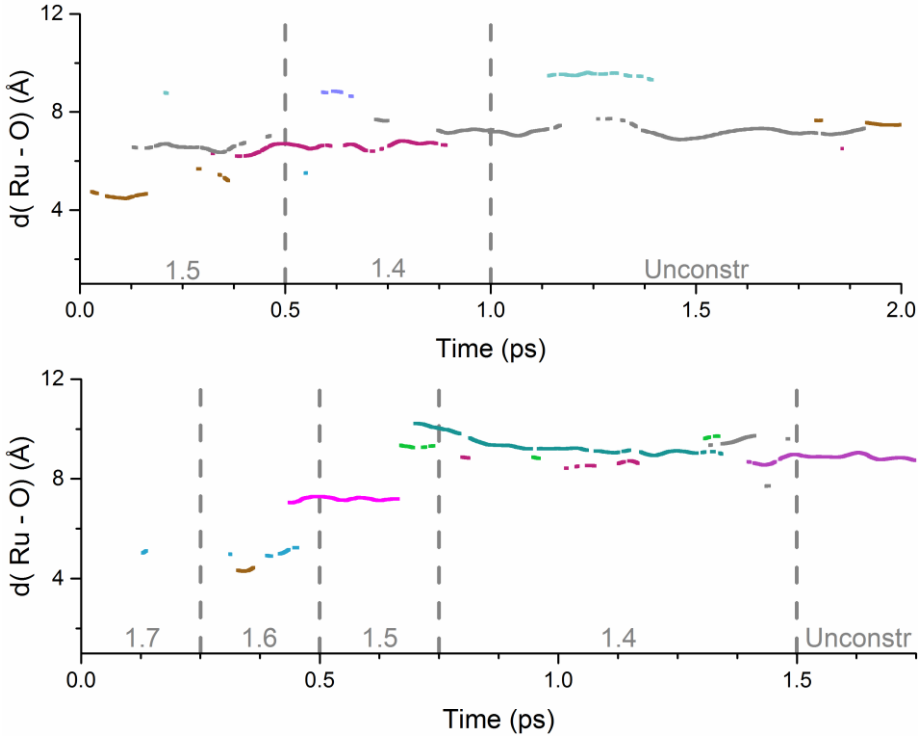

Figure 5.7 The distance between Ru and the H_3O^+ ion associated with the proton solvated during (top) $^3[Ru^{IV}=O]^{2+}$ + H_2O ⇌ $^3[Ru^{II}\text{-}OOH]^+$ + H^+_{solv}, and (bottom) $^1[Ru^{IV}=O]^{2+}$ + H_2O ⇌ $^1[Ru^{II}\text{-}OOH]^+$ + H^+_{solv}. d(O→O) is noted in grey, and subsequent runs with decreasing d(O→O) are separated by dashed lines. The different oxygens to which the additional proton associates are monitored by assigning a specific colour trace to each oxygen.

barrier than for the triplet (see also Table 5.2). It may therefore be concluded that the high barrier and late transition state for $^{3}[Ru^{IV}{=}O]^{2+}$ result from an unfavourable parallel electron spin alignment. In previous experimental work, it was concluded that a strong correlation existed between the control of the electron spin alignment and overpotential.[39] This is supported by the findings here, though here the energetically favoured mechanism proceeds by anti-parallel spin alignment as opposed to parallel spin alignment. This is likely due to the two different mechanisms for O – O bond formation, here the bond is formed by nucleophilic attack while the anti-parallel spin alignment was examined via a radical coupling mechanism.[39]

When a proton acceptor is added within the water wires surrounding the catalytic centre, i.e. for $[Ru^{IV}{=}O]^{2+} + OH^{-} \rightleftharpoons [Ru^{II}\text{-}OOH]^{+}$, a spin-intersystem crossing would also be expected (Table 5.1). For $^{3}[Ru^{IV}{=}O]^{2+} + OH^{-} \rightleftharpoons {}^{1}[Ru^{II}\text{-}OOH]^{+}$ the change in KS energy is around 0.9 eV. Furthermore, as d(O→O) is contracted for both triplet and singlet multiplicities <λ> is significantly lower than in the $[Ru^{IV}{=}O]^{2+} + H_2O \rightleftharpoons [Ru^{II}\text{-}OOH]^{+} + H^{+}_{solv}$ case (Figure 5.6, top right).

For the $^{1}[Ru^{IV}{=}O]^{2+} + OH^{-}$ system, the transition state barrier is only 0.03 eV (Table 5.2), which is comparable to k_bT at room temperature. This makes a case for a proton-first mechanism for the O – O bond formation step. The decreased transition state barrier compared to the system with H_2O leads to a higher rate constant for the reaction. The Eyring Equation

$$k = \frac{k_B T}{h} \exp\left(\frac{-\Delta G^{*}_{O-O}}{k_B T}\right), \qquad (5.1)$$

where *h* is Planck's constant, describes the rate constant for a microscopic single-step reaction from reactant to product.[40] Comparing the rate constants for $^{1}[Ru^{IV}{=}O]^{2+} + H_2O \rightleftharpoons {}^{1}[Ru^{II}\text{-}OOH]^{+} + H^{+}_{solv}$ and $^{1}[Ru^{IV}{=}O]^{2+} + OH^{-} \rightleftharpoons {}^{1}[Ru^{II}\text{-}OOH]^{+}$ using the ratio

$$\frac{k_{OH^-}}{k_{H_2O}} = \exp\left(-\frac{1}{k_B T}\left(\Delta G^{*}_{O-O,OH^-} - \Delta G^{*}_{O-O,H_2O}\right)\right) \qquad (5.2)$$

and Table 5.2, it may also be concluded that the rate of reaction can be increased by a factor of 10^7 by the introduction of a proton acceptor within the water wires surrounding the reaction site. This agrees with previous observations that OH^- is a favourable proton acceptor within the context of PCET,[41] as well as experimental evidence that has shown a dramatic increase in reaction rate for a ruthenium-based WOC as a result of a localised proton acceptor.[15]

The stable intermediates in the proton transfer steps considered here are summarised in Scheme 5.2. If this is compared to the natural system as discussed in Chapter One, one might draw favourable conclusions: introducing a proton acceptor leads to an interchange of intermediates and transition states due to the removal of a proton (cf. Chapter 1, Figure 1.2 (c)), which is associated with a decrease in the overall charge from 2^+ to 1^+. In Chapter One it was postulated that this interchange of intermediates and transition states is responsible for the energetically downhill ligand exchange of O_2 by H_2O, as well as necessary for the release of gaseous O_2. With four trajectories it was shown that O – O bond formation proceeds better in the 1^+ state with a proton acceptor compared to the 2^+ state without proton acceptor, though it does require intersystem crossing from the triplet to the singlet state in both cases. The inclusion of a localised proton acceptor forms a very promising avenue for improving the design of the environment of WOCs.

5.4. Conclusions

Proton diffusion was considered within the context of an explicitly solvated water oxidation catalyst. It was observed that water molecules arranged spontaneously into water wires adjacent to the catalytic site. Proton diffusion along these wires was very rapid; within 250 fs a proton hole was able to travel 8 Å along these wires towards the catalytic centre. The thermodynamic barrier of O – O bond formation, and therefore the reaction rate constant, decreased upon introduction of a proton acceptor. Including a proton acceptor within the simulation box decreased the change in free energy for O – O bond formation by around 1 eV. It can therefore be concluded that when designing the immediate environment of the reaction site, one should include a proton acceptor, preferably within 8 Å of the reaction site, to significantly increase the rate of reaction.

5.5. References

[1] J.-M. Savéant. *Annu. Rev. Anal. Chem.* **2014**, *7* (1), 537–560.
[2] S. Hammes-Schiffer. *J. Am. Chem. Soc.* **2015**, *137* (28), 8860–8871.
[3] C. Costentin and J.-M. Savéant. *Curr. Opin. Electrochem.* **2017**, *1* (1), 104–109.
[4] Yuan Binfang *et al. Eur. J. Org. Chem.* **2017**, *2017* (27), 3947–3956.
[5] M. D. Tissandier *et al. J. Phys. Chem. A* **1998**, *102* (40), 7787–7794.
[6] M. R. DuBois and D. L. DuBois. *Chem. Soc. Rev.* **2008**, *38* (1), 62–72.
[7] R. Matheu *et al. ACS Catal.* **2017**, 6525–6532.
[8] S. H. A. M. Leenders *et al. Chem. Soc. Rev.* **2014**.
[9] D. C. Marelius *et al. Eur. J. Inorg. Chem.* **2014**, *2014* (4), 676–689.
[10] S. Hammes-Schiffer. *Acc. Chem. Res.* **2017**, *50* (3), 561–566.
[11] L. Vilella *et al. Dalton Trans.* **2011**, *40* (42), 11241–11247.
[12] F. Acuña-Parés *et al. Chem. - Eur. J.* **2014**, *20* (19), 5696–5707.
[13] Q. Zeng *et al. Coord. Chem. Rev.* **2015**, *304–305*, 88–101.
[14] D. B. Grotjahn. *Chem. – Eur. J.* **2005**, *11* (24), 7146–7153.
[15] R. Matheu *et al. J. Am. Chem. Soc.* **2015**, *137* (33), 10786–10795.
[16] L. Li *et al. Chem. Commun.* **2010**, *46* (39), 7307–7309.
[17] T. Zhang *et al. J. Am. Chem. Soc.* **2014**, *136* (1), 273–281.

[18] P. Garrido-Barros *et al. J. Am. Chem. Soc.* **2015**, *137* (21), 6758–6761.
[19] A. Monti *et al. J. Phys. Chem. C* **2016**, *120* (40), 23074–23082.
[20] J. L. Vallés-Pardo *et al. ChemPhysChem* **2012**, *13* (1), 140–146.
[21] J. M. de Ruiter and F. Buda. *Phys. Chem. Chem. Phys.* **2017**, *19* (6), 4208–4215.
[22] M. Tuckerman *et al. J. Chem. Phys.* **1995**, *103* (1), 150–161.
[23] A. Hassanali *et al. Proc. Natl. Acad. Sci.* **2013**, *110* (34), 13723–13728.
[24] R. Biswas and G. A. Voth. *J. Chem. Sci.* **2017**, *129* (7), 1045–1051.
[25] J. M. de Ruiter *et al. ACS Catal.* **2016**, *6* (11), 7340–7349.
[26] *CPMD*; Copyright IBM Corp 1990-2008, Copyright MPI für Festkörperforschung Stuttgart 1997-2001.
[27] "Accelrys Software Inc." *Discovery Studio Modeling Environment*; Accelrys Software Inc., San Diego: San Diego, 2012.
[28] B. R. Brooks *et al. J. Comput. Chem.* **1983**, *4* (2), 187–217.
[29] A. D. MacKerell *et al. J. Phys. Chem. B* **1998**, *102* (18), 3586–3616.
[30] C. Hartwigsen *et al. Phys. Rev. B* **1998**, *58* (7), 3641–3662.
[31] I.-C. Lin *et al. Phys. Rev. B* **2007**, *75* (20), 205131.
[32] M. Swart *et al. Molecular Physics* **2004**, *102* (23-24), 2467–2474.
[33] W. Humphrey *et al. J. Mol. Graph.* **1996**, *14* (1), 33–38.
[34] *VMD - Visual Molecular Dynamics*; Theoretical Chemistry and Computational Biophysics Group, University of Illinois, Urbana, U.S.A, 2012.
[35] O. Andreussi and N. Marzari. *Phys. Rev. B* **2014**, *90* (24).
[36] D. Marx *et al. Chem. Rev.* **2010**, *110* (4), 2174–2216.
[37] N. Agmon *et al. Chem. Rev.* **2016**, *116* (13), 7642–7672.
[38] M. E. Tuckerman *et al. Nature* **2002**, *417* (6892), 925–929.
[39] W. Mtangi *et al. J. Am. Chem. Soc.* **2017**, *139* (7), 2794–2798.
[40] E. V. Anslyn and D. A. Dougherty. *Modern Physical Organic Chemistry*; University Science Books, 2006.
[41] C. Costentin *et al. J. Am. Chem. Soc.* **2007**, *129* (18), 5870–5879.

Conclusions and Outlook

Chapter Six

6. Conclusions and Outlook

6.1. Conclusions

Using computational methods to design and optimise catalysts is one of the Holy Grails of chemistry.[1] One of the essential steps on the way to this Holy Grail is the ability to correctly describe catalytic processes.

In **Chapter Two**, *a combination of experimental and computational techniques is described*. This combined analysis is implemented for a series of ruthenium-based mononuclear WOCs, and uses the comparisons between DFT calculations, spectroscopic techniques and electrochemistry to establish a water oxidation mechanism. The computational methods used are essential for the interpretation of experimental observables. The computational characterisation of the catalytic intermediates is done using static calculations, calculations which determine properties for a fixed geometry, i.e. a fixed snapshot in time.

However, chemical reactions are dynamic processes. Furthermore, in the case of WOCs, these processes usually take place within a solvent environment. In **Chapter Three** *dynamic simulations performed in explicit solvent suggest different preferred reaction cycles than static calculations within an implicit solvent*. CPMD was used to examine a mononuclear copper-based WOC within the CSA, an approach which includes both proton and electron acceptors within a fully solvated simulation box. This approach allows for the elucidation of the dynamic evolution between two stable intermediates.

The CSA also allows for examination of the effects of electron and proton transfer independently. In **Chapter Three** the O – O bond formation step of a copper-based WOC was seen to proceed more favourably when electron transfer occurred first, followed by proton transfer. In **Chapter Four** a ruthenium-based WOC examined in **Chapter Two** was investigated within the CSA: after electron transfer, proton transfer during the first catalytic step had reaction barrier of the order of k_BT at room temperature, while proton transfer during the second catalytic step was barrier-less. The energetic effects of proton diffusion and electron transfer were quantified in **Chapter Four**, as well as the energetic contribution of the added electron acceptor. The first two catalytic steps of the ruthenium-based WOC were used as a proof of principle, where, taking the energetic contribution of the added electron acceptor as constant, the change in free energy agreed with experiment within 0.1 eV. The electron transfer energies did have a large standard deviation however, due to the statistical uncertainty of the simulations.

In both **Chapter Three & Four** proton transfer into solution occurred when solvent dynamics established an appropriate hydrogen bonding network. In **Chapter Four** proton release was examined more closely, where it was observed that *a viable water wire is essential for proton release into the solvent*. This was further examined in **Chapter Five**, where an OH^- ion was introduced within the

water wire. The introduction of *a more explicit proton acceptor decreased the reaction barrier of proton transfer* and *appropriate water wires facilitated highly rapid proton diffusion*.

Considering only static intermediates when using computational methods to examine WOC mechanisms, and to thereby conclude design principles, is a dangerous oversimplification. To solve the molecular WOC question, considering the process of a reaction step will be essential. The reaction environment has a significant effect on the reaction process, and it is only by understanding and manipulating this environment that we can hope to design the optimal molecular WOC.

6.2. Outlook

Further Applications of CSA

In this thesis the CSA has been established as a methodology capable of describing the processes of a reaction step. The next step would be to employ the CSA further as a predictive methodology. There has been a significant amount of discussion as to the mechanism of a number of mononuclear WOCs: whether they catalyse water as a singular mononuclear WOC, or as a dimeric couple working via radical coupling.[2–5] The use of a CSA can allow for a comparison between the two, with the inclusions of any effects the solvent may have on these competing mechanisms. The techniques that are applied within the CSA may also be extrapolated to investigate catalysts with multinuclear metal centres. The question of the localisation of spin density within photosystem II, and how this guides water oxidation, is a long standing debate.[6] The CSA could also be used to track spin density changes within similar systems.

The effects of solvent molecules may also be further investigated within the CSA. In this thesis the effects of the inclusion of an OH^- ion acting as a proton acceptor at close proximity to the reaction site were examined. This could be expanded to consider proton acceptors at various distances, in this way the 'likeliness' of proton dissociation could be tweaked. Furthermore, the CSA could be extended to hosts of different solvent molecules. It has been found experimentally that different solvent molecules effect the catalytic activity of WOCs,[7,8] and the CSA can be used predictively to investigate the how and why of these environmental effects.

The CSA could be used to further investigate the spin-intersystem crossing that was observed during O – O bond formation in Chapter Five. However, in the current implementation, simulations remain on the Born-Oppenheimer surface and so there is no possibility for the investigation of non-adiabatic processes. For such cases, which include quantum coherence effects and the tunnelling of protons and electrons, the CSA would have to be extended to include non-

adiabatic dynamics methodologies.

One of the strengths of the CSA is its ability to decouple proton and electron transfer. In this way proton and electron transfer can be examined in varying sequences throughout the catalytic cycle. In natural photosynthesis, the catalytic steps do not all proceed by tidily coupled PCET.[9] Perhaps the gateway for the optimal WOC lies in mimicking this technique. The CSA can most definitely contribute in the investigation and design of these decoupled proton and electron transfer steps.

One of the dilemmas currently facing the CSA is the statistical uncertainty in the predicted free energy changes. But if numerical accuracy is less of a priority, this opens doors to using less computationally intensive methods, such as adaptive QM/MM or Density Functional based Tight binding method.[10–12] In using such methods, one can start to consider much larger and more complex systems. These complex systems could involve a reaction site environment which actively takes part and guides the process of the reaction.

Further Applications of Water Wires

In this thesis it was shown that water wires can dramatically facilitate proton transfer away from the reaction site. Within the CSA further modifications of these water wires can be examined, as well as the artificial creation of them. The function of these water wires are a key catalytic principle which should be extended into the design of future photoelectrochemical devices. One can imagine, for example, a WOC embedded within a matrix with a localised source of proton acceptors. In this way a more extended proton channel is devised, comparable to the more elaborate designs of proteins, which one could dub part of a smart matrix.[13]

6.3. References

[1] S. Hammes-Schiffer. *Acc. Chem. Res.* **2017**, *50* (3), 561–566.
[2] L. Duan *et al. Nat. Chem.* **2012**, *4* (5), 418–423.
[3] S. W. Sheehan *et al. Nat. Commun.* **2015**, *6*.
[4] L. Bíró *et al. Dalton Trans.* **2010**, *39* (42), 10272–10278.
[5] I. López *et al. Angew. Chem.* **2014**, *126* (1), 209–213.
[6] N. Cox *et al. Science* **2014**, *345* (6198), 804–808.
[7] D. G. H. Hetterscheid and J. N. H. Reek. *Eur. J. Inorg. Chem.* **2014**, *2014* (4), 742–749.
[8] O. Diaz-Morales *et al. J. Am. Chem. Soc.* **2014**, *136* (29), 10432–10439.
[9] H. Dau and M. Haumann. *Biochim. Biophys. Acta BBA - Bioenerg.* **2007**, *1767* (6), 472–483.
[10] J. M. Boereboom *et al. J. Chem. Theory Comput.* **2016**, *12* (8), 3441–3448.
[11] M. Elstner *et al. Phys. Rev. B* **1998**, *58* (11), 7260–7268.
[12] Frauenheim Th. *et al. Phys. Status Solidi B* **2000**, *217* (1), 41–62.
[13] R. Schlögl. *Chemical Energy Storage*; Walter de Gruyter, 2013.

Summary

In the search for sustainable energy solutions, the idea of artificial photosynthesis has been proposed as an approach with which to use water and sunlight to produce hydrogen. Hydrogen is an important chemical building block. It is an essential part of agricultural fertiliser production, important within the chemical industry, and can be reacted with CO_2 to decrease CO_2 levels in the atmosphere. Key in the development of hydrogen production technologies is the splitting of water using a water oxidation catalyst. In the water-splitting reaction, water is split into electrons, protons, and oxygen. The protons can then be used to form hydrogen.

The traditional computational methods for establishing how a catalyst splits water are demonstrated in **Chapter Two**, where a combined experimental and computational analysis is performed on a series of ruthenium-based water oxidation catalysts. The computational techniques allow for an in-depth understanding and interpretation of experimental data, and it is the combination of theory and experiment which leads to the clarification of the catalytic mechanism. This mechanism proceeds via four steps, each step featuring the coupled transfer of one proton and one electron away from the catalytic site. The computational characterisation of the catalytic intermediates is done using static calculations, which consider only a fixed snapshot in time. Furthermore, the catalyst's environment is represented by a continuum model. The continuum model generates a smooth surface around the catalyst molecule, which then reflects certain molecular properties in different ways depending on what kind of solvent environment it is modelling.

If one wishes to rationally design a catalyst, it is important to consider how the molecules surrounding the catalyst can affect the water-splitting reaction, as well as the reaction's dynamic nature. Neither can be investigated using the traditional methods used in Chapter Two. In **Chapter Three** it is observed that a different pathway is preferred when using an environment of water molecules instead of the continuum model. Furthermore, a closed system approach is introduced in Chapter Three, which features water molecules as proton acceptors and a metal ion as an electron acceptor. This approach allows for independent proton and electron transfer within the same simulation box. The approximation made in Chapter Two, where the energy contribution of proton and electron transfer was approximated using a correction term, is no longer necessary.

The independent energy contribution of the proton and electron transfer away from a ruthenium-based catalyst is quantified, using the closed system approach, in **Chapter Four**. The entire process of proton transfer from the catalyst into the surrounding water environment, and the resulting energy profile, can be considered. Proton transfer into the surrounding water was seen to be more favourable when the water molecules were arranged to form water wires radiating out from the catalytic centre. The first two catalytic steps of the catalyst are used

as a proof-of-principle, and compared to the experimental data measured for the same catalyst in Chapter Two. Taking the energetic contribution of the electron acceptor as constant, the change in energy for each catalytic step, as calculated using the closed system approach, agrees well with experimental results.

Proton transfer into the surrounding water environment is further investigated in **Chapter Five**. The water wires radiating out from the catalytic centre were modified to introduce OH^-, which is a good proton acceptor. The introduction of a more explicit proton acceptor decreased the energy barrier for the O – O bonding step. The O – O bonding step was found to be the most energetically demanding step of the water-splitting mechanism established in Chapter Two. Decreasing the energy barrier for this catalytic step would allow for a more rapid rate of water splitting.

In optimising water oxidation catalysts it is important to consider the interaction with the surrounding environment, and how this can impact the catalytic reaction. This impact can be missed if the environment is approximated using a continuum model. Furthermore, catalytic reactions are dynamic processes; to understand these fully, they should also be investigated using dynamic methods. Lastly, electrons and protons are independent particles, treating them as such will allow for a more detailed adjustment of catalytic mechanisms, and therefore allow for the rational design of the optimal water oxidation catalyst.

Samenvatting

In de zoektocht naar duurzame energieoplossingen wordt kunstmatige fotosynthese beschouwd als mogelijke methode om waterstof te produceren uit water en zonlicht. Waterstof is een belangrijke chemische bouwsteen, onder meer in de chemische industrie. Ook is het is een onmisbare component in de productie van kunstmest en kan het bijdragen aan een afname van broeikasgassen in de atmosfeer door te reageren met CO_2. Het splitsen van water met behulp van een wateroxidatiekatalysator is een essentiële stap in de productie van waterstof. In de splitsingsreactie wordt water ontleed in elektronen, protonen en zuurstof. De protonen kunnen vervolgens gebruikt worden om waterstof te vormen.

De traditionele berekeningsmethoden om vast te stellen hoe een katalysator water ontleedt, worden uitgelegd in **Hoofdstuk Twee**, waarin een gecombineerde experimentele en theoretische analyse van een wateroxidatiekatalysator op basis van Ruthenium beschreven wordt. De theoretische modellen maken het mogelijk om dieper in te gaan op de betekenis van de experimentele data, en de combinatie van theorie en experiment leidt dan ook tot opheldering van het mechanisme van de katalyse. Water oxidatie verloopt via vier stappen, waarbij in iedere stap een proton en een elektron van de plaats van de reactie afgevoerd wordt. De theoretische karakterisering van de katalytische tussenproducten wordt gedaan door middel van statische berekeningen die een tijdelijke opname, een 'foto' van het proces, beschouwen. De omgeving wordt beschreven met een continuüm model om de elektrostatische interactie van de katalysator met het oplosmiddel te benaderen.

Wanneer men echter de optimale katalysator wil ontwerpen, is het belangrijk om in overweging te nemen hoe de moleculen nabij de katalysator de reactie kunnen beïnvloeden, evenals de dynamiek van de reactie zelf. Geen van beide kan onderzocht worden door middel van de methoden in Hoofstuk Twee. In **Hoofstuk Drie** wordt tevens duidelijk dat wanneer expliciete watermoleculen gebruikt worden in de simulaties, in plaats van het continuüm model dat de omgeving van de katalysator voorstelt, een ander reactiemechanisme plaatsvindt. Daarnaast wordt in Hoofdstuk Drie een gesloten systeembenadering geïntroduceerd, waarin expliciete watermoleculen optreden als protonacceptoren en een metaalion als elektronacceptor. Deze aanpak maakt onafhankelijke proton- en elektronuitwisseling mogelijk binnen dezelfde gesimuleerde ruimte. De benadering die gebruikt werd in Hoofdstuk Twee, waar de energiebijdrage van proton- en elektronuitwisseling benaderd werd door het toepassen van een correctiefactor, is daardoor niet meer nodig.

De onafhankelijke energiebijdrage van de proton- en elektronuitwisseling van het reactieoppervlak van de Rutheniumkatalysator wordt in **Hoofdstuk Vier** gekwantificeerd door middel van een gesloten systeembenadering. Het volledige proces van de protonuitwisseling van de katalysator naar het omliggende water en het daarbij horende energieprofiel, kunnen zo worden beschouwd. Protonuitwisseling naar het omliggende water bleek gemakkelijker plaats te

vinden wanneer de watermoleculen op een bepaalde manier gepositioneerd waren, waardoor 'waterdraden' vanaf het katalytisch centrum gevormd werden. De eerste twee katalytische stappen worden gebruikt als 'proof-of-principle' en vergeleken met de experimentele data die verkregen zijn voor dezelfde katalysator in Hoofdstuk Twee. Wanneer de energiebijdrage van de elektronacceptor als constante beschouwd wordt, blijkt de energieverandering voor elke katalytische stap wanneer deze berekend wordt met de gesloten systeemaanpak goed overeen te komen met de experimentele data.

Protonuitwisseling in de richting van de omliggende watermoleculen wordt in **Hoofdstuk Vijf** nader onderzocht, waarbij een aangepaste variant gebuikt wordt van de waterdraden die vanaf het katalytisch centrum naar buiten gericht zijn. In dit model wordt OH^- geïntroduceerd, een goede protonacceptor. De introductie van OH^- verlaagt de energiebarrière voor de vorming van de O–O binding. Deze stap bleek in het watersplitsingsmechanisme dat in Hoofdstuk Twee is vastgesteld de hoogste activeringsenergie te vereisen. Het verlagen van deze energiebarrière zal leiden tot een sneller verloop van het watersplitsingsproces, wat een significante stap zou zijn in het ontwerpen van een betere katalysator.

Bij het optimaliseren van watersplitsingskatalysatoren is het belangrijk om de interacties met de omgeving en de effecten hiervan op de katalysereactie in overweging te nemen. Deze effecten kunnen gemakkelijk over het hoofd gezien worden wanneer de omgeving van de katalysator slechts benaderd wordt door een continuüm model. Daarbij geldt tevens dat katalysereacties dynamische processen zijn. Ze dienen daarom dan ook onderzocht te worden met dynamische modellen om ze volledig te kunnen begrijpen. Tot slot, elektronen en protonen zijn onafhankelijke deeltjes. Door ze ook als zodanig te behandelen kan met grote nauwkeurigheid gewerkt kan worden aan het ontwerpen van de optimale wateroxidatiekatalysator.

Publications

J. M. de Ruiter, R. L. Purchase, A. Monti, C. J. M. van der Ham, M. P. Gullo, K. S. Joya, M. D'Angelantonio, et al. "Electrochemical and Spectroscopic Study of Mononuclear Ruthenium Water Oxidation Catalysts: A Combined Experimental and Theoretical Investigation."
ACS Catalysis, **2016**, doi: 10.1021/acscatal.6b02345

- Chapter Two, this thesis

J. M. de Ruiter, and F. Buda "Introducing a Closed System Approach for the Investigation of Chemical Steps Involving Proton and Electron Transfer; as Illustrated by a Copper-Based Water Oxidation Catalyst."
Physical Chemistry Chemical Physics, **2017**, doi: 10.1039/C6CP07454E

- Chapter Three, this thesis

J. M. de Ruiter, H. J. M. de Groot, and F. Buda. "Energetic Effects of a Closed System Approach Including Explicit Proton and Electron Acceptors as Demonstrated by a Mononuclear Ruthenium Water Oxidation Catalyst."
ChemCatChem, **2018**, doi: 10.1002/cctc.201801093

- Chapter Four, this thesis

J. M. de Ruiter, H. J. M. de Groot, and F. Buda. "Increasing the Rate of the Deprotonation Step in a Single-site Water Oxidation Catalyst: Tuning the Environment."

- In preparation.
  - Chapter Five, this thesis

Y. Shao, J. M. de Ruiter, H. J. M. de Groot, and F. Buda. "Photocatalytic Water Splitting Cycle in a Dye-catalyst Supramolecular Complex: *ab initio* Molecular Dynamics Simulations."

- In preparation.

A. Monti, J. M. de Ruiter, H. J. M. de Groot, and F. Buda. "A Dynamic View of Proton-Coupled Electron Transfer in Photocatalytic Water Splitting."
The Journal of Physical Chemistry C, **2016**, doi:10.1021/acs.jpcc.6b08244.

H. Boots, J. M. de Ruiter, T. T. Nguyen, A. Brizard, E. Peeters, S. F. Wuister, T.S. Druzhinina, J. K. Wolterink, J. G. E. M. (Hans) Fraaije. "Pitch Variations of Self-Assembled Cylindrical Block Copolymers in Lithographically Defined Trenches."
J. Micro/Nanolith. MEMS MOEMS **2014**, doi:10.1117/1.JMM.13.3.033015.

T. T. Nguyen, J. M. Finders, W. S. M. M. Ketelaars, S. F. Wuister, E. C. A. van der Heijden, H. J. C. Meessen, R. Koole, E. Peeters, C. M. van Heesch, A. Brizard, H. Boots, T. S. Druzhinina, J. M. de Ruiter, "Method to provide a patterned orientation template for a self-assemblable polymer."
ASML Netherlands B.V, *US Patent App. 20140245948*, filed 2 Oct 2012, and published 4 Sep 2014.